TECHNISCHE
UNIVERSITÄT
MÜNCHEN

WALTHER - MEISSNER -
INSTITUT FÜR TIEF -
TEMPERATURFORSCHUNG

BAYERISCHE
AKADEMIE DER
WISSENSCHAFTEN

Circuit nano-electromechanics transmon qubits, nano-strings and resonators

Master's Thesis

Daniel Schwienbacher

Supervisor: Dr. Hans Hübl

Munich, May 2016

Fakultät für Physik
Technische Universität München

Contents

Chapter 1

Introduction

In the last decade, micro- and nanoscale mechanical resonators have gained in importance. Coupling mechanical degrees of freedom to optical ones allows to measure mechanical displacement from macroscale gravitational wave detectors [1] along microscale cantilevers used in scanning probe microscopy [2, 3] to nanoscale mechanical beams coupled to superconducting μ-wave resonators [4, 5]. Mechanical resonators can also be used for measuring minuscule forces and masses [6, 7] and are widely used in commercial applications such as acceleration sensors in smartphones, cars and other every day electronic equipment (c.f. [8]). The read out mechanisms are different though similar for these systems. Typical readout schemes for the displacement and the motion of the mechanical system are based on optical [1] and electrical techniques. In circuit-based nanoscale systems the readout and therefore the coupling is intrinsically electrical. For microscale systems optical and electrical variants have been implemented [8, 9]. In circuit-based systems the mechanical resonator changes either the capacitance or the inductance of the μ-wave circuit which impacts the eigenfrequency of the electromagnetic resonator and hereby mediates a mutual interaction between the two [6]. To date, nanoscale mechanical resonators coupled to superconducting μ-wave resonators are well understood [5, 9–13] and therefore merging the circuit nano-mechanical system with circuit quantum electro-dynamical systems seems the logical next step.

In quantum computing the classical bits are replaced with quantum bits (qubits) which enable that not only two states, as classical ones, but due to being a quantum two-level system, any superpositions of two eigenstates can be used for computation. This field of science is called quantum information processing (QIP). QIP is predicted to outperform [14] classical information processing for tasks like the travelling salesman problem or database searches. The most known example is Shor's algorithm for factoring integers [15, 16], other problems are not solvable by classical computation at all, but can be accessed by quantum simulation [17].

Circuit quantum electrodynamics (QED) uses the photons inside superconducting transmission lines and resonators to interact with artificial two-level systems or atoms that act as qubits [18, 19]. Circuit QED combines the advantages of large coupling strengths [20, 21] and good scalability by established fabrication techniques like optical or electron beam lithography [22, 23]. However, the disadvantage of these superconducting qubits is a much smaller coherence time than the one of e.g. isolated atoms in cavities [24] which in turn have small coupling strengths. Nevertheless recent advancements show increasing qubit coherence times [25], especially for so called transmon qubits [19, 26].

Merging the fields of circuit electromechanics and circuit QED offers a set of opportunities. Among the most imperative is that the combination of a superconducting qubit and a mechanical resonator has shown a strengthening of the electromechanical coupling of several orders of magnitude [27, 28]. Combining the large coupling strength of a superconducting qubit (acting as a two-level system) with two resonators, a μ-wave electrical resonator on one side and a nanobeam mechanical resonator at the other, promises access to new physics via enhanced nonlinearities [29, 30]. Recent experiments demonstrated such three body interactions as e.g. coherent conversion of qubit excitations to phonons as sideband Rabi oscillations in the qubit-resonator spectrum [28]. This allows using the long coherence times of mechanical resonators in combination with the large coupling strengths of circuit qubits e.g. using the mechanical resonator as storage for the quantum information.

Theory proposes that by integrating the mechanical nanobeam resonator into the shunt capacitance of a transmon qubit quantum mechanical three body interactions between photons, phonons and qubit excitations can be realized [31]. One of the basic predicted interactions is the ground state cooling of the mechanical resonator. When realized, quantum states prepared in the qubit can be transferred to the mechanical resonator [32] and hereby mechanical Fock states can be realized [31].

In current hybrid systems, consisting of a μ-wave resonator, a transmon qubit and a mechanical resonator [27, 28], only a mechanical resonator which is coupling the transmon capacitance to the ground plane has been implemented. In this thesis the feasibility of integrating a mechanical nanobeam resonator into the transmon shunt capacitance is studied. The fabrication of the individual subsystems has been demonstrated and optimized at the WMI during the last years [33–35]. But a study investigating the combination of the circuit QED and nano-electromechanics fabrication steps in one and the same device has not been pursued so far. This thesis is dedicated to this task and demonstrates the successful fabrication of a hybrid device containing a transmon qubit, a nano-mechanical resonator and a μ-wave resonator. Additionally, the characterization of the individual systems after the changes in fabrication is presented and the feasibility of uniting the individual systems (transmon qubit, μ-wave resonator and mechanical nanobeam resonator) on a single chip is discussed.

The structure of this thesis is as follows: First the theoretical background of the individual subsystems and hybrid systems will be explained in chapter 2. In chapter 3 the fabrication steps and techniques as well as the sample layouts and measurement devices are presented. Chapter 4 shows the characterization of a mechanical nanobeam resonator at room temperature and at millikelvin temperatures. Spectroscopy data of a transmon qubit coupled to a μ-wave resonator is presented. Finally the results of this thesis are summarized in chapter 6 and an outlook on future measurements and progress towards three body interaction devices is given.

Chapter 2

Theory

In this chapter the mechanical beams, transmon qubits and µ-wave resonators are introduced theoretically. Starting with the tensile stressed aluminum beam used as mechanical oscillating capacitor, discussing then the transmon qubit acting as a two level system and finally the µ-wave resonator used for coupling those systems to enable experimental access.
After these individual components the coupling mechanisms will be investigated. These are the electromechanical coupling between the nano beam and the µ-wave resonator and the capacitive coupling between the transmon qubit and the µ-wave resonator. The theoretical approaches will be motivated briefly and the important relations are shown.

2.1 Tensile stressed nanobeam resonators

This section introduces the nanomechanical beam which will be used as mechanical oscillator. The focus lies on the intrinsic properties of the nanomechanical beam. The theoretical equations describing the mechanical vibration will be presented, showing that it is sufficient to consider the center of mass amplitude motion with an effective mass. A picture of the mechanical motion will be given, taking into account damping and driving forces. The derivation and solution of these equations is found in textbooks about continuous classical mechanics and Euler-Bernoulli beam theory, e.g. [36]. Here only the main results are highlighted.

2.1.1 Mechanical mode frequencies and displacement

The dynamics of an ideal undamped doubly clamped beam with a length l extending in z-direction and vibrating in x-direction (see Fig. (2.1)) for the n-th vibrational mode is given by [10]:

$$\Omega_{\mathrm{m}}^{(n)} = \frac{n\pi}{l}\sqrt{\frac{\sigma}{\rho}}.$$

Where σ is the tensile stress and ρ is the density. Due to the high tensile stress, and the high aspect ratio between length and cross-section of the beam it can be considered

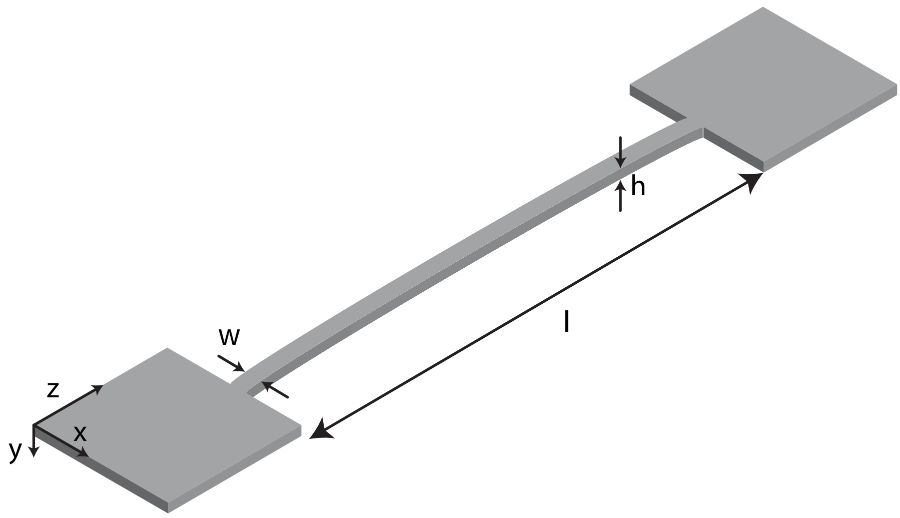

Figure 2.1: Schematic picture of the nanobeam used in this thesis. Only the aluminum beam is shown, with characterizing structural parameters.

one dimensional for this calculations. The simplification of only considering the center of mass motion is sufficient to describe the behaviour of the beams amplitude, however to accurately describe further important parameters like the energy it has to be considered more thoroughly which parts of the beam's mass contribute to the center of mass motion. To do this an effective mass is introduced, this effective mass depends on the structural layout and boundary conditions of the beam. For a highly tensile stressed beam the effective mass is given by [37] $m_{\mathrm{eff}} = \frac{1}{2}m$ with $m = \rho Al$. With the density of aluminium $\rho_{\mathrm{Al}} = 2700\,\frac{\mathrm{kg}}{\mathrm{m}^3}$ [38] the effective mass of a beam with length $50\,\mu\mathrm{m}$ used in this thesis is about $1.8 \times 10^{-15}\,\mathrm{kg} = 1.8\,\mathrm{pg}$.

2.1.2 Resonance frequency and dissipation

To describe the nanomechanical beam in a more realistic way after introducing the effective mass also damping has to be added to the ideal harmonic resonator. The damping force in harmonic oscillators is proportional to the velocity with a damping constant Γ_{m} [3]. In the equation of motion also a force driving the oscillator $F(t)$ is taken into account [33]:

$$\ddot{x}(t) + \Gamma_{\mathrm{m}}\dot{x}(t) + \Omega_{\mathrm{m}}^2 x(t) = F(t)/m_{\mathrm{eff}}.$$

Here Ω_{m} is the resonance frequency of the first vibrational mode of the nanomechanical beam. The mechanical damping rate Γ_{m} can be understood as the energy dissipation rate of the mechanical oscillator and can have various sources. The damping rate is the sum of all damping contributions $\Gamma_{\mathrm{m}} = \sum_i \Gamma_i$ which have been studied in literature [39, 40]. The most important damping channels for typical tensile stressed beams are dissipation into the clamps holding the beam [39] and intrinsic losses due to the coupling of acoustic

excitations to two level systems inside the material (material defects) [40].
In an experiment the the mechanical resonator is always connected to a substrate of some kind, therefore the displacement spectral density of mechanical fluctuations of the vibrational mode in contact with a thermal bath at temperature T and high mechanical occupation $\bar{n}_\mathrm{m} = k_\mathrm{B}T/\hbar\Omega_\mathrm{m} \gg 1$ has to be considered because it describes the actual physical system. To do this the mode temperature of an oscillations is defined. The fluctuation dissipation theore [41] allows to approximate the spectral density [33, 42]:

$$S_{xx}(\Omega) \approx \frac{1}{2m_\mathrm{eff}} \cdot \frac{2\Gamma_\mathrm{m} k_\mathrm{B} T}{\left(\Omega^2 - \Omega_\mathrm{m}^2\right)^2 + \Gamma_\mathrm{m}^2 \Omega^2}$$

with the Boltzmann constant k_B. For high Q resonators this can be simplified to a Lorentzian [33]:

$$S_{xx}(\Omega) \approx \frac{k_\mathrm{B}T}{2m_\mathrm{eff}\Omega_\mathrm{m}^2} \cdot \frac{\Gamma_\mathrm{m}}{(\Omega - \Omega_\mathrm{m}) + \left(\frac{\Gamma_\mathrm{m}}{2}\right)^2}. \tag{2.1}$$

Often the factor $\frac{\Gamma_\mathrm{m}}{(\Omega-\Omega_\mathrm{m})+\left(\frac{\Gamma_\mathrm{m}}{2}\right)^2}$ The mean square amplitude of the mechanical resonator can be calculated from this mechanical displacement spectrum [33]:

$$\langle \delta x^2 \rangle = \int_0^\infty \frac{d\Omega}{2\pi} S_{xx} \approx \frac{k_\mathrm{B}T}{m_\mathrm{eff}\Omega_\mathrm{m}^2} \tag{2.2}$$

and thus a temperature can be assigned to the mechanical mode:

$$T_\mathrm{m} = \frac{m_\mathrm{eff}\Omega_\mathrm{m}^2}{k_\mathrm{B}} \langle \delta x^2 \rangle. \tag{2.3}$$

For the undisturbed mechanical resonator this temperature is the bath(fridge)-temperature $T_\mathrm{m} = T_\mathrm{fridge}$.

2.2 Superconducting coplanar waveguide μ-wave resonators

This part is dedicated to the superconducting coplanar wave-guide μ-wave resonator used as coupling and readout element in this thesis. The use of superconducting materials such as aluminum allows for realizing devices with negligible Ohmic losses and permits high quality factors. In this thesis the μ-wave resonators will be coupled to superconducting transmon qubits as well as to nanomechanical oscillators inparticular for the readout of their states. Two types of resonators were used, for the investigation of the coupling between nanomechanical beam, $\lambda/4$ wavelength coplanar wave guide (CPW) μ-wave resonators were employed, for the coupling to the transmon qubit and for coupling to both devices (qubit and nanobeam) $\lambda/2$ wavelength μ-wave resonators were utilized. Both behave the same way from a physics point of view. The $\lambda/2$ wavelength resonator has the advantage of being shorter, and it is read out by coupling it to a transmission line.

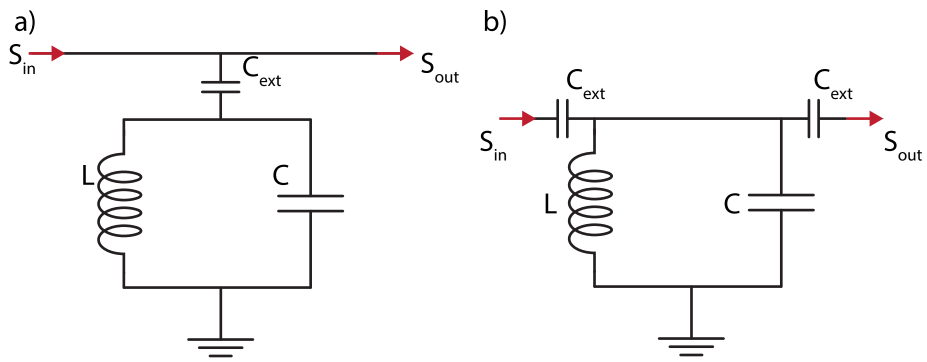

Figure 2.2: Equivalent circuit diagrams for $\lambda/4$ and $\lambda/2$ wavelength µ-wave resonators. The resonator is represented by a LC equivalent circuit respectively. The $\lambda/4$ wavelength resonator is coupled to a feedline by a capacitance C_{ex}(a). The $\lambda/2$ wavelength resonator is coupled to µ-wave ports by two capacitances C_{ex} (b).

Characteristics of a coplanar wave guide µ-wave resonator

Coplanar waveguides consist of a center conductor separated from ground planes by a gap as schematically shown in Fig. (3.2,f)). Due to the structure consisting of a thin metal layer the impedance is defined by the dielectric parameters of the substrate and the ratio between the width of the central conductor and the width of the gaps to the ground planes. This enables impedance matching the CPW structures to external µ-wave cables. The resonance frequency of such a µ-wave resonator is given by $\omega_{\mathrm{r}} = 1/\sqrt{LC}$ [43]. The overall inductance L and overall capacitance C are proportional to the length l of the CPW structure [44] and thus can be designed accordingly.
The voltage transmission spectrum of a CPW µ-wave resonator, coupled to a microwave transmission line as shown in Fig. (2.2,a)), corresponds to the one of an absorptive harmonic oscillator is given by [45]:

$$T(\omega) = \left|1 - \frac{\kappa_{\mathrm{ext,r}}/2}{\kappa_{\mathrm{ges,r}}/2 + i(\omega - \omega_{\mathrm{r}})}\right|^2 = \left|\frac{\kappa_{\mathrm{int,r}}/2 + i(\omega - \omega_{\mathrm{r}})}{\kappa_{\mathrm{ges,r}}/2 + i(\omega - \omega_{\mathrm{r}})}\right|^2$$

with internal and internal loss rates $\kappa_{\mathrm{int,r}} + \kappa_{\mathrm{ext,r}} = \kappa_{\mathrm{ges,r}}$. For a $\lambda/2$ resonator, coupled to an input and output microwave line as shown in Fig. (2.2,b)), the transmission spectrum is given by [33]:

$$T(\omega) = \left|\frac{\kappa_{\mathrm{ext,r}}/2}{\kappa_{\mathrm{ges,r}}/2 + i(\omega - \omega_{\mathrm{r}})}\right|^2$$

The external loss is mainly dictated by the layout of the coupling capacitance between transmission line and µ-wave resonator, whereas the internal loss dominantly depends on radiation leakage to the environment and absorption, thus it depends on the interface between µ-wave resonator and the quality of the coplanar waveguide structure the resonator consist of, there dissipation to two level systems (TLS) is the most influential powerdependent loss mechanism, coupling to quasi particles and radiation and dielectric losses are power independent and scale with the temperature [46]. The loss rates allow to define a quality factor Q comparing the energy stored in the resonator to the energy dissipated per period, mathematically given as:

$$Q = \frac{\omega_{\mathrm{r}}}{\Gamma_{\mathrm{r}}} \tag{2.4}$$

The ratio between internal and external loss rate $\eta = \frac{\kappa_{\mathrm{ext,r}}}{\kappa_{\mathrm{int,r}}}$ allows to distinguish between an undercoupled resonator ($\eta < 1/2$) where the internal loss rate dominates, an overcoupled resonator ($\eta > 1/2$) where the external loss rate dominates and the critically coupled case $\eta = 1/2$ where the losses are in balance.

2.3 Electromechanical coupling between a nanomechanical beam and a superconducting µ-wave resonator

To experimentally investigate the nanomechanical beam at mK temperatures, it is coupled capacitively to a µ-wave resonator. In this section, the physical origin of this coupling and its effect on the µ-wave resonator is discussed.
The nanomechanical beam integrated into the centerline of the µ-wave resonator and the groundplane of the resonator act as a capacitor with capacitance $C_{\mathrm{g,m}}$. This capacitance oscillates, as the mechanical beam vibrates, around its equilibrium position $C_{\mathrm{g,m}}(0) \equiv C_{\mathrm{g,m,0}}$. As depicted in the equivalent circuit diagram in Fig. (2.3), this capacitance is connected parallel to the overall capacitance of the µ-wave resonator. For small displacements the resonance frequency of the µ-wave resonator with coupled nanobeam is given as:

$$\omega_{\mathrm{r}}(x) = \frac{2\pi}{4\sqrt{L(C + C_{\mathrm{g,m}}(x))}} \approx \omega_{\mathrm{r}} \left(1 - \frac{C_{\mathrm{g,m}}(x)}{2C}\right). \tag{2.5}$$

Here, the coupling capacitance to the transmission line C_{ext} is assumed to be small compared to the overall capacitance and therefore neglected. The same holds for the beam capacitance $C_{\mathrm{g,m}} \ll C$. With this the electromechanical coupling can be estimated to [5]:

$$G_{\mathrm{m}} = -\frac{\partial \omega_{\mathrm{r}}}{\partial x} = \frac{\omega_{\mathrm{r}}}{2C}\frac{\partial C_{\mathrm{g,m}}}{\partial x} = \frac{2Z\omega_{\mathrm{r}}^2}{2\pi}\frac{\partial C_{\mathrm{g,m}}}{\partial x},$$

with $Z = \sqrt{L/C}$. With this, an estimation of the coupling is possible for known values of the impedance $Z = 50\,\Omega$ and resonance frequency ω_r. To compare different systems it

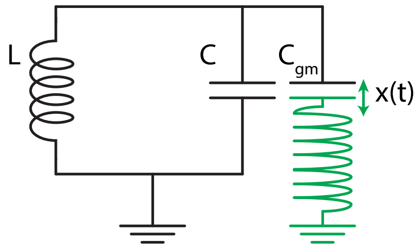

Figure 2.3: Equivalent circuit diagram of the electromechanical system. The LC oscillator depicting the µ-wave resonator is connected parallel to a vibrating capacitance $C_\mathrm{g,m}$ (green).

is advantageous to define the electromechanical vacuum coupling $g_\mathrm{m,0} = G_\mathrm{m}/x_\mathrm{zpf}$, where $x_\mathrm{zpf} = \sqrt{\hbar/2m_\mathrm{eff}\Omega_\mathrm{m}}$ is the square amplitude of the mechanical zero point fluctuation. The vacuum coupling allows comparison of different systems.

2.3.1 Electromechanical interaction

Classically the mutual coupling between optical and mechanical degrees of freedom can be described as counteracting forces. The microwave mode changes the mechanical oscillator with a force similar to the radiation pressure. The mechanical mode further influences the resonator by the means of a back-action force by changing the resonators resonance frequency. To describe the physics of a system consisting of an µ-wave resonator and a mechanical mode, the following set of equations of motion is used. these equations are written in a rotating frame with frequency ω_d, the frequency used to drive the resonator [47]:

$$\begin{aligned} \dot{a} &= (i(\Delta - G_\mathrm{m}x(t) - \kappa_\mathrm{ges,r}/2)a(t) + \sqrt{\frac{\kappa_\mathrm{ext,r}}{2}}\bar{s}_\mathrm{in}(t), \\ \ddot{x}(t) + \Gamma_\mathrm{m}\dot{x}(t) + \Omega_\mathrm{m}^2 x(t) &= -\hbar G_\mathrm{m}\frac{|a(t)|^2}{m_\mathrm{eff}}. \end{aligned} \tag{2.6}$$

Here $\kappa_\mathrm{ges,r}$ and $\kappa_\mathrm{ext,r}$ are the total and external loss rates of the µ-wave resonator. Ω_m and Γ_m are the resonance frequency and linewidth of the mechanical motion and m_eff is the effective mass of the nanobeam. $G_\mathrm{m} = (\partial C_\mathrm{g,m}/\partial x)\,2Z\omega_\mathrm{r}^2/2\pi$ is the electromechanical coupling. $\bar{s}_\mathrm{in}(t)$ is the mean drive amplitude.
These coupled equations describe a driven optical resonator, parametrically coupled to a mechanical displacement and a mechanical harmonic oscillator coupled to the photons inside the optical cavity. Here $a(t)$ is the field amplitude normalised to the photon flux in the optical resonator $|a(t)|^2 = n_\mathrm{r}(t)$. The detuning is defined as $\Delta = \omega_\mathrm{d} - \omega_\mathrm{r}$. The solution of the system of equations (2.6) can be decomposed in a static and a dynamic part: $a(t) = \bar{a} + \delta a(t)$ and $x(t) = \bar{x} + \delta x$. The static solution for a constant drive amplitude

$\bar{s}_{\mathrm{in}}$, is given by [33]:

$$\begin{aligned}\bar{a} &= \frac{\sqrt{\kappa_{\mathrm{ext,r}}/2}}{-i(\Delta - G_{\mathrm{m}}\bar{x})}\bar{s}_{\mathrm{in}}\\ \bar{x} &= -\frac{\hbar G_{\mathrm{m}}\bar{a}^2}{m_{\mathrm{eff}}\Omega_{\mathrm{m}}^2}.\end{aligned} \tag{2.7}$$

Substituting Eq. (2.7) into Eq. (2.6) and transferring the resulting, linearised system of equations to the frequency domain leads to the dynamic solutions [33]:

$$\begin{aligned}\delta a(\Omega) &= \frac{-iG_{\mathrm{m}}\bar{a}}{-i(\Delta+\Omega)+\kappa_{\mathrm{ges,r}}/2}\delta x(\Omega)\\ \delta a^*(\Omega) &= \frac{+iG_{\mathrm{m}}\bar{a}}{+i(\Delta-\Omega)+\kappa_{\mathrm{ges,r}}/2}\delta x(\Omega)\end{aligned} \tag{2.8}$$

which correspond to the Stokes and anti-Stokes sideband for a non-zero displacement $\delta x(\Omega)$ rotating at the frequency Ω. Since the mechanical amplitude is maximal at the resonance frequency $\Omega = \Omega_{\mathrm{m}}$, the sidebands are centered around $\omega_{\mathrm{r}} \pm \Omega_{\mathrm{m}}$. An other way to describe this is by considering the Stokes and anti-Stokes scattering processes shown in Fig. (2.4,a). By defining rates A^+ and A^- for the Stokes/anti-Stokes scattering events, it is possible to get values for annihilated(A^-) and created (A^+) phonons in the mechanical beam dependent on the detuning of the drive tone [48]:

$$A^{\pm} = \frac{g_{\mathrm{m},0}^2\bar{n}_{\mathrm{r}}\kappa_{\mathrm{ges,r}}}{(\Delta \mp \Omega)^2 + (\kappa_{\mathrm{ges,r}}/2)^2}. \tag{2.9}$$

From this it is possible to calculate the change in linewidth and resonance frequency of the nanomechanical resonator due to detuned drive fields [33],[49]. Here the natural linewidth and resonance frequency are modified and effective values are given by [33]:

$$\begin{aligned}\Gamma_{\mathrm{m,eff}} &\approx \Gamma_{\mathrm{m}} + 2g_{\mathrm{m},0}^2\bar{n}_{\mathrm{r}}\left(\frac{\kappa_{\mathrm{ges,r}}/2}{(\Delta+\Omega_{\mathrm{m}})^2+(\kappa_{\mathrm{ges,r}}/2)^2} - \frac{\kappa_{\mathrm{ges,r}}/2}{(\Delta-\Omega_{\mathrm{m}})^2+(\kappa_{\mathrm{ges,r}}/2)^2}\right)\\ \text{and}\Omega_{\mathrm{m,eff}} &\approx \Omega_{\mathrm{m}} + g_{\mathrm{m},0}^2\bar{n}_{\mathrm{r}}\left(\frac{\Delta+\Omega_{\mathrm{m}}}{(\Delta+\Omega_{\mathrm{m}})^2+(\kappa_{\mathrm{ges,r}}/2)^2} + \frac{\Delta-\Omega_{\mathrm{m}}}{(\Delta-\Omega_{\mathrm{m}})^2+(\kappa_{\mathrm{ges,r}}/2)^2}\right).\end{aligned} \tag{2.10}$$

Up to now, the classical perspective has been discussed, which is well satisfied for small coupling rates and large side-band driving fields. Next, a quantum mechanical picture will be considered. To describe the interaction between a µ-wave resonator and a mechanical oscillator the corresponding Hamiltonian introduced by Law [50] is used:

$$\hat{H} = \hbar\omega_{\mathrm{r}}\left(\hat{n}_{\mathrm{r}} + \frac{1}{2}\right) + \hbar\Omega_{\mathrm{m}}\left(\hat{n}_{\mathrm{r}} + \frac{1}{2}\right) + \hbar G_{\mathrm{m}}\hat{n}_{\mathrm{r}}\hat{x} + \hat{H}_{\mathrm{d}}. \tag{2.11}$$

Here $\hat{n}_\mathrm{r} = \hat{a}^\dagger \hat{a}$ and $\hat{n}_\mathrm{m} = \hat{b}^\dagger \hat{b} = \frac{1}{2}\left[\frac{m_\mathrm{eff}\Omega_\mathrm{m}}{\hbar}\hat{x}^2 + \frac{\hat{p}^2}{m_\mathrm{eff}\Omega_\mathrm{m}\hbar}\right]$ are the intra-resonator (photon) and mechanical (phonon) excitation number operators. Creation (annihilation) operators are given by $\hat{a}^\dagger$ ($\hat{a}$) and $\hat{b}^\dagger$ ($\hat{b}$) respectively. The operator $\hat{x} = x_\mathrm{zpf}(\hat{b}^\dagger + \hat{b})$ is the mechanical displacement operator and $\hat{p}$ the corresponding mechanical momentum. The external drive field is represented by:

$$\hat{H}_\mathrm{d} = i\hbar\sqrt{\frac{\kappa_\mathrm{ext,r}}{2}}\left(\bar{s}_\mathrm{in}\hat{a}^\dagger e^{-i\omega_\mathrm{d}t} - \bar{s}_\mathrm{in}\hat{a}e^{+i\omega_\mathrm{d}t}\right).$$

The drive amplitude $\bar{s}_\mathrm{in}$ is normalised to the phonon flux resulting from the drive fields intensity $|\bar{s}_\mathrm{in}|^2 = P_\mathrm{d}/\hbar\omega_\mathrm{d}$. The interaction Hamiltonian is given by $\hat{H}_\mathrm{int} = \hbar G_\mathrm{m}\hat{n}_\mathrm{r}\hat{x}$ [33]. A factorised and linearised interaction Hamiltonian can be derived [33],[4, 51]:

$$\hat{H}_\mathrm{int} = \hbar g_\mathrm{m,0}\bar{a}(\delta\hat{a}\hat{b} + \delta\hat{a}^\dagger\hat{b}^\dagger) + \hbar g_\mathrm{m,0}\bar{a}(\delta\hat{a}\hat{b}^\dagger + \delta\hat{a}^\dagger\hat{b}) \tag{2.12}$$

Here $\bar{a}$ is the static part of the drive field amplitude given in Eq. (2.7), $\delta\hat{a}$ and $\delta\hat{a}^\dagger$ are the quantum mechanic analogon to the classical dynamic solutions shown in Eq. (2.8). The first term of Eq. (2.12) enables joint excitations of both degrees of freedom. In the $\Delta > 0$ regime (blue detuned drive tone) this term dominates. The second part of Eq. (2.12) describes the transfer of excitations and is dominant in the red detuned regime $\Delta < 0$. For the zero detuning case $\Delta = 0$ a drive tone has the same contributions of both terms, this leads to a quantum non-demolition (QND) interaction Hamiltonian [52], schematically shown in Fig. (2.4). Here the mechanical mode can be probed without being disturbed by the measurement (see Eq. (2.10) for $\Delta = 0$) and the natural mechanical parameters can be extracted, experimentally this is done in sec. (4.1.4).

2.3.2 Transfer function

The mechanical motion of the nanobeam is, as shown in Eq. (2.5), changes the resonance frequency ω_r of the µ-wave resonator dependent on the mechanical displacement x. The mechanical displacement spectrum is thus connected to the resonance frequency spectrum of the µ-wave resonator [33]:

$$S_{\omega\omega} = G_\mathrm{m}^2 S_{xx} \approx g_\mathrm{m,0}^2 \frac{k_\mathrm{B}T}{\hbar\Omega_\mathrm{m}} \cdot \frac{\Gamma_\mathrm{m}}{(\Omega - \Omega_\mathrm{m})^2 + \left(\frac{\Gamma_\mathrm{m}}{2}\right)^2}$$

Here $S_{\omega\omega}$ describes µ-wave resonator's resonance frequency fluctuations and S_{xx} (see Eq. (2.1)) is the mechanical displacement spectrum. Integrating over the frequency fluctuation spectrum gives:

$$\langle\delta\omega_\mathrm{r}^2\rangle = \int_0^\infty 2S_{\omega\omega}(\Omega)\frac{d\Omega}{2\pi} = \frac{1}{2}S_{\omega\omega}(\Omega_\mathrm{m})\Gamma_\mathrm{m} = 2g_\mathrm{m,0}^2\bar{n}_\mathrm{m}, \tag{2.13}$$

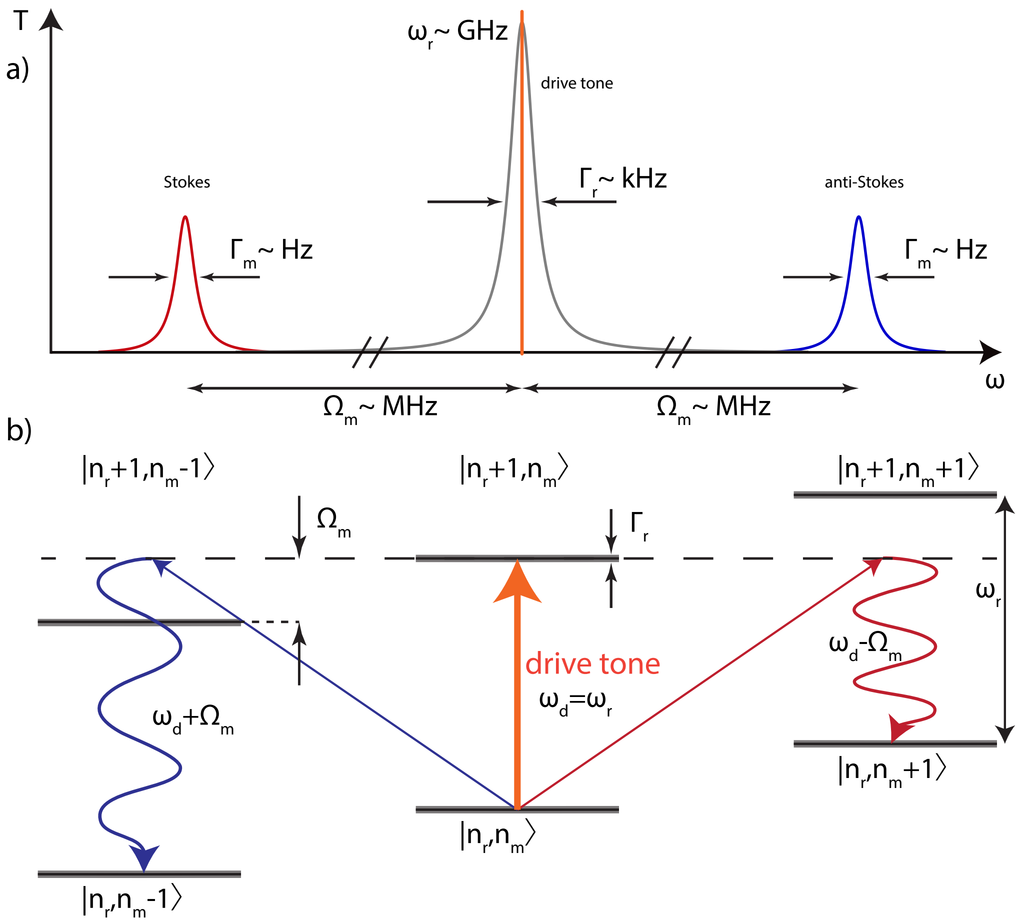

Figure 2.4: Schematic picture showing the correlations of a drive tone at zero detuning and the Stokes and anti-Stokes fields. a) By applying a strong drive tone at the resonator resonance frequency the Stokes(red) and anti-Stokes(blue) fields build up in the respective sidebands ($\mp\Omega_\mathrm{m}$), characteristic values for the parameters are given. The x-axis is not linear. b)The same effect as in a) is shown in a level scheme. Along the y-axis the number of µ-wave resonator excitations increases. The x-axis shows changes in the phonon occupation of the mechanical oscillator. By applying a strong drive tone at ω_r Stokes (red) and anti-Stokes (blue) scattering processes up(down)-convert the drive field by coupling to mechanical phonons. Both processes have the same probability, the mechanical resonator is undisturbed.

with the mean phonon number in the mechanical resonator $\bar{n}_\mathrm{m} = k_\mathrm{B}T/\hbar\Omega_\mathrm{m}$. In experiment however the power spectral density S_PP is typically recorded by a spectrum analyser, not the resonance frequency fluctuations. Therefore a transfer function $K(\Omega)$ has to be found to transduce the spectra [53]:

$$S_\mathrm{PP}(\Omega) = \frac{K(\Omega)}{\Omega^2} S_{\omega\omega}(\Omega) \approx \frac{K(\Omega)}{\Omega_\mathrm{m}^2} S_{\omega\omega}(\Omega). \tag{2.14}$$

This transfer function is determined experimentally by frequency noise calibration [53] in Sec. (4.1.4), and with a known transfer function equation (2.13) can be rewritten to:

$$g_{\mathrm{m},0}^2 = \frac{1}{4}\Gamma_{\mathrm{m}} S_{\mathrm{PP}}^{\mathrm{meas}} \frac{\Omega_{\mathrm{m}}^2}{K(\Omega)}. \tag{2.15}$$

2.3.3 EMIT & EMIA

In this section the theoretical background for electromechanically induced transparency (EMIT) and electromechanically induced absorption (EMIA) will be given. Staring with the Hamiltonian for the coupled system of μ-wave resonator and mechanical nanobeam given in Eq. (2.11) the system is discussed. To observe the interference effect EMIT a strong drive tone on the red sideband $\Delta = \omega_{\mathrm{d}} - \omega_{\mathrm{r}} = \Omega_{\mathrm{m}}$ is injected into the system. In addition a second weaker probe tone is used to scan the μ-wave resonator frequency $\omega_{\mathrm{p}} \simeq \omega_{\mathrm{d}} + \Omega$ schematically shown in Fig. (2.5). If this difference frequency matches the mechanical resonance frequency $\Omega = \Omega_{\mathrm{m}}$ the interference of anti-Stokes photons at the frequency $\omega_{\mathrm{d}} + \Omega_{\mathrm{m}}$ with the probe tone lead's to the generation of a transmission window around $\omega_{\mathrm{d}} + \Omega_{\mathrm{m}}$. The linewidth of this transmission window is given by the effective mechanical linewidth $\Gamma_{\mathrm{m,eff}}$. Stokes and anti-Stokes fields (shown in Fig.(2.5,b)) are induced at $\omega_{\mathrm{d}} \pm \Omega_{\mathrm{m}}$ around the driving tone. The Stokes line at $\omega_{\mathrm{d}} - \Omega_{\mathrm{m}}$ is strongly suppressed in this case due to the system being in the resolved sideband regime $\Omega_{\mathrm{m}} > \kappa_{\mathrm{ges,r}}$, which implies it is off resonant with the μ-wave resonator. The anti-Stokes line $\omega_{\mathrm{d}} + \Omega_{\mathrm{m}} \simeq \omega_{\mathrm{r}}$ however is enhanced because of an increase in anti-Stokes scattering events Eq. (2.9). The EMIT effect can be visualized by the level scheme shown in Fig. (2.5,a). In this scheme electromechanical states are shown as simplified product states $|n_{\mathrm{r}}, n_{\mathrm{m}}\rangle$ characterized by n_{r} resonator excitations (photons) and n_{m} mechanical excitations (phonons). A pure resonator excitation is depicted by a vertical arrow. By optimal red detuning the drive tone $\omega_{\mathrm{d}} = \omega_{\mathrm{r}} - \Omega_{\mathrm{m}}$ the photon number is increased while decreasing the phonon number, this is represented with a (blue) diagonal arrow. The photons from the drive field are upconverted by consuming a mechanical phonon and scatter into the anti-Stokes line $\omega_{\mathrm{d}} + \Omega_{\mathrm{m}}$ matching the resonance frequency of the probe tone closely. Now the upconverted drive field interferes with the probe field. Depending on the relative powers of the probe and drive field the interference can lead to a partial or complete extinction of the probe field inside the μ-wave resonator. This is detected as enhanced resonator transmission in experiments (see Sec. (4.1.5)).

The EMIA effect is observed in the case of blue detuning the drive tone optimal ($\Delta = \omega_{\mathrm{d}} - \omega_{\mathrm{r}} = +\Omega_{\mathrm{m}}$). This leads to similar interference effects as the EMIT with some differences. Similarly to EMIT, also for EMIA a strong drive tone at $\omega_{\mathrm{d}} = \omega_{\mathrm{r}} + \Omega_{\mathrm{m}}$ is send to the resonator while it is probed with a weaker probe tone at $\omega_{\mathrm{p}} = \Omega - \omega_{\mathrm{d}}$. Contrary to EMIT here the anti-Stokes is suppressed and the Stokes field is enhanced and similar to EMIA the downconverted drive field and the probe field interfere. This results in a

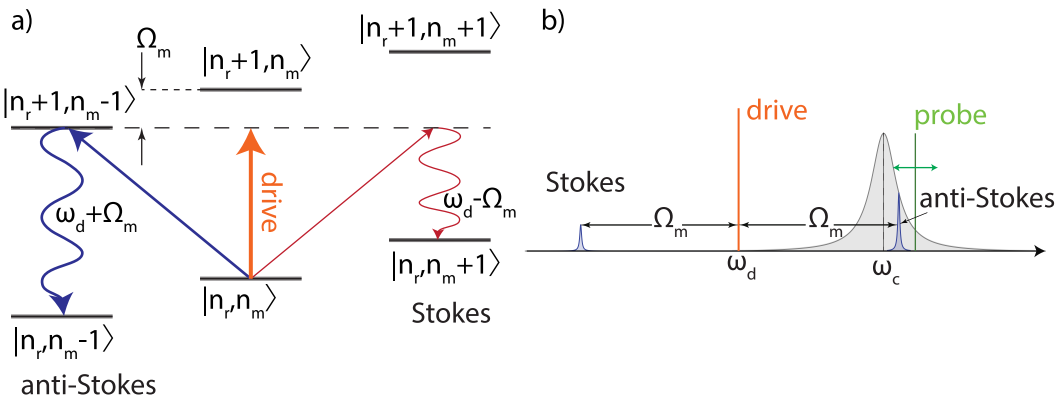

Figure 2.5: Schematic picture showing the coherences of a drive tone at optimal red detuning and the Stokes and anti-Stokes fields. b) By applying a strong drivetone at optimal red detuning $\omega_\mathrm{d} = \omega_\mathrm{r} - \Omega_\mathrm{m}$ the Stokes(red) and anti-Stokes(blue) fields build up. The Stokes field is strongly suppressed because it is far detuned from the resonator, the anti-Stokes field is at the resonator frequency and thus enhanced. a) The same effect as in a) is shown in a level scheme. Along the y-axis the number of µ-wave resonator excitations increases. The x-axis shows changes in the phonon occupation of the mechanical oscillator. By applying a strong drive tone at $\omega_\mathrm{r} - \Omega_\mathrm{m}$ Stokes (red) and anti-Stokes (blue) scattering processes up(down)-convert the drive field by coupling to mechanical phonons. The anti-Stokes is enhanced and the Stokes suppressed, a nonequilibrium between the processes leads to phonon reduction inside the mechanical oscillator.

partially or complete extinction of the probe field outside the µ-wave resonator. The interference between the now downconverted drive field and the probe field is constructive instead of destructive. In experiment this is observed as an enhanced absorption (see Sec. (4.1.5)). Also, due to the decreasing linewidth, the usable frequency window decreases for higher drive powers opposite to what happens in the case of EMIT (Eq. (2.10)).
The power transmission for such a system in the resolved sideband regime is given similarly to the undisturbed µ-wave resonator but now with modulations due to the coupling to the mechanical motion as [33]:

$$T = \left| 1 - \frac{\kappa_{\mathrm{ext,r}}/2}{-i\left(\Delta+\Omega\right) + \kappa_{\mathrm{ges,r}}/2 + \frac{g_{\mathrm{m},0}^2 \bar{n}_\mathrm{r}}{-(\Omega+\Omega_\mathrm{m}) - \Gamma_\mathrm{m}/2}} \right|^2 . \tag{2.16}$$

For optimal detuning ($\Delta = -\Omega_\mathrm{m}$ and $\Omega = \Omega_\mathrm{m}$) this simplifies to:

$$T = \left| \frac{1 - (\kappa_{\mathrm{ext,r}}/\kappa_{\mathrm{ges,r}}) - C}{1 - C} \right|^2 . \tag{2.17}$$

Here $C = 4g_{\mathrm{m},0}^2 \bar{n}_\mathrm{r}/\kappa_{\mathrm{ges,r}}\Gamma_\mathrm{m}$ is the cooperativity defined in Eq. (2.10) simplified for optimal detuning:

$$\Gamma_{\mathrm{m,eff}} = \Gamma_\mathrm{m} + 4g_{\mathrm{m},0}^2 \bar{n}_\mathrm{r}/\kappa_{\mathrm{ges,r}} = \Gamma_\mathrm{m}(1 + C).$$

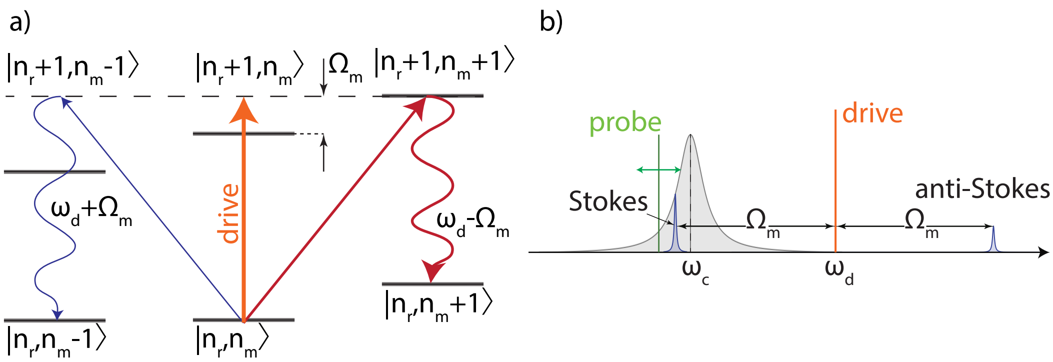

Figure 2.6: Schematic picture showing the coherences of a drive tone at optimal blue detuning and the Stokes and anti-Stokes fields. b) By applying a strong drive-tone at optimal blue detuning $\omega_\mathrm{d} = \omega_\mathrm{r} + \Omega_\mathrm{m}$ the Stokes(red) and anti-Stokes(blue) fields build up. The anti-Stokes field is strongly suppressed because it is far detuned from the resonator, the Stokes field is at the resonator frequency and thus enhanced. a) The same effect as in b) is shown in a level scheme. Along the y-axis the number of μ-wave resonator excitations increases. The x-axis shows changes in the phonon occupation of the mechanical oscillator. By applying a strong drive tone at $\omega_\mathrm{r} + \Omega_\mathrm{m}$ Stokes (red) and anti-Stokes (blue) scattering processes up(down)-convert the drive field by coupling to mechanical phonons. The Stokes is enhanced and the anti-Stokes suppressed, a nonequilibrium between the processes leads to a phonon increase inside the mechanical oscillator.

2.4 Josephson physics

The transmon qubit investigated in this thesis consist of a dc SQUID (**s**uperconducting **q**uantum **i**nterference **d**evice) which is shunted by an additional capacitor, sketched in Fig. (3.5,b)). Because the understanding of the transmon qubit depends strongly on the understanding of the dc SQUID and hence the physics of Josephson junctions, this section contains a short introduction to these two systems. Afterwards the transmon qubit itself is discussed.

2.4.1 Josephson junctions

A Josephson junction is defined as a tunnel junction of superconducting materials, separated by a thin insulating barrier [54–56]. The materials used for Josephson junctions in this work are aluminium as superconductor and aluminiumoxide as insulating barrier. In quantum mechanics the tunnelling through the insulating barrier is possible due to the finite overlap of the wave functions of the superconductors on both sides of the insulating layer. The coupling of the condensate states on either side of the junction was first described by Brian D. Josephson in 1962 [54]:

$$I = I_{\mathrm{c}} \sin\varphi \tag{2.18}$$

$$\frac{d\varphi}{dt} = \frac{2\pi V}{\Phi_0}. \tag{2.19}$$

Here I_{c} is the critical current of the junction and $\varphi = \Theta_{\mathrm{s},2} - \Theta_{\mathrm{s},1}$ is the phase difference between the macroscopic wave functions in the superconductors on either side of the junction. ϕ_0 is the magnetic flux quantum. I and V describe the phase dependent current and voltage in the system. The next step is to derive the Josephson inductance by inserting the time derivative of Eq. (2.18) into Eq. (2.19)[1]:

$$L_{\mathrm{J}} = V\left(\frac{dI}{dt}\right)^{-1} = \frac{\Phi_0}{2\pi I_{\mathrm{c}}\cos\varphi} = L_{\mathrm{J0}}\frac{1}{\cos\varphi},$$

where $L_{\mathrm{J0}} = \Phi_0/2\pi I_{\mathrm{c}}$ has been defined. Thus, the inductance of a Josephson junction is nonlinearly dependent on φ, wgich is of fundamental importance for building nonlinear oscillators, e.g. transmon qubits.

The energy stored in the Josephson inductance is the Josephson coupling energy [56]:

$$E_{\mathrm{J}}(\varphi) = E_{\mathrm{J0}}(1 - \cos(\varphi)) \tag{2.20}$$

with the maximal Josephson coupling energy $E_{\mathrm{J0}} = \Phi_0 I_{\mathrm{c}}/2\pi$. The energy stored in the junction (E_{J}) is usually regarded as a potential energy because it depends on the junction variable φ. The other energy present is dependent on $\dot\varphi$ and is therefore treated as a kinetic energy related to the capacitance of the junction. The two superconductors on either side of the insulating barrier can be imagined as two capacitor plates. The junction capacitance C_{J} and a corresponding energy stored in the electric field of the junction is given as:

$$E_{\mathrm{field}} = \frac{1}{2}C_{\mathrm{J}}V^2 = \frac{1}{2}C_{\mathrm{J}}\left(\frac{\Phi_0}{2\pi}\right)^2\dot\varphi^2.$$

The characteristic scale for this energy is the charge energy needed to move one elementary charge between the capacitor plates:

$$E_{\mathrm{C}} = \frac{e^2}{2C_{\mathrm{J}}}$$

[1] $L = V \cdot (dI/dt)^{-1}$; $dI/dt = d(I_{\mathrm{c}} \sin\varphi)dt = I_{\mathrm{c}}\cos\varphi\, d\varphi/dt$; $V = (d\varphi/dt)\,(\Phi_0/2\pi)$

The overall energy of the system is the sum of Josephson coupling energy and the electric field energy:

$$E = E_{\text{field}} + E_{\text{J}} = \frac{1}{2} C_{\text{J}} \left(\frac{\Phi_0}{2\pi} \right)^2 \dot{\varphi}^2 + E_{\text{J}0}(1 - \cos(\varphi)) \tag{2.21}$$

In this form the junction Hamiltonian can be identified equivalent to the Hamiltonian of a phase particle with a position φ and an effective mass $m_\varphi = C_{\text{J}}(\Phi_0/2\pi)^2$.

2.4.2 dc SQUID

In the section above it is shown that the energy of a Josephson junction is dependent on the phase difference φ between the two superconductors forming the junction. In experiment it is desirable to be able to tune this junction in situ [57]. This is possible by manipulating the phase difference externally. This is done by interrupting a superconducting loop with two Josephson junctions, this device is known as a direct current superconducting quantum interference device (dc-SQUID). Due to fluxoid quantisation the phase drop across the closed superconducting ring depends on the flux Φ threading the loop. By using SQUID loops with small areas and small critical currents a regime is chosen were the externally applied flux dominates over the self induced flux due to circulating currents. The phase difference across a Josephson junction depends on the phases of the macroscopic wave functions in the superconductors on each side and the potential wall due to the isolating barrier. This phase difference φ_{i} is assumed to be equal both Josephson junctions. The phase differences of the two junctions are coupled by the applied external flux and the overall phase quantisation simplifies using Kirchhoffs equations to [3]:

$$\varphi_1 - \varphi_2 = \frac{2\pi\Phi}{\Phi_0},$$

the difference between the individual phase quantisations. For an ideal equal Josephson junction also $I_{\text{c},1} = I_{\text{c},2} = I_{\text{c}}$ is assumed and the current-phase relation of the dc-SQUID simplifies to [3]:

$$I_{\text{S}} = I_1 + I_2 = 2I_{\text{c}} \left| \cos\left(\pi \frac{\Phi}{\Phi_0} \right) \right|.$$

Here, I_{S} is the current in the SQUID loop consisting of the currents across the Josephson junctions 1 and 2 with I_1 and I_2, respectively. This is similar to the current phase relation of a single Josephson junction and indeed the dc-SQUID behaves like a flux tunable Josephson junction. Its energy-phase relation is therefore given by Eq. (2.20) when replacing I_{c} by I_{S}.

2.4.3 Transmon qubit

The transmission line shunted plasma oscillation (transmon) qubit consists of a dc-SQUID shunted by a large capacitance C_{S} as depicted in Fig. (2.7). With this the Hamiltonian of

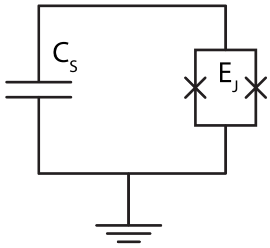

Figure 2.7: Equivalent circuit diagram of a transmon qubit. The transmon is described by an LC oscillator with a nonlinear inductance introduced by a SQUID loop with two Josephson junctions.

the qubit is similar to the one of the Josephson junction (Eq. (2.21)):

$$H_{\mathrm{T}} = \frac{1}{2} C_{\Sigma} \left(\frac{\Phi_0}{2\pi} \right)^2 \dot{\varphi}^2 + E_{\mathrm{J0}}(1 - \cos(\varphi)) \tag{2.22}$$

with the modified capacitance $C_{\Sigma} = C_{\mathrm{S}} + C_{\mathrm{J}}$. In Eq. (2.22) it is possible to identify a phase particle mass $m_p his = C_{\Sigma} \left(\frac{\Phi_0}{2\pi} \right)^2$ in a cosine potential. The momentum of this particle is defined as $p_{\varphi} = C_{\Sigma} \left(\frac{\Phi_0}{2\pi} \right)^2 \dot{\varphi}$. With this, φ and p_{φ} are conjugate variables. The large shunt capacitance effectively confines the phase particle to one specific minimum of the cosine function. This is possible by reducing the characteristic kinetic energy E_{C}, which depends inversely on the capacitance, relative to the characteristic potential energy E_{J0} which depends on the critical current of the single junctions. the tunneling across the walls of the potential wells scales with $\exp\left(-\sqrt{E_{\mathrm{J}}/E_{\mathrm{C}}}\right)$, this implies only small deviations from zero for the phase φ if $E_{\mathrm{J}} \gg E_{\mathrm{C}}$. These requirements are fulfilled for the transmon used in this thesis ($E_{\mathrm{J}}/E_{\mathrm{C}} \approx 75$ Sec. 4.2.3). Therefore the cosine potential can be approximated by the terms of its Taylor expansion up to fourth order and the Hamiltonian simplified to:

$$H_{\mathrm{T}} = \frac{1}{2} m_{\varphi} p_{\varphi}^2 + \frac{1}{2} E_{\mathrm{J0}} \varphi^2 - E_{\mathrm{J0}} \frac{\varphi^4}{24} + O(\varphi^6). \tag{2.23}$$

Neglecting the $O(\varphi^4)$ and $O(\varphi)^6$ terms in Eq. (2.23), the transition frequency can be calculated [19]:

$$\omega_{\mathrm{p}} = \frac{1}{\hbar} \sqrt{8 E_{\mathrm{J0}} E_{\mathrm{C}}}, \tag{2.24}$$

which is equivalent to the plasma frequency of a single junction. Due to the dc-SQUID in the transmon qubit, E_{J0} depends on the external magnetic flux penetrating the SQUID loop and is therefore tunable. By quantising the variables in Eq. (2.23) according to [35]:

$$\hat{\varphi} = \frac{1}{\sqrt{2}} \left(\frac{8E_{\mathrm{C}}}{E_{\mathrm{J0}}} \right)^{1/4} (\hat{c} + \hat{c}^{\dagger}) \,, \hat{p_{\varphi}} = i \frac{\hbar}{\sqrt{2}} \left(\frac{E_{\mathrm{J0}}}{8E_{\mathrm{C}}} \right)^{1/4} (\hat{c} - \hat{c}^{\dagger}), \tag{2.25}$$

the Hamiltonian of the transmon resembles the one of a quantised duffing oscillator [35]:

$$H_{\mathrm{T}} = \hbar\omega_{\mathrm{p}}\left(\hat{c}^{\dagger}\hat{c} + \frac{1}{2}\right) - \frac{E_{\mathrm{C}}}{12}(\hat{c} + \hat{c}^{\dagger})^4.$$

From this the energy levels of the qubit can be computed to [35]:

$$E_k = \hbar\omega_{\mathrm{p}}(k + \frac{1}{2}) - \frac{E_{\mathrm{C}}}{4}(2k^2 + 2k + 1)$$

where k denotes the qubit state ($0 = |g\rangle, 1 = |e\rangle$ ...), as well as the corresponding transition frequencies between neighbouring levels [35]:

$$\omega_{k,k+1} = (E_{k+1} - E_k)/\hbar = \omega_{\mathrm{p}} - E_{\mathrm{C}}/\hbar(k + 1).$$

2.4.4 Two level approximation of the transmon qubit

It is possible to treat a transmon qubit as an effective two level system if the anharmonicity between the two lowest levels $\alpha = \omega_{12} - \omega_{01} = -E_{\mathrm{C}}/\hbar$ is much larger than the linewidth of the qubit. This is true for the transmon used in this thesis (see Sec. (4.2)). In this case the qubit can be described similar to an artificial atom or spin 1/2 particle. The two levels chosen as eigenstates are the ground state $|g\rangle$ and the first excited state $|e\rangle$ of the qubit. Using this, the qubit Hamiltonian of Eq. (2.23) can be rewritten as [58]:

$$H_{\mathrm{T}} = \sum_{m=\mathrm{g,e}} E_m |m\rangle \langle m| = \sum_{m=\mathrm{g,e}} E_m \hat{\sigma}_m m.$$

By defining the qubit frequency $\omega_{\mathrm{q}} = (E_{\mathrm{e}} - E_{\mathrm{g}})/\hbar$, normalizing the energy and the Pauli matrix identities $\hat{\sigma}_{\mathrm{gg}} + \hat{\sigma}_{\mathrm{ee}} = \mathbb{I}_2$ and $\hat{\sigma}_z = \hat{\sigma}_{\mathrm{gg}} - \hat{\sigma}_{\mathrm{ee}} = |g\rangle\langle g| - |e\rangle\langle e|$ the Hamiltonian simplifies to that of an isolated spin 1/2 term:

$$H_{\mathrm{T}} = \frac{1}{2}\hbar\omega_{\mathrm{q}}\hat{\sigma}_z. \tag{2.26}$$

This simple form of Eq. (2.26) allows describing the physics of the transmon qubit coupled to a μ-wave resonator intuitively in terms of quantum electrodynamics.

2.5 Coupling between a transmon qubit and a superconducting μ-wave resonator

2.5.1 Jaynes-Cummings model

By integrating a transmon qubit into a μ-wave resonator an interaction between a photonic light field and a two level system is achieved. The dynamics of this system are

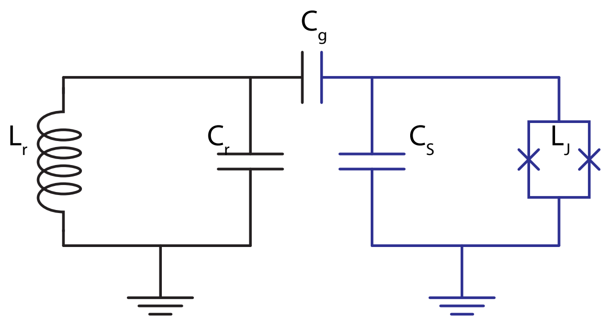

Figure 2.8: Circuit equivalent for the transmon qubit coupled to a µ-wave resonator. The harmonic (µ-wave) and nonlinear (transmon) LC oscillators are coupled by a gate capacitance Cgq.

usually described by the Jaynes-Cummings model. The coupling between the two can be understood by considering the transmon as an anharmonic LC-oscillator which can be driven by an AC electric field. This is enhanced by placing the qubit close to a voltage antinode of the µ-wave resonator, where the qubit can couple capacitively. The transmon and the resonator are coupled by an effective gate capacitance $C_{\mathrm{g,q}}$ also shown in the equivalent circuit diagram in Fig. (2.8). With the Eq. (2.25) and (2.26) the coupling term can be written to [35]:

$$\hat{H}_{\mathrm{int}} = C_{\mathrm{g,q}} \sqrt{\frac{\hbar\omega_{\mathrm{r}}}{2C_{\mathrm{r}}}} \frac{\hbar\Phi 2\pi}{\sqrt{2}C_{\Sigma,\mathrm{g}}\Phi_0} \left(\frac{E_{\mathrm{J0}}}{8E_{\mathrm{C}}}\right)^2 (\hat{a} - \hat{a}^\dagger)(\hat{\sigma}_- - \hat{\sigma}_+).$$

By using $\hbar\omega_{\mathrm{q}} = \sqrt{8E_{\mathrm{J0}}E_{\mathrm{C}}}$ and transforming the Hamiltonian is simplified to [35]:

$$\hat{H}_{\mathrm{int}} = \hbar \underbrace{\sqrt{\omega_{\mathrm{r}}\omega_{\mathrm{q}}} \frac{C_{\mathrm{g,q}}}{\sqrt{C_{\mathrm{r}}C_{\Sigma,\mathrm{g}}}}}_{g_{\mathrm{q}}} (\hat{a} - \hat{a}^\dagger)(\hat{\sigma}_- - \hat{\sigma}_+). \tag{2.27}$$

Here g_{q} is the capacitive coupling constant. Equation (2.27) describes the general dipole interaction Hamiltonian for coupling a microwave field and a two level system. For a more intuitive view the coupling is often written as [35]:

$$g_{\mathrm{q}} = \frac{2eV_{\mathrm{rms}}}{\sqrt{2}\hbar} \beta \left(\frac{E_{\mathrm{J0}}}{8E_{\mathrm{C}}}\right)^{1/4},$$

with e the electron charge, $V_{\mathrm{rms}} = \sqrt{\hbar\omega_{\mathrm{r}}/(2C_{\mathrm{r}})}$ the root mean square value of the resonator voltage and $\beta = C_{\mathrm{g,q}}/C_\Sigma$ the ratio of gate and transmon capacitance. The full Hamiltonian of the system is given as [35]:

$$\hat{H} = \hbar\omega_{\mathrm{r}} \left(\hat{a}^\dagger\hat{a} + \frac{1}{2}\right) + \frac{\hbar}{2}\omega_{\mathrm{q}}\hat{\sigma}_z + \hbar g_{\mathrm{q}}(\hat{a} - \hat{a}^\dagger)(\hat{\sigma}^- - \hat{\sigma}^+).$$

Here the first two terms describe the μ-wave resonator and qubit energies, the third term represents the interaction between qubit and resonator, allowing photon exchanges between them. The mixed terms like $\hat{a}\hat{\sigma}^-$ and $\hat{a}^\dagger\hat{\sigma}^+$ can be eliminated by using a rotating wave approximation. These terms are fast rotating $(\omega_\mathrm{q} + \omega_\mathrm{r})$ compared to the interaction rate g_q and are averaged out over one interaction period $1/g_\mathrm{q}$. With this the result is the Jaynes-Cummings-Hamiltonian [59]:

$$\hat{H} = \hbar\omega_\mathrm{r}\left(\hat{a}^\dagger\hat{a} + \frac{1}{2}\right) + \frac{\hbar}{2}\omega_\mathrm{q}\hat{\sigma}_z - \hbar g_\mathrm{q}(\hat{\sigma}^+\hat{a} + \hat{\sigma}^-\hat{a}^\dagger).$$

Here only a coherent exchange of photons is possible. Because of this interaction the qubit states ($|g\rangle$ and $|e\rangle$) and μ-wave resonator states ($|n\rangle$) are no longer eigenstates of the Hamiltonian (2.5.1). The states mix to new eigenstates depending on the detuning $\Delta = \omega_\mathrm{q} - \omega_\mathrm{r}$ [60]:

$$\begin{aligned} |n,-\rangle &= \cos(\theta_n)\,|n,g\rangle - \sin(\theta_n)\,|n-1,e\rangle \\ |n,+\rangle &= \sin(\theta_n)\,|n,g\rangle + \cos(\theta_n)\,|n-1,e\rangle \\ \theta_n &= \frac{1}{2}\arctan\left(\frac{2g_\mathrm{q}\sqrt{n}}{\Delta}\right) \end{aligned} \tag{2.28}$$

2.5.2 Resonant regime

The case of $\Delta \ll g_\mathrm{q}$ is called the resonant regime of the Jaynes-Cummings-Hamiltonian. Here the transition energies of the transmon qubit and the μ-wave resonator are matched and excitations can be exchanged. The eigenstates (Eq. (2.28)) form doublets, which depict symmetric and antisymmetric superpositions of the states:

$$|\pm,n\rangle = \frac{|n+1,g\rangle \pm |n,e\rangle}{\sqrt{2}}.$$

For $n = 0$ this corresponds to a single photon being exchanged coherently at the vacuum Rabi frequency $2g$, the energy levels are shown in Fig. (2.9). In experiment avoided crossings in the flux dependent spectrum of qubit and resonator are expected due to the formation of Jaynes-Cummings doublets. Due to interaction the doublets have an energy splitting of $2g_\mathrm{q}\sqrt{n}$. The qubit and the resonator exchange a photon with a rate of $2g_\mathrm{q}\sqrt{n}/2\pi$, this is usually called vacuum Rabi oscillation. Because the qubit frequency is tunable for a transmon qubit the resonant regime can be reached by tuning the external magnetic flux. This is experimentally shown in Sec. (4.2.1).

2.5.3 Dispersive regime

By tuning the transmon qubit far from the resonator $\Delta \gg g_\mathrm{q}$ the dispersive regime of the Jaynes-Cummings-Hamiltonian is reached. The energy difference is much larger than the

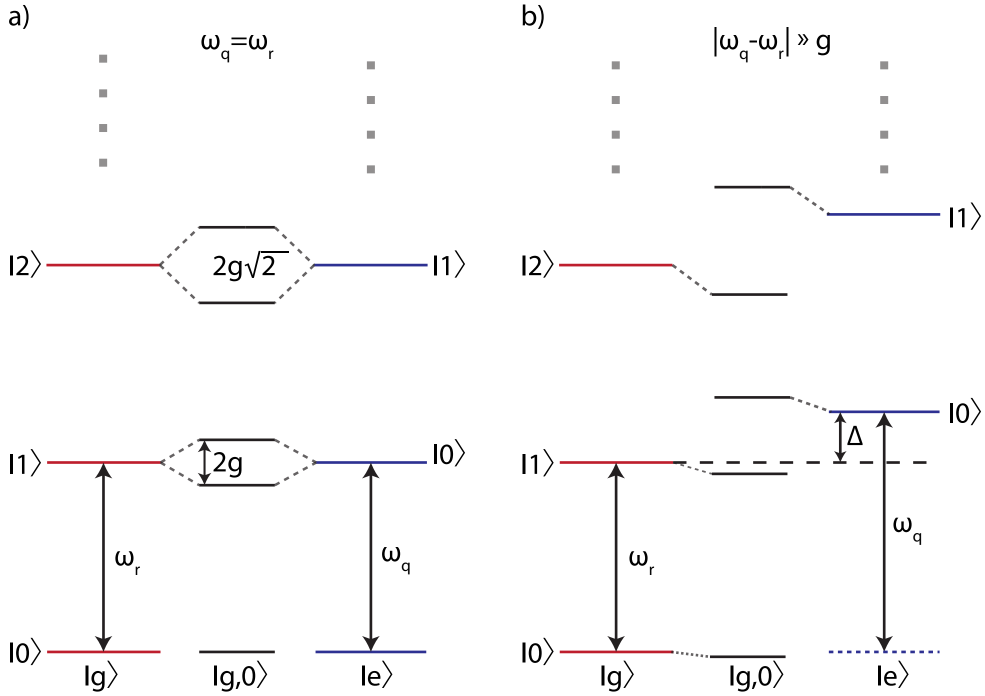

Figure 2.9: Level schema of the Jaynes-Cummings ladder in the resonant(a) and dispersive(b) regime. a) The transmon qubit and μ-wave resonator transition frequencies match, due to the strong coupling the degeneracy of the states is lifted by $2g_\mathrm{q}\sqrt{n+1}$, the resulting dressed states are observed as avoided crossings in measurements. b) In the dispersive regime of the Jaynes-Cummings-Hamiltonian no direct excitation exchanges between the respective eigenstates are possible, however they are still shifted due to the presence of the respective other system.

interaction energies and the eigenstates are nearly undisturbed resonator and qubit-like excitations. This suppresses the photon exchange strongly. Here, the Jaynes-Cummings-Hamiltonian can be expanded in g_q/Δ and approximated in first order [60]:

$$\hat{H} = \hbar\left[\omega_\mathrm{r} + \frac{g_\mathrm{q}^2}{\Delta\hat{\sigma}_z}\right]\left(\hat{a}^\dagger\hat{a} + \frac{1}{2}\right) + \frac{\hbar}{2}\omega_\mathrm{q}\hat{\sigma}_z.$$

Thus, if the transmon qubit is in its excited state, the resonators eigenfrequency shifts by $2g_\mathrm{q}^2/\Delta$ [35]. This is known as ac-Stark shift [61].

Chapter 3

Sample Fabrication and Experimental Techniques

3.1 Sample Fabrication

The fabrication of a hybrid sample with a transmon qubit and a nanomechanical beam coupled to one and only one micro-wave (μ-wave) resonator is, even though the fabrication of the individual parts is established and optimized at the WMI for several years, not a simple endeavor. Combining and altering fabrication steps up to the point of the feasibility of hybrid samples were a big part of this thesis.
The strategy to achieve this is as following: In a first step the single fabrication steps necessary for each individual part (transmon qubit, nanomechanical beam and μ-wave resonator) were investigated and possible interferences with the fabrication or existence of other parts searched. After identifying such steps, a main task was to change this fabrication step in a way that it would not interfere with the other systems any-more, but nevertheless perform the task it was designated. If a possible solution was found, it was tested experimentally. The final fabrication sequence and the methods used are described in this chapter. Furthermore, the used sample layouts and the experimental setups are presented.

3.1.1 Fabrication

The fabrication of all samples startswith a cleaned $6 \times 10\,\mathrm{mm}^2$ highly resistive silicon chip shown in Fig. (3.1,a)). In a first step the sample is coated with negative resist, see Fig. (3.2,b)). The desired design is written into the resist using a *NanoBeam Limited* nB5 Electron Beam Lithography System (e-Lithography) Fig. (3.2,c)). After exposure the resist was developed, see Fig. (3.2,d)). Using electron-beam evaporation (EVAP) a $100\,\mathrm{nm}$ aluminum film was deposited on the sample with orthogonal incidence to the sample surface as displayed in Fig. (3.2,e)). After a lift-off process, the sample consists of a aluminum μ-wave resonator and a nanomechanical beam surrounded by an Al ground plane Fig. (3.2,f)) and Fig. (3.1,b)). The nanomechanical beam is integrated into the

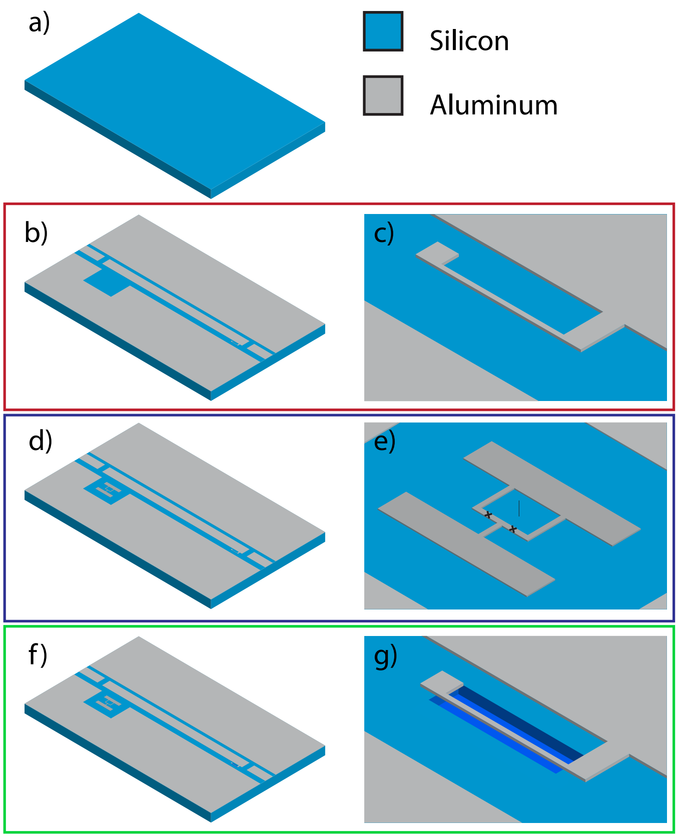

Figure 3.1: Overview of the fabrication sequence. a) Cleaned silicon substrate. b) Substrate with added μ-wave resonator and pocket for the transmon. c) Close up of nanobeam integrated into the μ-wave resonator. d) Substrate with μ-wave resonator, nanobeam and included transmon qubit. e) Close up of the transmon qubit in its pocket next to the resonator. f) Finished sample with released mechanical beam. g) Close up of the released nanobeam. The steps are divided into three parts: Patterning of the μ-wave resonator and nanobeam (red frame), Adding the transmon qubit (blue frame) and releasing the nanobeam (green frame).

μ-wave resonator on one end Fig. (3.1,c)), at the other end, a pocket is patterned in the ground plane. This is were the transmon qubit will be added later. The sample is annealed to generate a tensile stress in the aluminum thinfilm. For exact fabrication sequences and further information about used methods and devices please see the Appendix A. In the second step a transmon qubit was added to the sample. To this end, the sample was coated with a double layer of positive resist with different sensitivities to electron exposure shown in Fig. (3.3,b)). Next the transmon qubit is patterned using ebeam lithography, Fig. (3.3,c)). After development Fig. (3.3 ,d),e) and f)), the upper resist layer is used as a mask for the evaporation whereas the lower resist layer has a higher sensitivity and acts as a spacer between mask and substrate. This spacing is needed for the shadow-evaporation process. In this process the sample is tilted during a first aluminum EVAP step to project the resist pattern onto the substrate (Fig. (3.3,g))). After an insulating aluminumoxide layer has been grown by exposure to oxygen Fig. (3.3,h)), a second layer of aluminum is

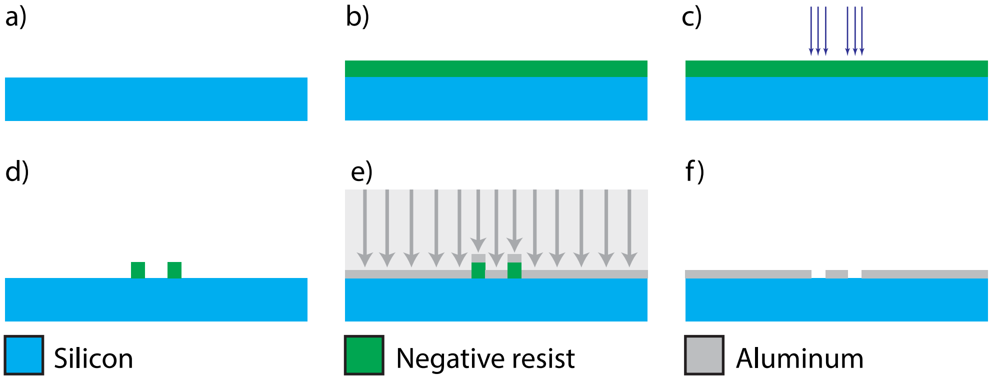

Figure 3.2: Schematic picture of the electron beam lithography and evaporation sequence used to fabricate the μ-wave resonator and nanobeam. a) Cleaned silicon substrate. b) Substrate coated with negative resist. c) Exposure to the electron beam for patterning μ-wave resonator and nanobeam. d) Substrate with developed resist. e) Evaporation of aluminum on top of the substrate and resist. f) Finished aluminum μ-wave resonator and nanobeam after lift-off.

deposited via EVAP, this time however tilted by the opposite angle Fig. (3.3,i)). With this technique localized sandwich structures of aluminum, aluminum-oxide and aluminum are patterned Fig. (3.3,j)), which form the Josephson Junctions within the transmon qubit Fig. (3.1,d),e)). In the final step the nanomechanical beam has to be released. For this the sample is coated with a single layer of positive resist to define an etching window by e-Litho. After development, the silicon substrate below the nanomechanical beam is removed via reactive ion etching (RIE) in a *Oxford Instruments Plasmalab 80 Plus*. Next, the electron beam resist is removed using critical point drying (CPD) to avoid the destruction of the nanomechanical beam due to capillary forces during the evaporation of the solvent.

3.1.2 Yield improvements for nanomechanical beams

For the final layout, as proposed theoretically, only one nanomechanical beam on each sample is planned. At the beginning of this thesis project the fabrication process of those only had a yield of about 50% for the proposed layout. This is attributed to capillary forces during the last resist removal step, as mentioned before. This fabrication step becomes especially problematic, when the gap between nanomechanical beam and groundplane is small. Initially, when trying to combine the nanobeam fabrication steps with the one for transmon qubits the yield dropped to $18\% - 30\%$ if the structuring of the transmon was done last. When the nanomechanical beam is released in the last step the yield is 50% as before. As this impracticable, different methods to increase the beam yield were tried. The biggest impact was achieved by using a CPD process for the final drying. By this the yield for the used layouts, was improved to $> 80\%$ and thus in the range where single nanobeam samples become in reach. If the CPD process would be done automated, unlike

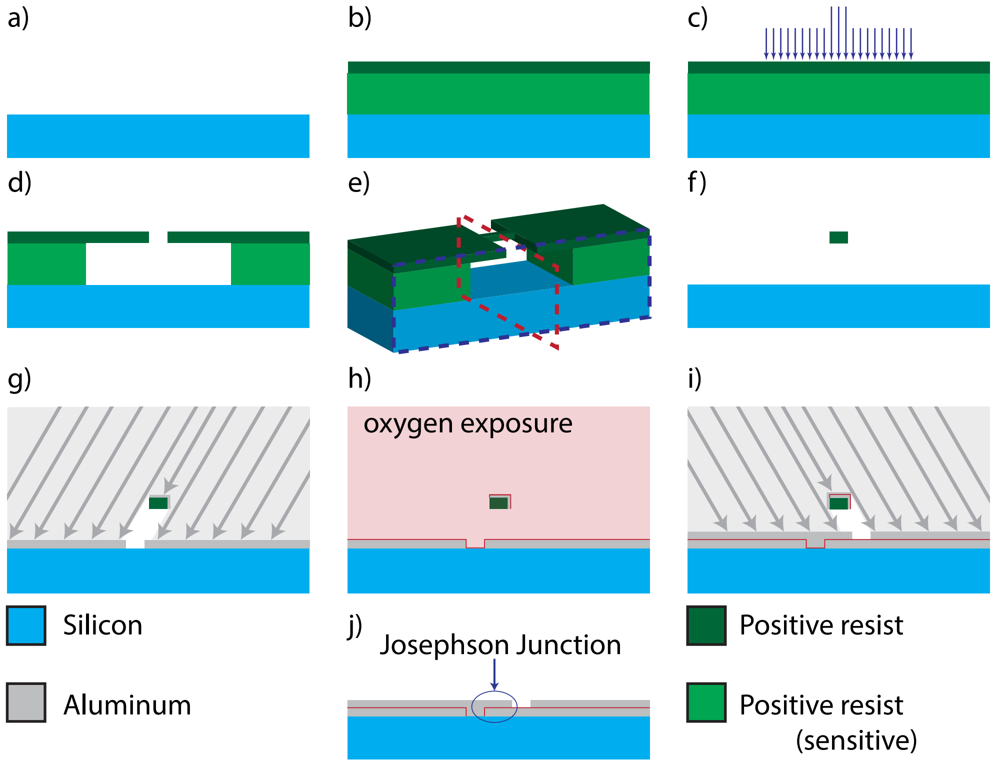

Figure 3.3: Schematic picture of the shadow-evaporation sequence used to pattern the transmon qubit including Josephson Junctions. a) Cleaned silicon substrate. b) Substrate coated with a double layer of positive resist with different sensitivity (low sensitivity above high sensitivity). c) Exposure to the electron beam for patterning. d) Substrate with developed resist. e) Change of perspective, the view on the substrate is turned by 90° to allow better understanding of the process of structuring Josephson Junctions. f) Substrate with resist bridge. g) Evaporation of aluminum at an angle of 17°. h) Oxidation of the Al film surface. i) Evaporation of aluminum at an opposite angle of (−17°). j) Finished aluminum structure with embedded JJ after lift-off.

the manual process used for these samples App. (A.2.2), a further yield improvement is likely.

3.2 Layout and Simulation

Within the scope of this thesis, different sample layouts have been realized. First, samples for understanding and measuring nanomechanical beams were fabricated and the impact of changes in different fabrication steps was determined. As a second line of approach samples for understanding and measuring transmon qubits were fabricated and their compatibility with the methods used for fabricating nanomechanical beams were tested. Finally samples with both, nanomechanical resonators and a transmon qubit on one and only one chip were fabricated. In this section a presentation of the used samples will be given and layout choices will be commented.

3.2.1 Sample layout #1 (μ-wave resonator & nanobeam)

The first sample layout to be discussed is the one designed for measuring and understanding the fabrication processes of mechanical beams integrated in a superconducting coplanar wave-guide μ-wave resonator. It consists of eight $\lambda/4$ μ-wave resonators capacitively coupled

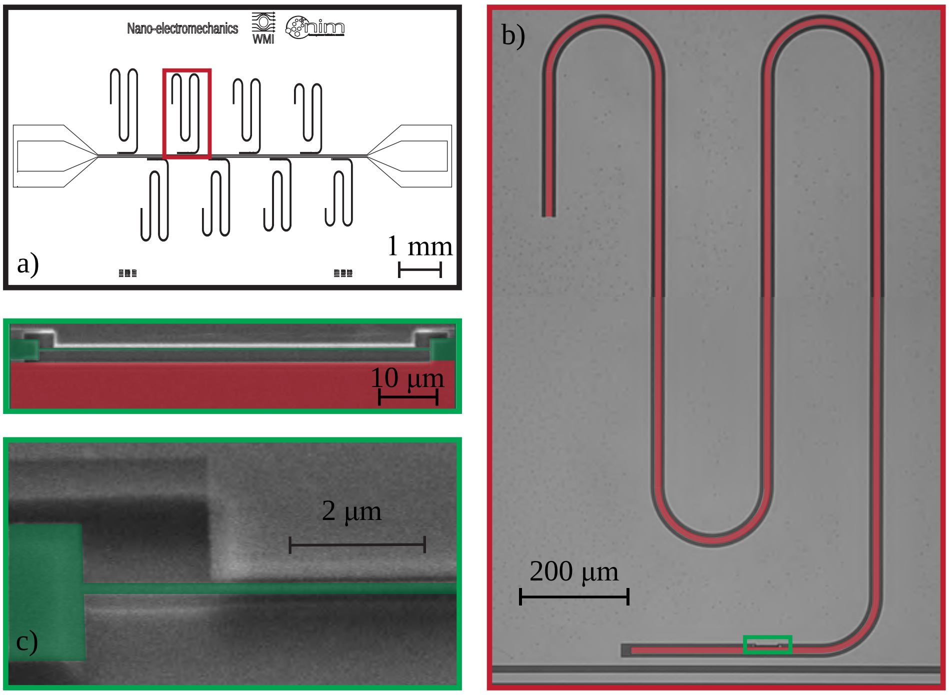

Figure 3.4: Graphic of the sample layout for layout # samples with different magnifications. a) Pattern of the whole sample chip with $\lambda/4$ wavelength μ-wave resonators coupled to a central transmission line. b) Micrograph of a single μ-wave resonator (colored in red) with embedded mechanical resonator. c) SEM pictures of the nanomechanical beam(colored in green),as whole (upper picture) and a tilted close up of the clamping area (lower picture).

to a central transmission line shown in Fig. (3.4 ,a)). The transmission line is designed to match the impedance $Z_0 = 50\,\Omega$ of standard μ-wave cables. The μ-wave resonators are positioned alternating on either side of the transmission line and have different eigenfrequencies ω_r ranging from $6 - 8\,$GHz Fig. (3.4,a)). Into six of them, nanomechanical beams are embedded. The μ-wave resonators are coupled to the transmission line on one end, and shorted to the ground on the other Fig. (3.4,b)). Embedded into the resonator on one end, close to the voltage-antinode, is a nanomechanical beam, see Fig. (3.4,c)). The nanomechanical beam length varies between $40 - 60\,\mu$m on the sample. Depending on the beamlength the width of the beam varies between $100 - 150\,$nm as does the gap to

the ground plane, from $100 - 120\,\mathrm{nm}$. The height of the nanomechanical beam is$100\,\mathrm{nm}$, defined by the thickness of the evaporated Al layer. The lower SEM picture in Fig. (3.4,c)) shows that the beam is under-etched by at least double of its own height and can move freely.
This sample layout was used to measure the nanomechanical beam at room temperature as well as at mK temperatures in a dilution refrigerator.

3.2.2 Sample layout #2 (transmon qubit & µ-wave resonator)

This sample type was designed for measuring transmon qubits and understanding their fabrication process. The transmon-layout is composed of a $\lambda/2$ µ-wave resonator capac-

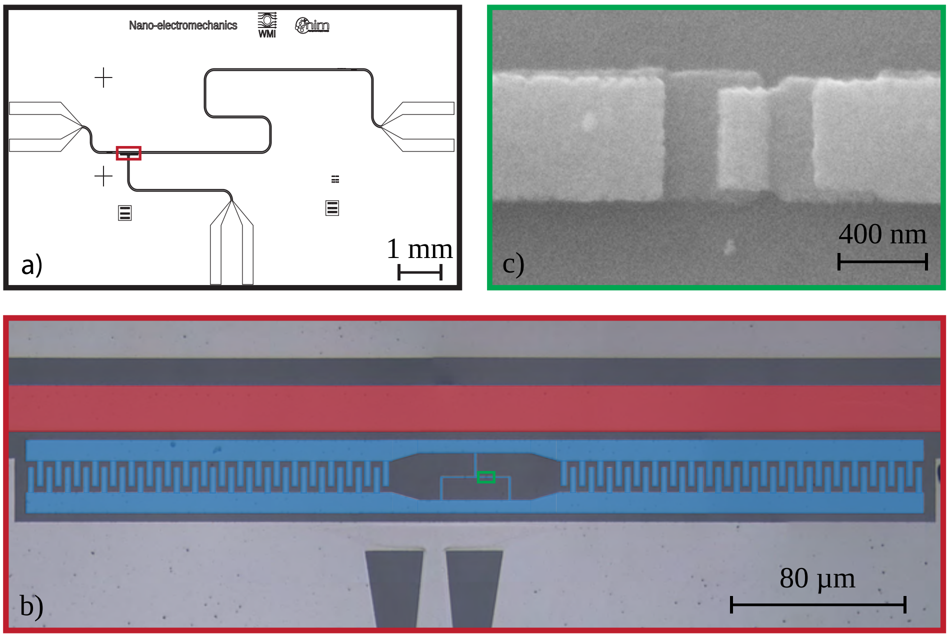

Figure 3.5: Graphic of the sample layout # 2 with different magnifications. a) Pattern of the whole sample chip with transmon coupled to $\lambda/2$ µ-wave resonator and separate µ-wave antenna leading to the transmon. b) Micrograph of the a transmon qubit (colored in blue). c) SEM picture of a JJ embedded in the transmon.

itively coupled to a µ-wave input and output line, as illustrated in Fig. (3.5,a)). The resonator and input/output lines are designed to match $50\,\Omega$ µ-wave cables. On one end of the µ-wave resonator a transmon qubit is coupled to the resonator capacitively by placing its capacitor plates parallel to the resonator. The transmon qubit Fig. (3.5,b)) consists of two capacitor plates forming a interdigital capacitor. The capacitor plates are shunted by a loop containing two Josephson Junctions Fig. (3.5,c)), the junction area is

$200 \times 400\,\mu\mathrm{m}^2$ each. The distance between the capacitor planes and their width define the charging energy E_C of the transmon qubit whereas the length of the capacitor planes and the distance between the transmon qubit and the resonator determine the coupling g/π between the two of them. The area of the Josephson Junctions is essential for their critical current I_C and therefore for the Josephson Energy E_J of the qubit. Various values for design parameters where investigated with *CST Studio Suite* (App. (A.3)) to determine the different impact on physical properties like E_C and g.

3.2.3 Sample layout #3 (μ-wave resonator & transmon qubit & nanobeam)

This sample layout was used to fabricate a device with a transmon qubit and a nanomechanical resonator coupled to one and the same μ-wave resonator Fig. (3.6,a)). For a proof of principle, a transmon qubit Fig. (3.6,b)) and a nanomechanical beam Fig. (3.6,c)) are located on opposite ends of the $\lambda/2$ resonator. The transmon qubit has the same layout as the one used in layout # 2 to enable direct comparison of the samples. Two nanomechanical beams with lengths of 50 μm and 60 μm are embedded into the μ-wave resonator. This also allows direct comparison to the beam samples which have the same beam lengths.

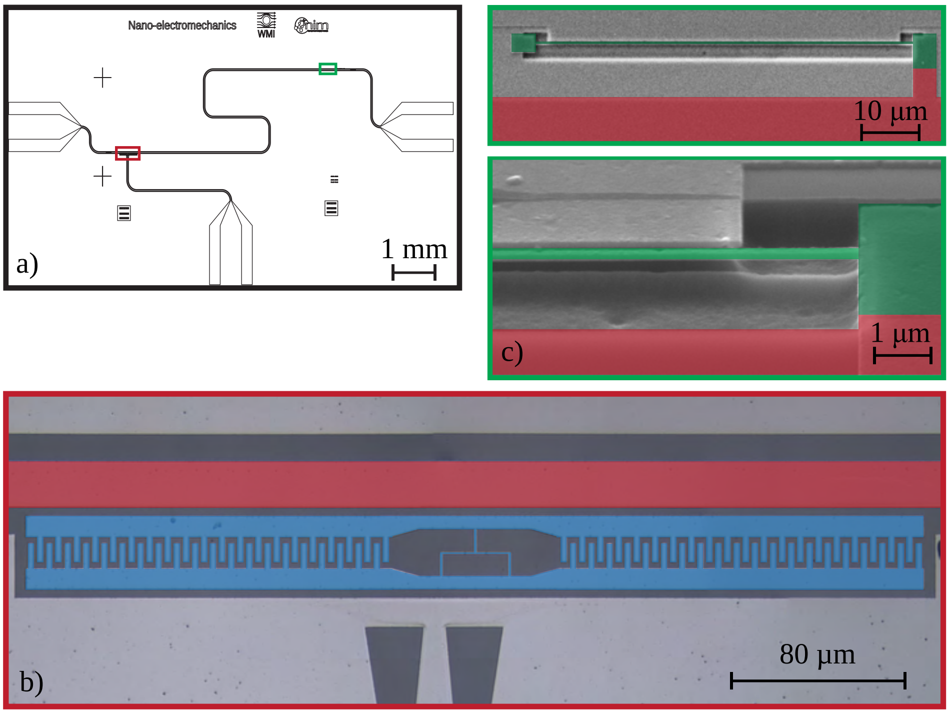

Figure 3.6: Graphic of the sample layout # 3 at different magnifications. a) Pattern of the whole sample chip with transmon and mechanical beam coupled to the same $\lambda/2$ μ-wave resonator. b) Micrograph of a the transmon qubit (colored in blue). c) SEM pictures of the the nanomechanical beam as whole (upper picture) and tilted close up of the clamping area (lower picture).

3.3 Setups

In this section the experimental setups and their wiring will be introduced. This includes the room temperature optical interferometer and the two used dilution refrigerators

Triton^{TM} and Kermit.

3.3.1 Optical Interferometer

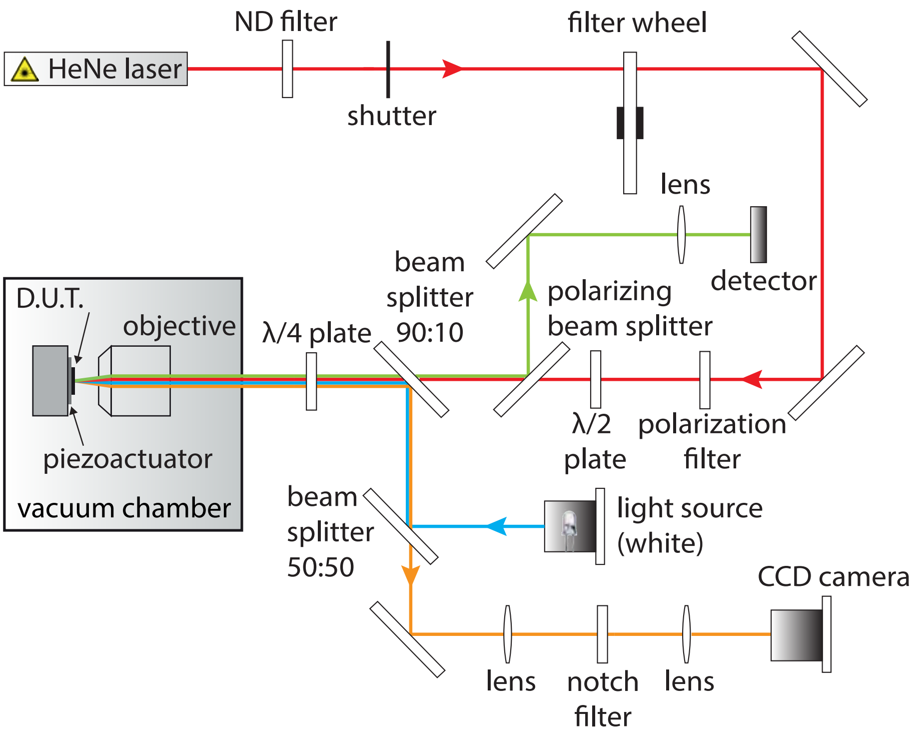

Figure 3.7: Schematic picture of the optical interferometer used for room temperature measurements of the mechanical beams. The sample is located in a vacuum chamber. Mechanical motion is excited by a piezoactuator, on to which the sample is mounted. To monitor the motion of the nanobeam, the laser spot is focused on the sample and the reflected laser light is detected with a photodiode. Optical access to the sample is given by a white light source and a CCD camera.

To characterize the nanomechanical beams at room temperature an optical interferometer is used. This has the advantage of fast measurements to quickly check if the beams are working and determine their eigenfrequencies.The optical interferometer Fig. (3.7) consists of a vacuum chamber integrated in an optical table because the air would damp the mechanical oscillation. A laser beam is guided from its source to the sample by different mirrors, beam splitters and polarizing plates. This allows to decouple the laser beam entering the vacuum chamber from the one exiting it after being reflected from the sample. The reflected laser beam is guided to a detector.
The main components are a polarizing beam splitter to enable the readout via detector and the objective that focuses the beam onto the sample. To position and move the sample relative to the laser beam a piezo-stage is used, this also allows for changes in the focal length between sample and objective.The correct positioning of the sample can be

observed via a CCD camera supported by a white light source. A filter wheel the laser and path allows control of the intensity on the sample, while a notch filter in the white light path is used to avoid damage of the CCD camera by the laser beam. A piezoactuator mounted below the sample can excite it mechanically via a μ-wave signal.

3.3.2 Triton dilution fridge

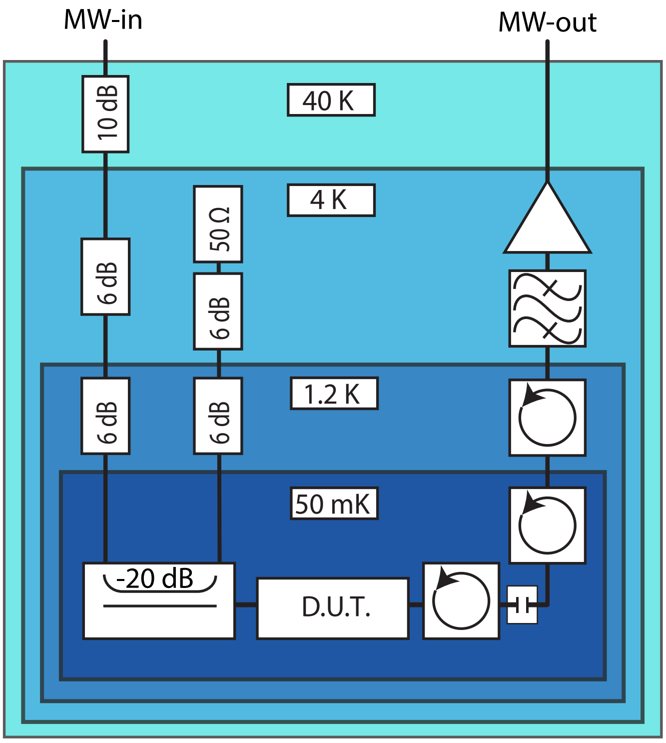

Figure 3.8: Schematic picture of the *Oxford Instruments* Triton^{TM} fridge with μ-wave paths and devices. The sample is mounted at the mixing chamber stage, which is operated at temperatures between $40 - 400\,$mK.

One of the used dilution refrigerators is a *Oxford Instruments* Triton^{TM} fridge (Triton) Fig. (3.8). It is a dry dilution fridge and its used at temperatures from 40 mK to 400 mK. The μ-wave input signal is attenuated at each temperature stage to suppress thermal noise. Together with losses in the μ-wave cables, the total attenuation along the input line is about 55dB (See Sec. (4.1.5)). On the outgoing path three circulators and a DC-block reduce the backscattering of noise photons. A bandpass filter and a cold high-electron-mobility-transistor (HEMT) amplifier at the 4 K stage are used to amplify the signal by 28 dB to the output port. Within the thesis this fridge is referred to as "Fridge #1 ".

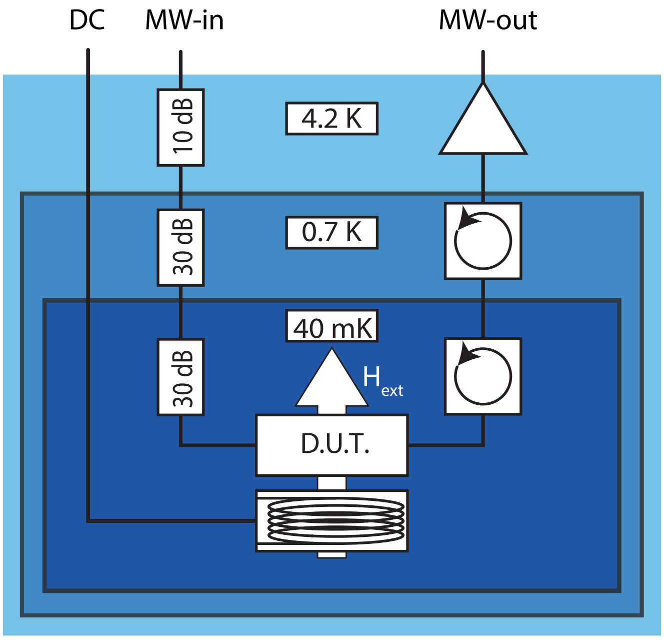

Figure 3.9: Schematic picture of the Kermit fridge with μ-wave paths and devices. The sample is mounted at the mixing chamber ($\approx 40\,\mathrm{mK}$).

3.3.3 Kermit dilution fridge

The other used dilution refrigerator is the home-made fridge called Kermit, which is schematically shown in Fig. (3.9). This is a LHe pre-cooled dilution fridge, with a base temperature of about 40 mK. On the input μ-wave path 70 dB of attenuation are integrated, the μ-wave cables generate another 15 dB of attenuation. On the output path two circulators reduce backscattering of photons and a HEMT amplifier amplifies the signal by 28 dB. In addition to the μ-wave paths a DC line leads to the sample stage, where it is connected to a superconducting coil attached to the sample box. This allows to apply an external magnetic field to the sample. To reduce field noise from the environment, the whole sample stage is shielded by an aluminum cylinder. Within the thesis this fridge is referred to as "Fridge #2 "

Chapter 4

Experimental results

This chapter discusses the experimental findings of this thesis. The measurements study the different samples with the layouts introduced in Sec. (3.2). At first characterization measurements of the mechanical nanobeam and the µ-wave resonator are shown. The nanobeam was characterized at room temperature with optical interferometry (Sec. (4.1.1)), for this the samples *nBAl1.1* and *nBSi3.3* were used. The µ-wave resonator was characterized inside fridge # 1 with microwave spectroscopy (Sec. (4.1.2)), here the sample *nBSi3.7* was used. The same sample was also used to investigate the coupled nanobeam/µ-wave resonator hybrid system, this will be discussed in Sec. (4.1.3). The last part of this chapter is dedicated to the measurements on the transmon qubit coupled to a µ-wave resonator. In this section, the transmon qubit was characterized using transmon spectroscopy techniques. The sample was measured three times with intermediate fabrication process steps, this was done to investigate the impact of specific fabrication processes on the transmon qubit, here only one sample, *nbSiAl2.4*, was used.

4.1 Sample layout #1 (µ-wave resonator & nanomechanical beam)

Before measurements on hybrid devices were performed, the isolated constituents were characterized. The mechanical beam can be investigated at room temperatures, without it being coupled to a µ-wave resonator. The µ-wave resonator, which is measured at mK temperatures is characterized using a measurement scheme, where the impact of the nanobeam can be neglected.

Room temperature optical interferometry is a quick method to check the functionality if a mechanical nanobeam resonator and to determine its resonance frequency Ω_{m}. This allows to predict Ω_{m} at low temperatures .

Pre-Characterization of the µ-wave resonator is necessary to identify its core parameters like its resonance frequency ω_{r}, the linewidth $\kappa_{\mathrm{ges,r}}$, and the drive amplitude when it becomes non-linear. These parameters are necessary for certain calibrations used later on. Here fore, also the internal and external loss rates ($\kappa_{\mathrm{ext,r}}$,$\kappa_{\mathrm{int,r}}$) have to be known.

After the pre-characterization, the coupled nanomechanical beam and μ-wave resonator system was investigated at mK temperatures. Within the section concerning the measurements performed in the millikelvin temperature range, the nanobeam's mechanical resonance frequency Ω_m and linewidth Γ_m as well as the electromechanical vacuum coupling $g_{\mathrm{m},0}$ between nanomechanical beam and μ-wave resonator are investigated.
In the last part of this section, the effects of electromechanically induced transparency (EMIT) and electromechanically induced absorption (EMIT) generated by coupling mechanisms between a detuned drive tone and a weak probe tone mediated by electromechanical coupling to the nanobeam are studied.

4.1.1 Characterisation of the nanomechanical beam at room temperature

The parameters characterising the nanomechanical beam are known from fabrication and literature. The length l can be measured by SEM microscopy and the density for the used aluminium $\rho_\mathrm{Al} = 2700\,\frac{\mathrm{kg}}{\mathrm{m}^3}$ [38] is also known. According to Sec. (2.1.2), the resonance frequency of the fundamental vibrational mode of a tensile stressed nanomechanical beam is given by:

$$\Omega_\mathrm{m} = \frac{\pi}{l}\sqrt{\frac{\sigma_\mathrm{Al,eff}}{\rho_\mathrm{Al}}}. \tag{4.1}$$

The one parameter to be determined is the tensile stress $\sigma_\mathrm{Al,eff}$ in the nanomechanical beam. The latter depends on the deposition and the annealing steps during the fabrication. Thus if $\sigma_\mathrm{Al,eff}$ can be determined and demonstrated to be constant for the chosen fabrication parameters, nanomechanical beams with specific Ω_m can be designed and built. Goal of the measurements presented in this section is to determine the mechanical resonance frequency at room temperature and calculate the tensile stress in the nanomechanical beam. Further the Q-factor, as defined in Eq. (2.4), of a nanomechanical beam will be determined at room temperature. It directly depends on the tensile stress, because higher tensile stress results in a higher resonance frequency and smaller linewidth for an unchanged beam length and thus gives a possibility to increase the Q-factor. High tensile stresses of the nanomechanical beam result in a higher electromechanical vacuum coupling to the μ-wave resonator $g_{\mathrm{m},0}$ Sec. (4.1.4). This is due to the fact, that with higher Q-factors, it is possible to increase the beam length and still remain within the resolved sideband regime. The longer the mechanical beam the bigger the beam capacitance $C_\mathrm{g,m}$ and respectively the impact on the electromagnetic μ-wave resonator and thus the electromechanical vacuum coupling $g_{\mathrm{m},0}$.

Setup

To characterize the nanomechanical beam at room temperatures the optical interferometer described in Sec. (3.3.1) is used. The piezoactuator on which the sample is mounted is driven by a RF (radio frequency) signal from a vector network analyzer (VNA). The photodiode, detecting the reflected laser light, is read out by the same VNA.
During the measurements the VNA sweeps the drive tone frequency applied to the piezoactuator while monitoring the intensity of the laser light via the optical detector. If the eigenfrequency Ω_m is resonant with the drive frequency, the motion of the nanobeam will be excited resulting in the modulation of the reflected laser light (again Ω_m). This is caused by interfering parts of the laser beam. One part of the laser beam is, due to its diameter, reflected by the substrate surrounding the mechanical beam, the other part is reflected by the mechanical beam itself. When not in resonance, the mechanical beam moves with the same frequency and amplitude like the whole sample, because it is driven by the piezoactuator. If Ω_m is met by the drive frequency applied to the piezoactuator, the motional amplitude of the nanomechanical beam will change and thus the laser light reflected as it will have a different pathlength than the part of the laser light reflected by the substrate. The laser light of both paths combines and interferes. The change in intensity caused by this interference is observed via the detector. With this technique, both, the in-plane and the out-of-plane movement of the nanomechanical beam can be detected, however the out-of-plane motion is easier to detect because its modulation amplitude is larger.

Measurements

In the experiment data like Fig. (4.1,a)) is acquired. Both mechanical modes are visible and for a beamlength of $l_1 = 60\,\mu$m shown in Fig. (4.1). From the measurements presented in Fig. (4.1,b),c)) the resonance frequencies and linewidths of the mechanical resonance are extracted by a Lorentzian fit:

$$T = \left[iA + \frac{\Gamma_\mathrm{m}}{i\left(\omega - \Omega_\mathrm{m}\right) + \frac{\Gamma_\mathrm{m}}{2}} \right] \times B + C.$$

The out-of-plane motion has a resonance frequency of $\Omega_\mathrm{m,oop} = 1.59\,\mathrm{MHz}$. The in plane motion has a higher frequency due to geometric reasons $\Omega_\mathrm{m,ip} = 1.62\,\mathrm{MHz}$. A second measured beam with a length of $l_2 = 36\,\mu$m shows resonance at $\Omega_\mathrm{m,oop} = 2.87\,\mathrm{MHz}$ and $\Omega_\mathrm{m,ip} = 2.95\,\mathrm{MHz}$. Both beams have been fabricated the same way, thus the tensile stress should be equal. Using Eq. (4.1) the tensile stress for the out-of-plane motion is $\sigma_\mathrm{Al,eff,oop} = (105 \pm 8)\,\mathrm{MPa}$. For the in plane motion $\sigma_\mathrm{Al,eff,oop} = (110 \pm 8)\,\mathrm{MPa}$ is calculated. The measured linewidths are $\Gamma_\mathrm{m} = 1900\,\mathrm{Hz}$ for the out-of-plane mode and $\Gamma_\mathrm{m} = 656\,\mathrm{Hz}$ for the in-plane mode. The discrepancy between the two values can be accounted to

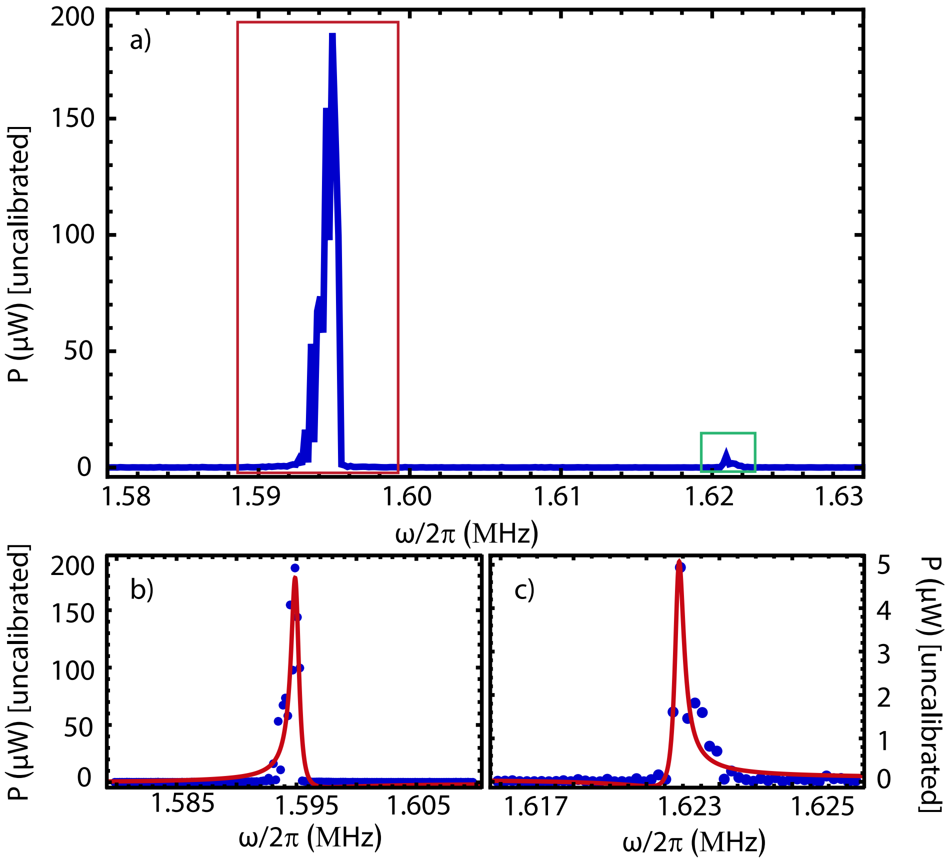

Figure 4.1: Data acquired by interferometric measurements of a nanomechanical beam. a) Spectrum showing in plane (green frame) and out of plane (red frame) motion of the nanobeam. b) Zoom to the out-of-plane vibrational mode (red frame) and Lorentzian fit (red line). c) In-plane vibrational mode of the nanobeam (green frame) and Lorentzian fit (red line). All measurements were made with an drive tone amplitude of −8 dBm at the VNA output and a measurement bandwidth of 1 Hz.

asymmetries in the beams cross-section, these are not considered in Eq. (4.1) but can be explained by more explicit formulas [36, 62]. Because of this and because of the fact that in later cold measurements mainly the in-plane motion will be important the quality factor of the nanomechanical beam is calculated with the linewidth and resonance frequency of the in plane mode. The quality factor is calculated as $Q = \frac{\Omega_\mathrm{m}}{\Gamma_\mathrm{m}} \approx 2500$.
These values ($Q \approx 2500$ and $\sigma_\mathrm{Al,eff,oop} = (105 \pm 8)\,\mathrm{MPa}$) are small compared to other material systems like pre-stressed silicone nitride beams, which are known to have tensile stresses of 830 MPa and quality factors of $Q \approx 160.000$ at room temperature [63] for comparable beam lengths. Double layer systems which combine pre-stressed silicon nitride with an aluminium layer show a quality factor of $Q \approx 13.000$ [34], in this particular system the tensile stress in the aluminium was calculated as $\sigma_\mathrm{Al} = (306\,\mathrm{MPa}$ [34]. This shows that the tensile stress inside the aluminum can be increased by using double layer systems, however this uses more complex fabrication techniques, as not only the mechanical

nanobeam is concerned within this thesis but also adding a superconducting qubit to the system. Enhancing the tensile stress via a double layer system is therefore not considered as it would lead to further complications with the fabrication of the superconducting qubit. Nevertheless the ratio $\Omega_\mathrm{m}/\Gamma_\mathrm{r} \geq 2$ and thus well in the resolved-sideband regime, not considering that the tensile stress is even larger at low temperatures.

4.1.2 Characterisation of the superconducting μ-wave resonator

The goal of this section is to characterize the μ-wave resonator. The basic properties of a μ-wave resonator are its resonance frequency ω_r and its linewidth $\kappa_\mathrm{ges,r} = \kappa_\mathrm{int,r} + \kappa_\mathrm{ext,r}$ which depends on the internal and external photon loss rates *gammaresint* and $\Gamma_\mathrm{r,ext}$, respectively. With the loss rates known it is possible to calculate the quality factor Q (Eq. (2.4)) of the μ-wave resonator which allows comparison between resonators with different resonance frequencies. Similar to the quality factor Q also internal (Q_int) and external quality factor (Q_ext) can be defined. An important parameter used to quantify the relation between the different loss rates is $\eta_\mathrm{r} = \frac{\Gamma_\mathrm{r,ext}}{\Gamma_\mathrm{r,int}}$. The optimal value is $\eta_\mathrm{r} = 1/2$, here the μ-wave resonator is critically coupled and the highest contrast in measurements is achieved.

Setup

The measurements on the $\lambda/4$ μ-wave resonator are performed in fridge # 1 Sec. (3.3.2). For the single tone measurements the setup consist of a VNA (*Rohde& Schwarz ZVB8*) which is connected to the in and output lines of the fridge. A schematic picture of the setup is shown in Fig. (4.2). The frequency (ω) send to the sample is varied over a frequency interval and the transmitted amplitude is monitored by the same VNA. If the probe frequency is resonant with the eigenfrequency of the μ-wave resonator frequency ($\omega_\mathrm{p} = \omega_\mathrm{r}$) the transmission through the central transmission line decreases because the signal is coupled into the μ-wave resonator and partially dissipated to the ground plane (Eq. 2.2)). For this the ratio between external and internal loss rate is important, as it describes which parts of the signal are dissipated to the environment and the transmission line respectively.

Measurements

Experimentally obtained data is shown in Fig. (4.3) for different probe-tone powers P_d. This was done to investigate the power dependence of resonance frequency (ω_r) and linewidth (Γ_r). The data in Fig. (App. B.2) shows the power dependence of the resonance frequency. For a probe power between -20 dBm and -60 dBm the resonance frequency remains constant within the accuracy of the measurement. For lower probe powers the signal to noise ratio decreases and for higher probe powers Fig. (App. B.3) shows that

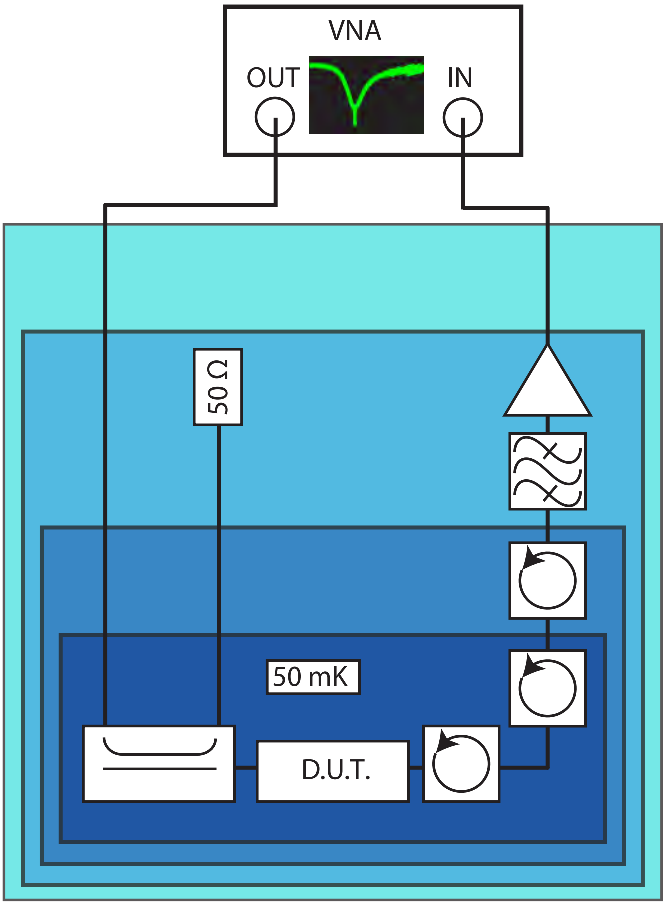

Figure 4.2: Schematic picture of the measurement setup for single tone measurements. The VNA output port is connected with the input line of the fridge and the output line of the fridge is connected to the input port of the VNA. The fridge schema shown here is simplified for exact internal fridge paths and setup please see Sec. (3.3.2).

the linewidth is increased. Therefore, the parameters are extracted at a probe power of $-20\,\mathrm{dBm}$. *Deng et al.* [64] showed that the data obtained by a transmission measurement with the setup used can be described by:

$$T = \left| \frac{1 + \frac{2i(\omega - \omega_\mathrm{r})}{\kappa_\mathrm{int,r}}}{1 + \frac{\kappa_\mathrm{ext,r}}{\kappa_\mathrm{int,r}} + \frac{2i(\omega - \omega_\mathrm{r})}{\kappa_\mathrm{int,r}} + \frac{i\omega_\mathrm{r}}{A\kappa_\mathrm{int,r}}} \right|^2$$

Here A is a parameter used to characterize the asymmetry of the transmission with respect to the resonance frequency, this asymmetry can be explained by impedance mismatches along the transmission line or at the connectors. The fit gives the values $\omega_\mathrm{r}/2\pi = 6.1578\,\mathrm{GHz}$ and a linewidth of $\Gamma_\mathrm{r}/2\pi = 925\,\mathrm{MHz}$ consisting of an internal loss rate $\Gamma_\mathrm{r,int}/2\pi = 674\,\mathrm{MHz}$ and and external loss rate of $\Gamma_\mathrm{r,ext}/2\pi = 251\,\mathrm{MHz}$. The quality factor is $Q = 6655$.

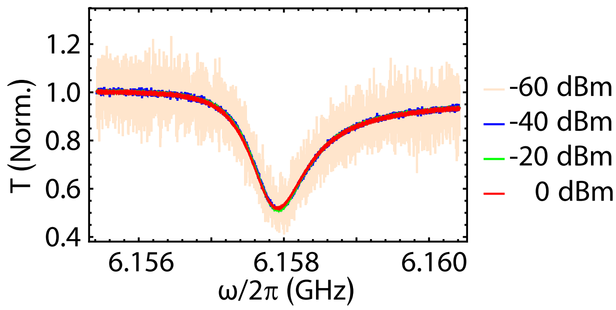

Figure 4.3: In this graph the single tone measurement is plotted for different probe powers for sample layout # 1. The measurements show that the signal to noise ration decreases for lower probe power, the eigenfrequency of the resonator ω_{r} and its linewidth Γ_{r} however do not change significantly. The data is normalized to the undisturbed transmission through the probed transmission line.

4.1.3 The coupled nanomechanical beam/μ-wave resonator system

In this part, the measurements of the nanomechanical beam coupled to the superconducting μ-wave resonator are discussed. The goal of these measurements is to characterize the nanomechanical beam at millikelvin temperatures and to investigate the interactions between the nanomechanical beam and the μ-wave resonator. In the first section the relevant parameters of the nanomechanical beam are determined with a homodyne detection setup. These are the mechanical resonance frequency Ω_{m} and linewidth Γ_{m}. Further, the electromechanical vacuum coupling $g_{\mathrm{m},0}$, between the nanomechanical beam and the μ-wave resonator is extracted.
In the second part, two tone spectroscopy will be used to access an other class of physical phenomena such as electromechanically induced transparency (EMIT) and the electromechanically induced absorption (EMIA). All measurements in this part were conducted using fridge # 1.

4.1.4 Determination of the electromechanical vacuum coupling $g_{\mathrm{m},0}$

In this section a homodyne detection setup is used to determine the mechanical resonance frequency Ω_{m} and the undisturbed natural linewidth Γ_{m} of the nanobeam. The electromechanical vacuum coupling $g_{\mathrm{m},0}$ is determined by spectral analysis of the mechanical displacement spectrum.

Setup

To determine the resonance frequency and natural linewidth of the nanomechanical beam, the μ-wave resonator is driven at its resonance frequency or zero detuning $\Delta = 0$, while measuring the sidebands of the mechanical motion of the nanobeam using a homodyne setup. This allows to observe the Brownian motion of the nanobeam without it being actively driven or suppressed by the interaction with the µ-wave resonator (Sec. (2.3.1)). The setup is shown schematically in Fig. (4.4). It consist of a *Rohde&Schwarz SMF 100A* µ-wave source (SMF) which provides the microwave signal. This signal is split up into a measurement and reference signal. The measurement signal is fed into the microwave input line of the fridge # 1 described in Sec. (3.3.2). The signal is guided to the sample via the internal wiring and attenuation. The signal is modulated by interactions with the sample and exits the fridge via the output line. The signal is then guided to the rf-port of an IQ-mixer. The reference path leads from the power divider to the local oscillator (LO) port of the IQ-mixer, the used microwave cables have the same electrical length as the signal line, including the wiring inside the fridge. A phase shifter in this path is used to phase-match the signals arriving at the LO and RF ports of the IQ mixer. To ensure the correct signal amplitude at the LO port the signal from the SMF is set to the according value, the signal towards the input line of the fridge is attenuated accordingly for the measurements. The IQ-mixer downconverts the measured signal with the original drive signal, thus the sidebands of the mechanical motion in the microwave transmission are mapped to the frequency Ω_m. This signal is amplified and detected with a *Rohde&Schwarz FSV30 Signal Analyzer* (SA).

For further theoretical explanations please see Sec. (2.3.1).

Measurements

Figure (4.5,a)), shows the recorded homodyne detection spectrum for a drive frequency of $\omega_\mathrm{d} = \omega_\mathrm{r} + \Omega_\mathrm{m}$ with a drive power of 1.15 nW (at the sample input). Here, the probe tone with a carrier frequency $\omega_\mathrm{d} = \omega_\mathrm{r}$ is frequency modulated for calibration purposes explained later. A Lorentzian fit to the sideband of the mechanical motion Fig. (4.5,b)) allows extraction of the resonance frequency $\Omega_\mathrm{m}/2\pi = 4.87\,\mathrm{MHz}$ and a linewidth of $\Gamma_\mathrm{m}/2\pi = 32\,\mathrm{Hz}$ at 400 mK. This temperature was chosen, because here the signal due to Brownian motion is bigger and because the thermalisation of the sample is ensured. Measurements at 70 mK show a linewidth of $\Gamma_\mathrm{m}/2\pi = 13\,\mathrm{Hz}$. Figure (4.6) shows the mechanical linewidth versus the fridge temperature. In the higher temperature range $(400 - 100\,\mathrm{mK})$ the expected linear dependence is visible. Below 100 mK the linewidth seems to stay constant this also is true for the spectral intensity namely the area below the peak. This behaviour is presently attributed to the absence of thermalization of the nanobeam with the sample, this is often reported in literature. In the part of the temperature range where the linewidth and spectral intensity behave linear a extrapolation to lower temperatures can be made. This predicts what happens if the phonon number in the resonator decreases linearly with decreasing temperature and predicts a natural linewidth of $\Gamma_\mathrm{m}/2\pi = 8\,\mathrm{Hz}$ for temperatures close to 0 K. Corresponding to a Q factor of $Q = \frac{\Omega_\mathrm{m}}{\Gamma_\mathrm{m}} = 608 \times 10^3$. The last value to be extracted from these homodyne measurements is the electromechanical vacuum coupling $g_\mathrm{m,0}$ between the µ-wave resonator and the nanobeam. One way to do this is via frequency noise calibration. The approach is to send

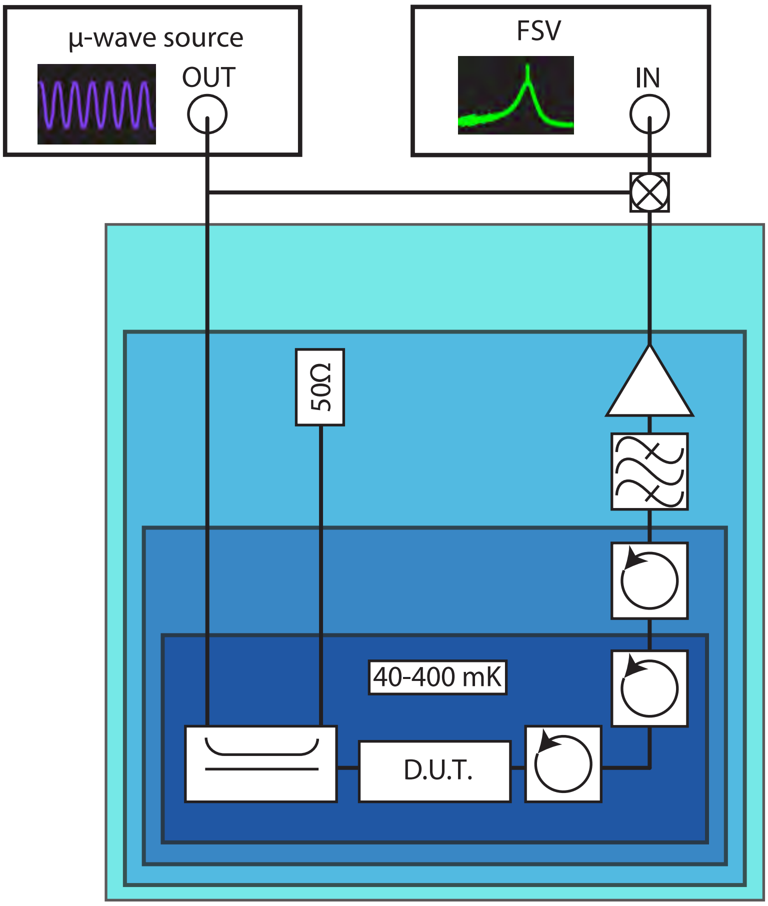

Figure 4.4: Schematic picture of the setup used for homodyne measurements. A microwave signal is generated by a μ-wave source and split between the microwave input line of the fridge and a μ-wave cable leading to the local oscillator (LO) port of an IQ-mixer. The signal from the microwave output line of the fridge is connected to the radio frequency (RF) port of the IQ-mixer. The output of the IQ-mixer is monitored with a spectrum analyzer. The fridge schema shown here is simplified, for exact internal fridge paths and setup please see Sec. (3.3.2).

a well defined signal to the sample, this signal experiences the same phase shift inside the μ-wave resonator as the signal resulting from mechanical motion. This allows to cancel the resonator response function extract the transfer function $K(\Omega_{\mathrm{mod}})$. This is realized experimentally by applying a frequency modulation to the microwave signal used for the homodyne detection, the resulting frequency peak is visible in Fig. (4.5,a)). The transfer function of the μ-wave resonator can be determined [53]:

$$K(\Omega_{\mathrm{mod}}) \approx \frac{2\mathrm{ENBW} S_{\mathrm{PP}}^{\mathrm{meas}}(\Omega_{\mathrm{mod}})}{\phi_0^2} = 0.052\,\mathrm{W/s}.$$

With the modulation tone close to the mechanical sideband and both within the linewidth of the μ-wave resonator the respective transfer functions can be assumed to be similar

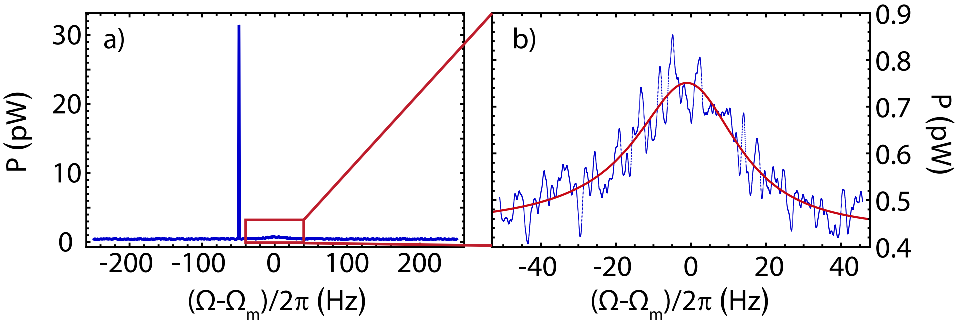

Figure 4.5: Experimental data from the homodyne detection setup of the mechanical sideband centered around the mechanical resonance frequency $\Omega_\mathrm{m} = 4.87\,\mathrm{MHz}$ of the nanobeam ($l = 50\,\mu\mathrm{m}$). a) Shows the complete measurement with modulation tone at $\Omega = \Omega_\mathrm{m} - 50\,\mathrm{Hz}$. b) Shows a zoom in to the mechanical sideband with a Lorentzian fit(red) which was used to extract the relevant parameters.

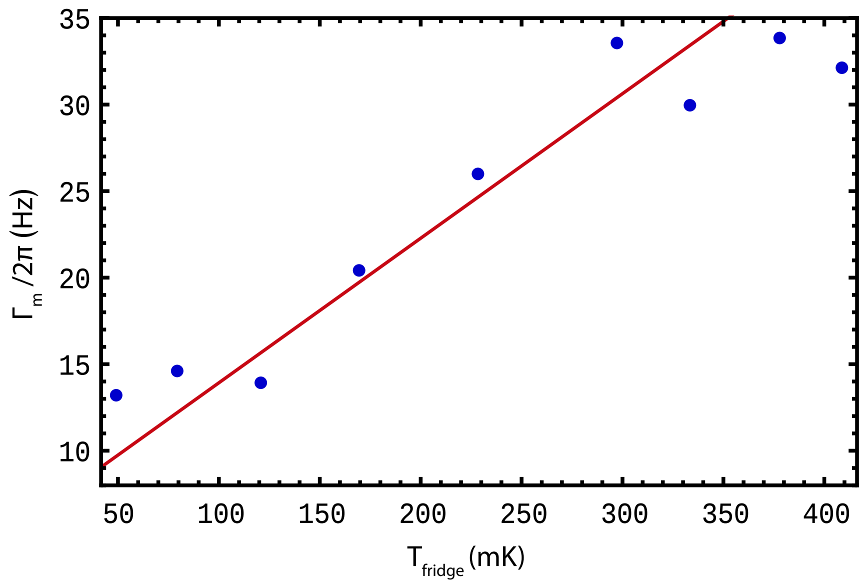

Figure 4.6: Extracted natural linewidths depending on the fridge temperature, above 100 mK a linear dependence is visible. Below 100 mK the linewidth remains constant, this may be due to discrepancies between measured and actual temperature at the nanobeam.

$K(\Omega_\mathrm{mod}) \approx K(\omega_\mathrm{r}) \approx K(\Omega_\mathrm{m})$[53]. Now the vacuum coupling can be calculated as shown in Eq. (2.15):

$$g_{\mathrm{m},0}^2 = \frac{1}{2\bar{n}_\mathrm{m}} \frac{\phi_0^2 \Omega_\mathrm{mod}^2}{2} \frac{S_\mathrm{PP}^\mathrm{meas}(\Omega_\mathrm{m})\Gamma_\mathrm{m}/4}{S_\mathrm{PP}^\mathrm{meas}(\Omega_\mathrm{mod})\mathrm{ENBW}}.$$

Here the modulation frequency was set as $\Omega_\mathrm{mod}/2\pi = \Omega_\mathrm{m}/2\pi - 50\,\mathrm{Hz}$ (see Fig. (4.5,a))) and a modulation depth of $\Omega_\mathrm{md}/2\pi = 80\,\mathrm{Hz}$, equivalent to a phase modulation with a modulation index $\phi_0 = \Omega_\mathrm{md}/\Omega_\mathrm{mod} \approx 16{,}4 \times 10^{-6}$. ENBW $= 1\,\mathrm{Hz}$ describes the detection bandwidth and the mean phonon occupation of the nanomechanical beam $\bar{n}_\mathrm{m} = \frac{k_\mathrm{B}T}{\hbar\Omega_\mathrm{m}}$ is calculated from the fridge temperature. The spectra $S_\mathrm{PP}^\mathrm{meas}(\Omega_\mathrm{mod})$ and $S_\mathrm{PP}^\mathrm{meas}(\Omega_\mathrm{m})$ can be extracted from the measurement Fig. (4.5,a),b)). With this the electromechanical vacuum coupling is calculated as $g_{\mathrm{m},0}/2\pi = 0.699\,\mathrm{Hz}$. In this measurement no back-action of the drive field onto the mechanical mode is possible, however such back-action might be caused by a mocrowave field of the right spectrum. Such a noise signal would influence the temperature used to calculate the mean phonon number ($T = T_{\mathrm{fridge}} + T_{\mathrm{BA}}$). The offset temperature T_{BA} could result in an error for the determination of $g_{\mathrm{m},0}$, as the sample is assumed to be in thermal equilibrium with T_{fridge}. In other words $\bar{n}_{\mathrm{m}}$ would be affected by such an offset temperature and therefore also $g_{\mathrm{m},0}$ would be underestimated. To eliminate this source of uncertainty an other approach to extract $g_{\mathrm{m},0}$ is chosen to verify the data. According to Eq. (2.13) with $T = T_{\mathrm{fridge}} + T_{\mathrm{BA}}$:

$$\delta\omega_{\mathrm{r}}^2 = \frac{2g_{\mathrm{m},0}^2 k_{\mathrm{B}}}{\hbar} \times (T_{\mathrm{fridge}} + T_{\mathrm{BA}})\,.$$

This frequency shift ($\delta\omega_{\mathrm{r}}^2$) can be calculated from the measured $S_{\mathrm{PP}}^{\mathrm{meas}}(\Omega_{\mathrm{m}})$ by using Eq. (2.14)and Eq. (2.13). Here the transfer function $K(\Omega_{\mathrm{m}})$ derived from the frequency noise calibration measurements is used. A plot showing the integrated mechanical beam fluctuations in units of the shift of the μ-wave resonator frequency $\delta\omega_{\mathrm{r}}^2$ is shown in Fig. (4.7). The red line is a linear fit to the data points and gives a electromechanical vacuum coupling of $g_{\mathrm{m},0}/2\pi = 0.67\,\mathrm{Hz}$ in agreement with the previous measurements. The spread in the data points in this graph can be explained by uncertainties in the determination of the temperature. The temperature measurement inside the fridge an uncertainty due to measurement methods, also there is the uncertainty in how exact the temperature of the nanomechanical beam can be determined with a temperature sensor outside the sample box. It is possible, especially for lower temperatures, that the local temperature of the nanomechanical beam differs from the temperature measured outside the sample box.

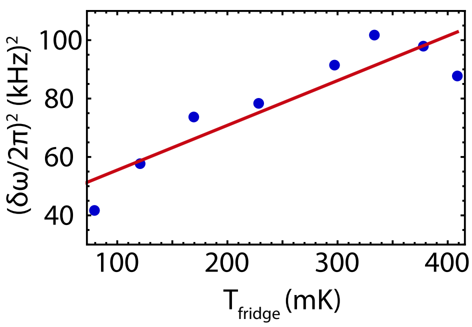

Figure 4.7: Frequency fluctuation spectrum of the μ-wave resonator, induced by thermal nanobeam motion at different fridge temperatures. The red line is a linear fit to the data points. An electromechanical vacuum coupling of $g_{\mathrm{m},0}/2\pi = 0.67\,\mathrm{Hz}$ is extracted.

4.1.5 EMIT & EMIA

In this section the results of investigating the sample with two tone spectroscopy will be studied. Goal of this measurements was to show that EMIA and EMIT could be performed with the sample and to which extend this is possible. The probe and drive signals were detuned to the red (EMIT) and blue (EMIA) sidebands by the mechanical resonance frequency. The interference between probe and drive signals via the electromechanical coupling to the nanomechanical beam inside the μ-wave resonator were investigated and discussed.

Setup

The setup used for two-tone measurements on the mechanical beam consists of a *Rohde&Schwarz SMF 100A* μ-wave source (SMF) and a *Rohde& Schwarz ZVB8* vector network analyzer (VNA). A simplified schematic picture of the setup is given in Fig. (4.8). The output signals from the SMF and VNA are combined and guided to the sample via the microwave input line of fridge # 1. The microwave output line of the fridge is connected to the VNA. This allows to probe the transmission of the μ-wave resonator around its resonance frequency with the VNA while applying a strong red- or blue-detuned drive tone.

Measurements

Fig. (4.9) shows the transmission spectrum of the μ-wave resonator in EMIT configuration i.e. with a strong ($0.1\,\mu$W) ideally red-detuned drive tone with a frequency $\omega = \omega_\mathrm{r} - \Omega_\mathrm{m}$ or $\Delta = -\Omega_\mathrm{m}$. Within the broad microwave absorption dip attributed to the μ-wave resonator, a narrow transmission window located at a probe frequency $\omega_\mathrm{p}/2\pi = 6.158\,\mathrm{GHz}$ with a linewidth given by the effective mechanical damping rate $\Gamma_\mathrm{m,eff}$ is observed. This transmission window (Eq. (2.3.3)) is a result of the interference of the anti-Stokes photons with the weak probe tone explained in Sec. (2.3.3). for this detuning, only the anti-Stokes process is is visible due to the spectra selectivity of the μ-wave resonator. The anti-Stokes is amplified (Eq. (2.9)). As a consequence of this the the effective linewidth of the nanobeam changes to:

$$\Gamma_\mathrm{m,eff} = \Gamma_\mathrm{m} + \Gamma_\mathrm{ba}$$

with the backaction-induced linewidth broadening Γ_ba. This results in an increased linewidth that depends on the detuning. The visibility of the anti-Stokes field is limited by the envelope of the μ-wave resonator response function. Equation (2.9) indicates a dependence of the anti-Stokes process of the mean resonator population $\bar{n}_\mathrm{r}$. Thus the changes in the linewidth and transmission amplitude should be stronger for optimal mechanical detuning ($\Delta = -\Omega_\mathrm{m}$). The changes linewidth and transmission amplitude are described by Eq. (2.10) and Eq. (2.16), thus close to unity transmission is expected for

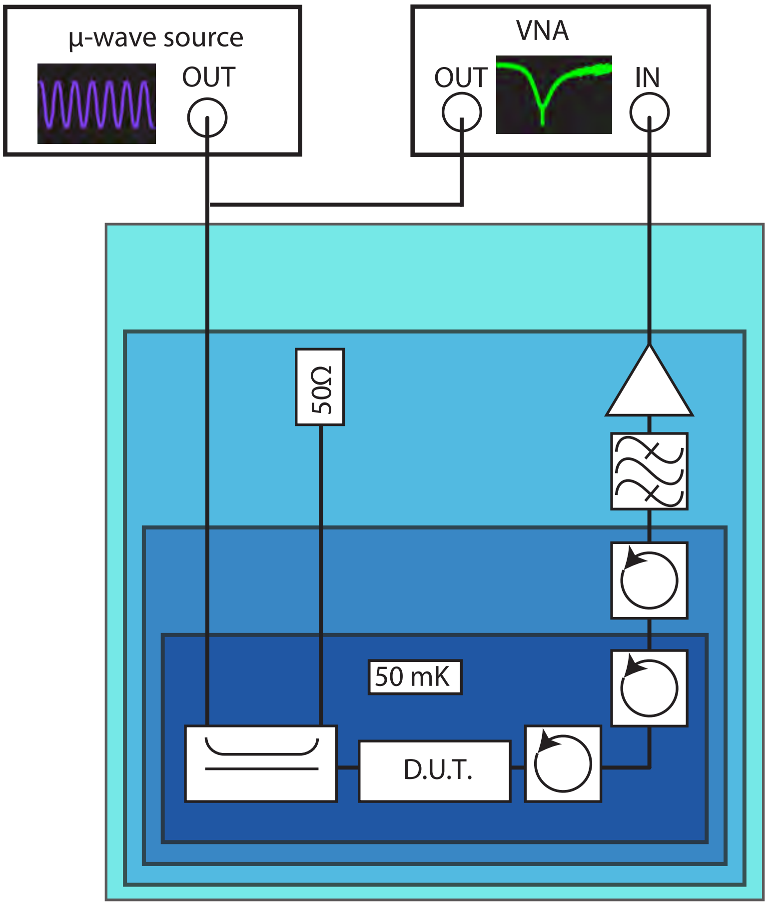

Figure 4.8: Schematic picture of the measurement setup for single tone measurements. The VNA output port is connected with the input line of the fridge and the output line of the fridge is connected to the input port of the VNA. The fridge schema shown here is simplified for exact internal fridge paths and setup please see Sec. (3.3.2).

large drive-tone intensities and only the bare resonator transmission characteristics for $P_\mathrm{d} \to 0$

By varying the detuning accordingly the anti-Stokes peak is tuned through the resonator dip. Figure (4.10,a)) shows the extracted maximum transmission and the effective mechanical linewidth for interference of the anti-Stokes field with the probe tone. The peak transmission is at its maximum for optimal detuning and decreases when moving away from optimal detuning. For detunings $\Delta - \omega_\mathrm{r} > \Gamma_\mathrm{m}/2$ the transmission of the EMIT peak vanishes. Also the linewidth increases towards optimal detuning and decreases towards the natural linewidth for large deviations ($|\Delta - \Omega_\mathrm{m}| > \Gamma_\mathrm{r}$) (see Fig. (4.10,b))).

In the next measurement the drive power is varied for a fixed detuning at the optimal

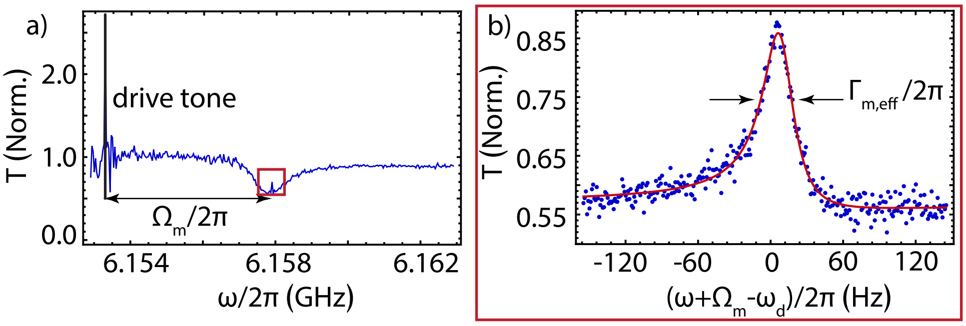

Figure 4.9: Example measurement data for the EMIT configuration. a) Full EMIT spectrum with red-detuned drive tone ($0.1\,\mu$W) and resonator dip with transmission window (probe power 282 fW). b) Zoom in to the transmission window with indicated effective mechanical linewidth $\Gamma_{\mathrm{m,eff}}$.

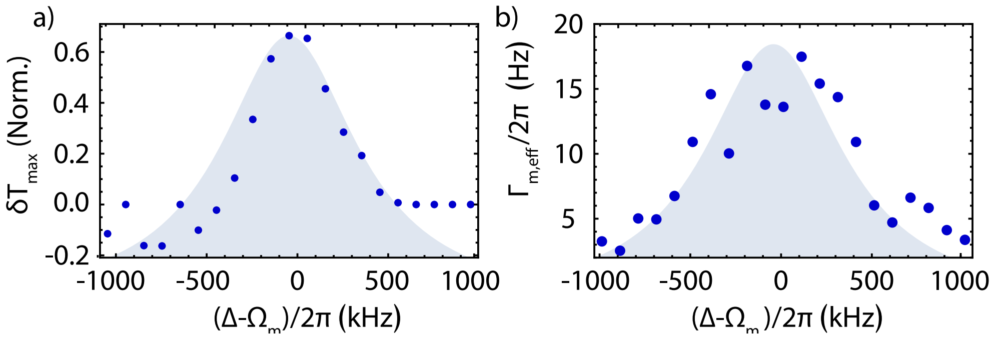

Figure 4.10: a) Measured microwave transmission at different positions within the μ-wave resonator range in presence of a strong red-detuned drive tone (28 nW), as a function of the drive detuning $\Delta = \omega - omegadrive$. The local peak maximum T_{max} is normalized to the value of the μ-wave resonator transmission at the respective point without a drive-tone being present T_{norm}: $\delta T_{\mathrm{max}} = T_{\mathrm{max}}/T_{\mathrm{norm}}$. The value increases towards $\Delta = \Omega_{\mathrm{m}}$. b) Effective linewidth $\Gamma_{\mathrm{m,eff}}$ of the transmission window for the same frequency sweep. Here the linewidth too increases towards optimal detuning. Shaded in grey is the spectral response of the μ-wave resonator response function.

red-detuned value of $\Delta = -\Omega_{\mathrm{m}}$ (Fig. (4.12)). For high drive powers the rate at which phonons are converted to photons is increased and the linewidth widens as shown in Fig. (4.11). Additionally the resulting peak inside the resonator dip gains in amplitude (Fig. (4.12)) :

$$\Gamma_{\mathrm{m,eff}} = \Gamma_{\mathrm{m}} + \frac{4g^2}{\kappa_{\mathrm{ges,r}}}. \tag{4.2}$$

Using $g = g_{\mathrm{m},0}\sqrt{\bar{n}_{\mathrm{r}}}$ the photon number inside the μ-wave resonator can be calculated. Together with the theoretical photon number inside the μ-wave resonator calculated from the drive tone power

$$\bar{n}_{\mathrm{r}}(P_{\mathrm{d}}) = \frac{P_{\mathrm{d}}}{\hbar\omega_{\mathrm{d}}} \frac{\kappa_{\mathrm{ext,r}}/2}{(\kappa_{\mathrm{ges,r}}/2)^2 + \Delta^2} \tag{4.3}$$

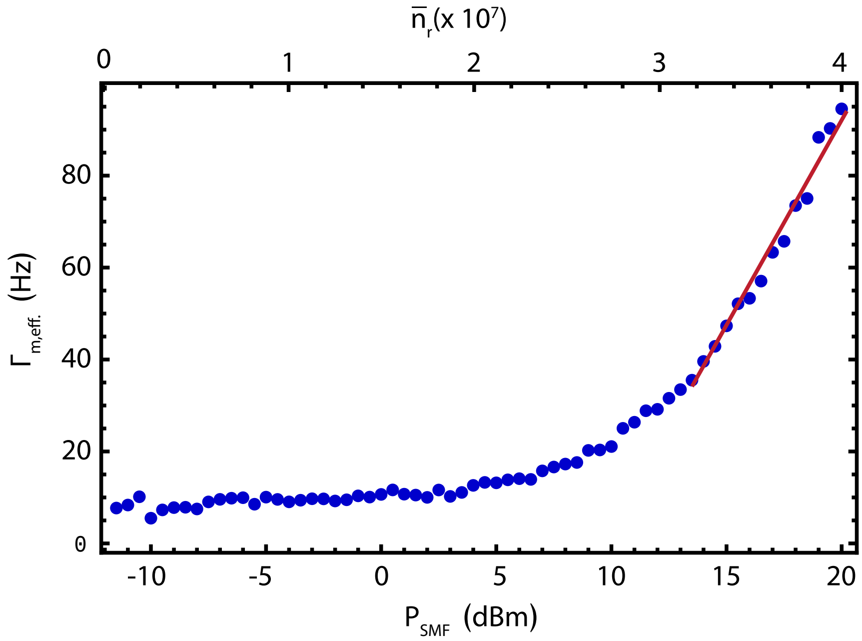

Figure 4.11: Effective linewidth of the mechanical resonance versus SMF drive power. From the linear part indicated ba the red line the attenuation in the system is calculated by using Eq. (4.2). At low drive powers the linewidth approaches the natural linewidth $g_{m,0}/2\pi \approx 8\,\mathrm{Hz}$.

the total attenuation of the input line in the system can be determined to $55.5 \pm 0.4\,\mathrm{dB}$. The power transmission at $\omega_p = \omega_d + \Omega_m = \omega_r$ in this case is

$$T = \left| \frac{1 - \kappa_{\mathrm{ext,r}}/\kappa_{\mathrm{ges,r}} + C}{1 + C} \right|^2 \tag{4.4}$$

with the cooperativity $C = 4g^2_{m,0}\bar{n}_r/\kappa_{\mathrm{ges,r}}\Gamma_m$ [65]. Figure (4.12) shows the measured data in combination with the theoretical curve from Eq. (4.4) demonstrating a maximal EMIT transmission of about 94%.

For EMIA measurements the drive tone was detuned to the blue sideband ($\Delta = +\Omega_m$). Here the inverse happens, the anti-Stokes is suppressed and the Stokes process is visible see Eq. (2.9). This implicates a decrease of the linewidth close to optimal detuning and an decrease in the amplitude of the μ-wave resonator transmission. The complementary drive frequency sweep compared to Fig. (4.10) (red sideband) is shown in Fig. (4.13) and thus the Stokes dip is tuned through the resonator transmission function. Fig. (4.13,a)) shows that the amplitude of the interference dip is minimal for optimal detuning and increases for deviations. Again, the EMIA signature vanishes, if its frequency leaves the vicinity of the μ-wave resonator eigenfrequency ω_r.

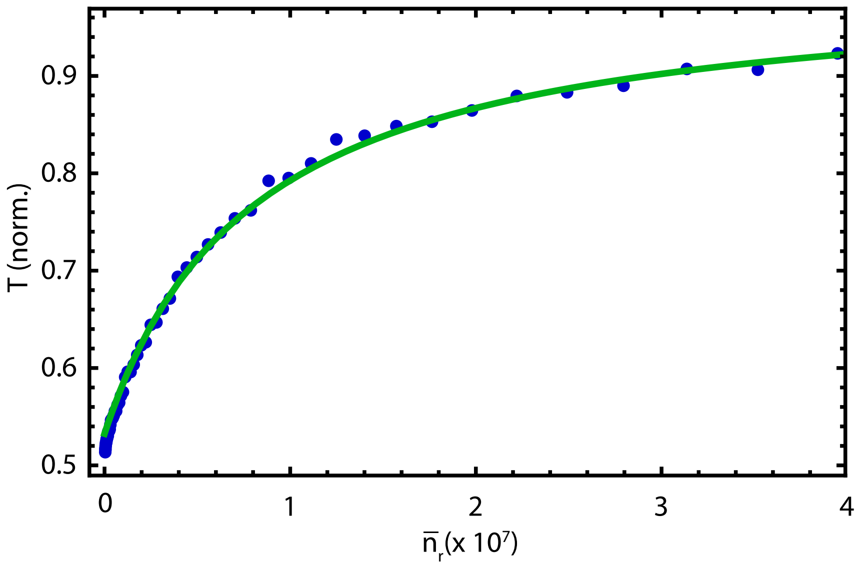

Figure 4.12: Microwave transmission in EMIT configuration as a function of the µ-wave resonator photon number. The photon number is calculated from the drive power using the determined attenuation (55.5 dB) and Eq. (4.3). The green line is a theory plot of Eq. (4.4) using the parameters $\kappa_{\mathrm{ges,r}}$,$\kappa_{\mathrm{ext,r}}$,$g_{\mathrm{m,0}}$ and Γ_{m} as determined independently above.

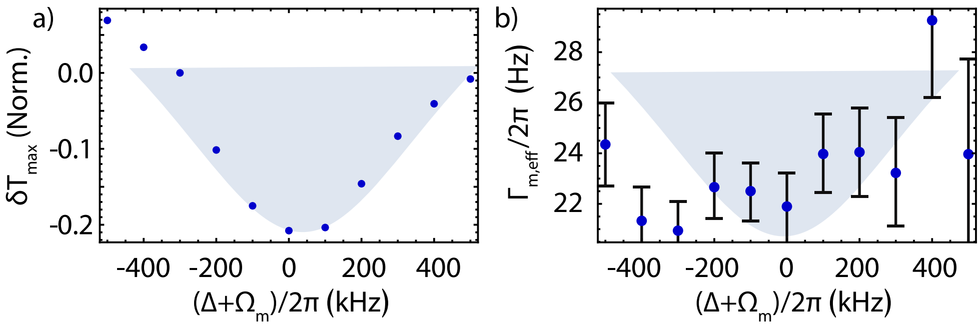

Figure 4.13: a) Measured microwave transmission at different positions within the µ-wave resonator range in presence of a strong blue-detuned drive tone (28 nW), as a function of the drive detuning $\Delta = \omega - omegadrive$. The local peak maximum T_{max} is normalized to the value of the µ-wave resonator transmission at the respective point without a drive-tone being present T_{norm}: $\delta T_{\mathrm{max}} = T_{\mathrm{max}}/T_{\mathrm{norm}}$. The value decreases towards $\Delta = \Omega_{\mathrm{m}}$. b) Effective linewidth $\Gamma_{\mathrm{m,eff}}$ of the transmission window for the same frequency sweep. Due to the large uncertainty in the data points the expected behaviour can not be observed. This uncertainty is due to large noise contributions in the measurements caused by the high drive tone amplitude. Theory predicts a decreasing linewidth towards optimal detuning (see Eq. 2.10)). Shaded in grey is the spectral response of the µ-wave resonator response function.

4.1.6 Summary & Conclusions

Summarizing the goal of coupling an aluminum nanobeam to a µ-wave resonator was achieved. The mechanical resonance frequency of $\Omega_{\mathrm{m}}/2\pi = 4.87\,\mathrm{MHz}$ and the linewidth of the μ-wave resonator of $\kappa_{\mathrm{ges,r}} = 927\,\mathrm{kHz}$ put the system in the resolved sideband regime and enable the effects of EMIT and EMIA which both have been observed and quantitatively discussed. Even more, this was accomplished with a beam layout that allows integration into a hybrid, nanobeam/transmon qubit sample, which is one of the main objectives of this thesis.

4.2 Sample layout #2 (μ-wave resonator & transmon qubit)

In this section, the measurements on a transmon qubit, coupled to a μ-wave resonator (sample # 2) will be discussed. The sample used for these measurements is described in Sec. (3.2.2). The goal of these measurements was to check if the fabrication process of the qubit, particularly the Josephson junctions, is compatible with the fabrication process of the nanobeam introduced in Sec. (3.1). Due to the fact that the releasing of the nanomechanical beam has to be the last fabrication step, it is important to confirm and ensure that the transmon qubit is not damaged by this step. The fabrication step resulting in the free suspension of the nanobeam contains electron beam lithography, isotropic reactive ion etching and a final critical point drying step. Single and two-tone measurements allow to extract relevant qubit parameters: the coupling g_q between the qubit and the μ-wave resonator, the anharmonicity, which for transmon qubit equals the charge energy $-E_C$ and the linewidth of the qubit Γ_q, which is directly related to the coherence time of the qubit T_2. To investigate the impact of these critical fabrication steps concerned with the releasing of the nanobeam on the transmon qubit the identical sample was measured three times. The first time after its initial fabrications (**A**)(Fig. 3.3,f)). The second time after a fabrication sequence containing coating the sample in resist and baking it at high temperatures (**B**)(Fig. 3.2,b)) and the third time after the fabrication sequence containing coating the sample with resist, baking the resist and the RIE etching process (**C**)(Fig. 3.1g)) The sample *nBSi2.4* was used for these measurements.

4.2.1 Single Tone spectroscopy

This section contains the single-tone microwave spectroscopy of the transmon qubit. Single-tone spectroscopy enables experimental access to the coupling constant g_q between the transmon qubit and the $\lambda/2$ μ-wave resonator it is coupled to. The used measurement setup and techniques are described and the extracted coupling g_q is presented for the three measurements described above.

Setup

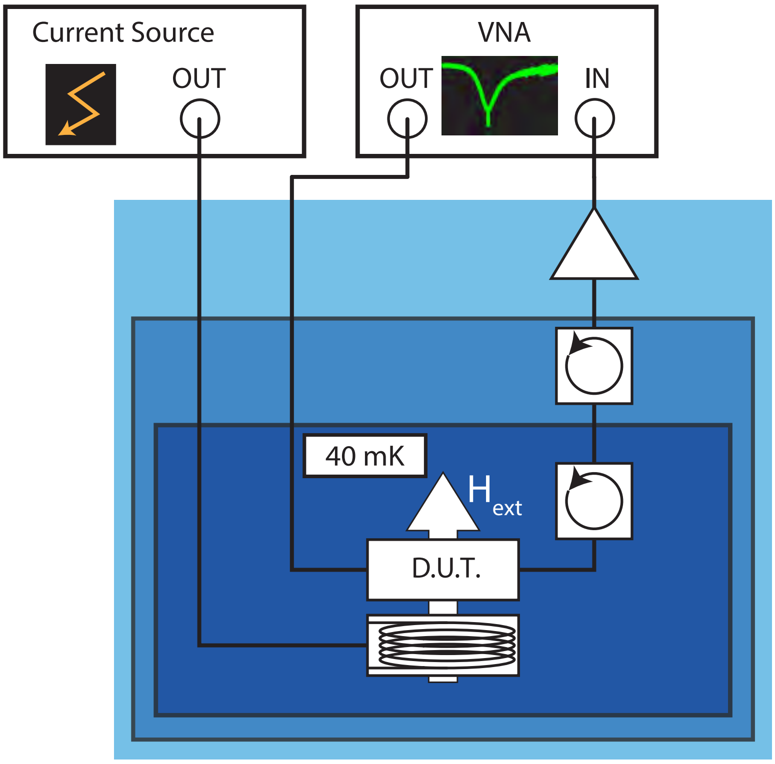

Figure 4.14: Schematic picture of the setup used for spectroscopy of the transmon. The sample is inside the fridge and connected to the in and output-port of a vector network analyzer. The magnetic flux through the sample is controlled by a current source connected to a coil next to the samplebox. This schema shows a simplified picture of the fridge. For further information please see Fig. (3.9)

For all measurements on the transmon qubit fridge # 1 (Fig. (3.9)) is used. The sample is mounted on the mixing chamber stage of the cryostat and operated at about 40 mK. The sample is connected to the output port of a *Rhode& Schwarz ZVB8* VNA by the attenuated microwave input line of the fridge described in Sec. (3.3.3). On the exit port the sample is connected to the input port of the same VNA by the microwave output line. The coil next to the sample box was connected to a *YOKOGAWA GS200* current source by a dc-line. This allows to create a variable external magnetic field perpendicular to the squid loop of the transmon qubit and hereby tune its resonance frequency.

Measurements

The coupling g_{q} between the transmon and the µ-wave resonator is one of the important system parameters, because it determines the rate at which the two can exchange excitations. To access g_{q}, the transmission through the µ-wave resonator is measured continuously, while varying the magnetic flux (Φ) applied to the sample. The externally applied flux Φ tunes the resonance frequency of the transmon qubit between 0 and its maximum value $\omega_{\mathrm{q,max}}$ according to Eq. (2.24). When sweeping Φ over several flux quanta Φ_0 the qubit frequency ω_{q} will therefore periodically match the resonance frequency of the µ-wave resonator. In the transmission spectra of the resonator this manifests as avoided crossings as shown in Fig. (4.15) (see Sec. (2.5.1)). In this graph the evolution of the resonator frequency depends on the transmon frequency. Three different domains can be distinguished: The transmon frequency is close to zero ($\omega_{\mathrm{q}} \rightarrow 0$) at $\Phi = 0.5\,\Phi_0$, here the nearly undisturbed µ-wave resonator can be observed also the coupling g_{q} has a negligible small impact on the µ-wave resonator at this point. By increasing the magnetic flux, the transmon frequency increases and becomes resonant with the resonator frequency around $\Phi = 0.76\,\Phi_0$ where an avoided crossing is observed. This is due to the mixing of qubit and resonator states which happens because both subsystems exchange excitations as detailed in Sec. (2.5.2). The transmon frequency keeps increasing with increasing magnetic flux until $\Phi = \Phi_0$, where it reaches its maximum. Further increasing the magnetic flux causes the transmon frequency to decrease again and match the resonator frequency at $\Phi = 1.24\,\Phi_0$, where the next avoided crossing appears. These avoided crossings indicate the range where transmon qubit and µ-resonator are close enough to exchange excitations. The resulting mixed states visible are split by $\sqrt{n}\frac{2g}{2\pi}$ (Sec. (2.5.2)) with n being the number of photons exchanged in one excitation swap, this is $n = 1$ for the used probe powers.
A measurement of the avoided crossing around $\Phi = 1.24\,\Phi_0$ with higher resolution is shown in Fig. (4.16). Here the avoided crossing is clearly visible as two separated resonance lines and the range where both resonances coexist is distinguishable. In the center of this avoided crossing, at $\Phi \approx 0.74\,\Phi_0$ both resonances have an equal amplitude indicating an equal superposition of states. A frequency sweep at this point is shown in Fig. (4.17) The distance between the two peaks equals $2g/2\pi$ and a coupling of $g_q^A/2\pi = 140\,\mathrm{MHz}$ was determined for measurement (**A**). In the other measurements the values $g_q^B/2\pi = 138\,\mathrm{MHz}$ (**B**) and $g_q^C/2\pi = 140\,\mathrm{MHz}$ (**C**) were obtained. All those values are in accord with the simulated value (App. (A.3)) of $g_q^{simu}/2\pi = 160\,\mathrm{MHz}$. Deviations between the two can mainly be explained by simplifications in the simulation, the design values for gaps and distances. In reality the shadow evaporation causes non rectangular shapes which are not taken into account in the simulation.

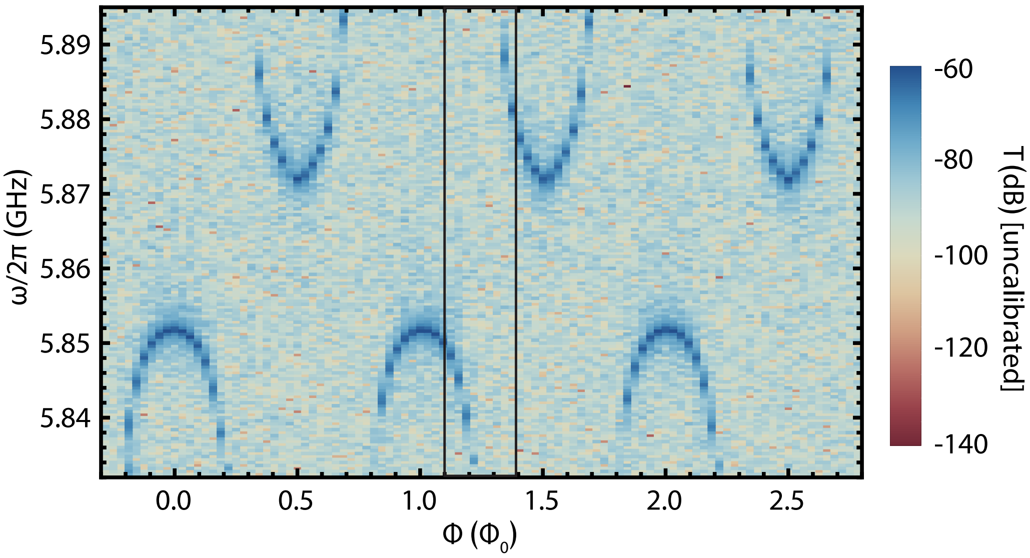

Figure 4.15: Transmission spectroscopy of the coupled μ-wave resonator - qubit system (Sample # 2) as a function of the applied magnetic flux Φ. Several avoided crossings can be observed. Here a VNA probe power of 1 nW was used. The two black lines mark a range to be further investigated in Fig. (4.16). Further explanations are given in the text.

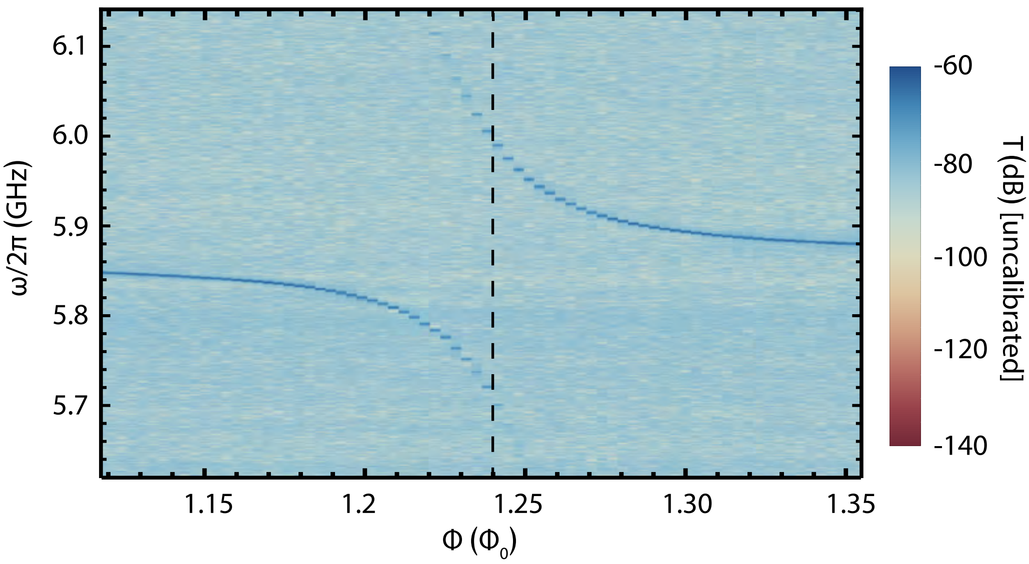

Figure 4.16: Avoided crossing between μ-wave resonator and qubit around $\Phi \approx 1.24\Phi_0$. Two resonance peaks, corresponding to the mixed states can be seen clearly and also the range were they both coexist is visible. Here a VNA Probe power of 0.19 nW was used, this corresponds to $\approx$ 4500 photons (see Eq. (4.3)). The black dashed line marks a single frequency sweep further investigated in Fig. (4.17).

4.2.2 Two Tone spectroscopy

While single-tone spectroscopy allowed to extract the coupling (g_q), two-tone spectroscopy is used to determine the other relevant qubit parameters $\omega_{q,max}$ (the maximal qubit

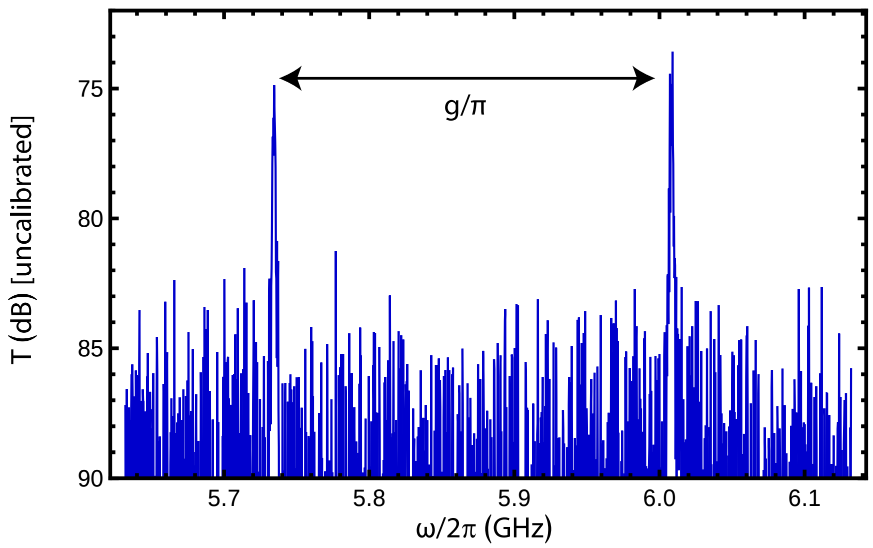

Figure 4.17: Transmission spectrum of sample # 2 at a fixed magnetic flux $\Phi \approx 1.24\,\Phi_0$. Here both resonances can be seen in coexistence and their equal amplitude indicates an equal superposition of qubit and resonator states. The separation of the two resonances equals g_q/π.

frequency), E_C (the anharmonicity of the qubit) and Γ_q (the qubits linewidth).

Setup

To perform the two-tone measurements the setup shown in Sec. (4.2.1) is expanded by a μ-wave source (*Rhode&Schwarz SMF 100A*) (SMF) as sketched in Fig. (4.18). The output paths from VNA and SMF are combined with a power combiner before sending the sum signal into the fridge by the microwave input line and to the sample mounted on the mixing chamber stage. The microwave output line is still connected to the input port of the VNA and the coil at the sample-box is still connected to the current source by a dc-line. The internal attenuation of the fridge was not changed, however external attenuators between the measurement devices (VNA and SMF) and the power combiner as well as attenuators between the power combiner and the microwave input port of the fridge were used, this attenuation will be taken into account when probe (VNA) or drive (SMF) powers are given.

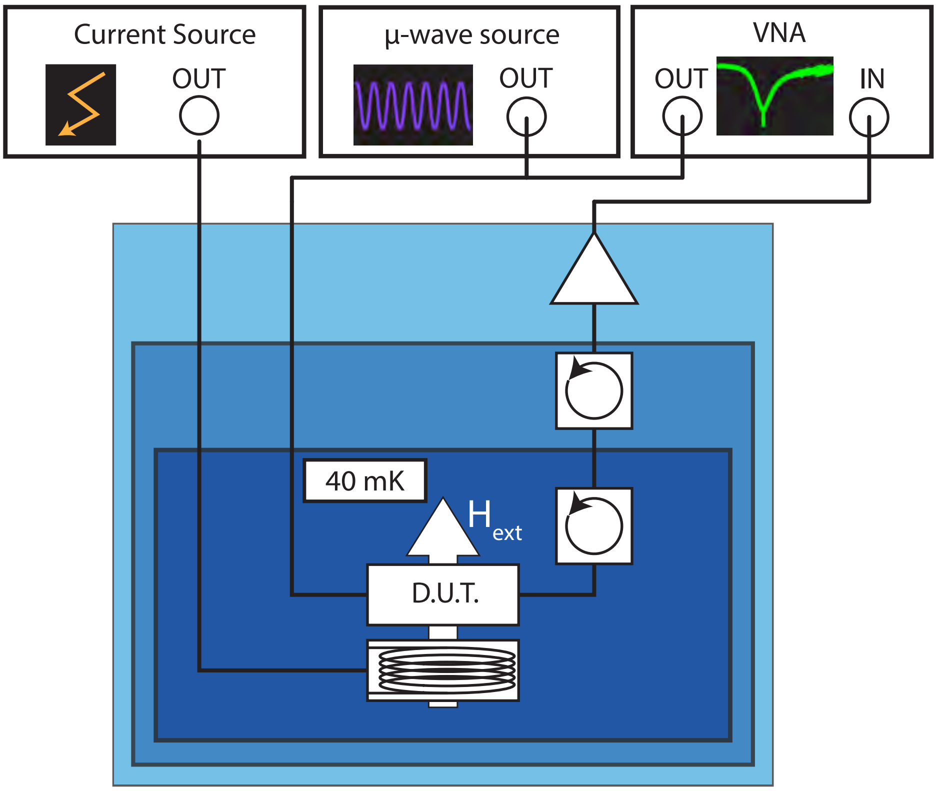

Figure 4.18: Schematic picture of the setup used for two-tone spectroscopy of the transmon. The sample is inside the fridge and connected to the output ports of the vector network analyzer and the μ-wave source. The microwave output line is connected to the vector network analyzer. The magnetic flux trough the sample is controlled by a current source connected to a coil next to the sample-box. This schema shows a simplified picture of the fridge a complete schematic of the microwave circuitry inside the cryostat is given in Fig. (3.9).

Measurements

In the dispersive regime the transmon frequency has a linear dependency on the resonator population and vice versa. In particular, when the transmon changes its excitation, as example from the ground state $|g\rangle$ to the first excited stage $|e\rangle$, the resonator frequency will shift. This is known as AC-Stark shift. This behaviour is used to determine the maximum qubit frequency (at $\Phi = 0.5\,\Phi_0\,, 1.5\,\Phi_0, etc.$) via spectroscopy of the μ-wave resonator. To this end the resonator is probed at its resonance frequency ω_r with the VNA while the qubit is in its ground state ($|g\rangle$). With an additional drive tone ω_d (generated by the SMF) the qubit is excited. As the qubit frequency is initially unknown, the frequency of the drive tone is varied while monitoring the μ-wave resonator transmission. If the drive tone frequency (ω_d) matches the qubit transition frequency, the qubit is excited and the resonator frequency shifts. For a fixed probe frequency $\omega_\mathrm{p} = const.$, which is initially tuned to the bare resonator frequency ω_r, this resonator frequency shift manifests as change in the transmitted phanse and change in the microwave transmisison. Figure (4.19) shows the µ-wave resonator transmission for a fixed frequency of $\omega_\mathrm{p} = \omega_\mathrm{r} \approx 5.9\,\mathrm{GHz}$ and a drive power $P_\mathrm{d} = 1\,\mathrm{fW}$ and an applied flux of $\Phi = 1\,\Phi_0$. When varying ω_d a reduction in the transmission of ω_p is found for a drive tone frequency of 7.14 GHz corresponding to the maximal transmon transition frequency of $\omega_\mathrm{q}/2\pi = 7.14\,\mathrm{GHz}$. The linewidth of the qubit depends on the population of both the µ-wave resonator and drive power used to excite the qubit. Therefore, to obtain the natural qubit linewidth, both the probe and the drive power have to be decreased as far as possible [35]. This was done for Fig. (4.19) were the probe power was 0.5 fW and the drive power 1 fW. Each data point is composed of 200 averages due to the low signal to noise ratio. The qubit linewidth was extracted as $\frac{\Gamma_\mathrm{q}}{2\pi} = 648\,\mathrm{kHz}$ in measurement (**A**) . This translates into $T_1 = \frac{2}{\Gamma_\mathrm{q}} = 491\,\mathrm{ns}$, which is comparable with other transmon qubits build at the WMI up to date [35] [66] and it is also comparable to initial transmon experiments [67] [68]. For the measurements (**B**) and (**C**) the linewidth could not be extracted due to fluctuations in the fridge temperature which influence the µ-wave resonators resonance frequency $\omega_\mathrm{r}(T)$. The averaging necessary for linewidth measurements was not possible any more and thus Γ_q could not be extracted.

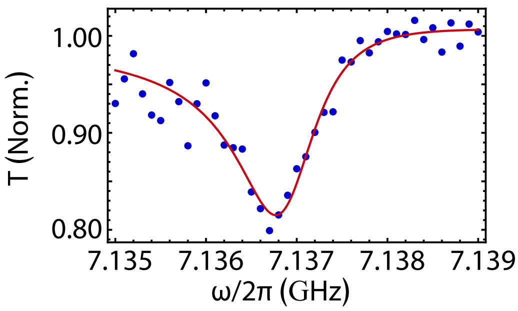

Figure 4.19: This Graph shows a measurement for the process step configuration (**A**) of the qubit in the dispersive regime. To extract the natural qubit linewidth, both the drive ($-50\,\mathrm{dBm}$) and the probe($-53\,\mathrm{dBm}$) power are decreased as far as possible. A Lorentzian fit (red) is used to extract the linewidth $\frac{\Gamma_\mathrm{q}}{2\pi} = 648\,\mathrm{kHz}$. Every data point is composed of 200 averages and measured with a bandwidth of 10 Hz. The date is normalized to the transmission with the drive tone far detuned from the qubit frequency. The external applied magnetic flux was set to $\Phi = 1\,\Phi_0$.

The qubit anharmonicity is an additional important parameter. For the transmon it equals the negative charge energy $-E_\mathrm{C}$ (Sec. (2.4.3)). It is easily calculated from the design and a comparison between measured and simulated value can give information on the quality of the simulation (App. (A.3)). From a physical point of view the anharmonicity limits the minimal pulse-length the qubit can react to. This is explained by the uncertainty equation $\Delta E \Delta t \geq \frac{\hbar}{2}$. This implies that a narrow wave packet (equivalent to a short pulse) has a broad frequency/energy spectrum. Therefore the pulse length is limited by the E_C, $\tau \geq \left(\frac{\hbar}{2E_\mathrm{C}}\right)$, as a shorter pulse could excite more than one qubit level and thus the assumption of a two level system would no longer be valid.

To measure the anharmonicity the frequency difference between the excitation frequencies for the first excited state ω_{ge} and the second excited state ω_{gf} has to be determined (Sec. (2.5.1)). Due to parity reasons [69] it is not possible to excite the second excited qubit state $|f\rangle$ with a single photon from the ground-state $|g\rangle$ directly. Instead, a two-photon excitation process with half the transition frequency $\frac{1}{2}\omega_{\mathrm{gf}}$ as shown in Fig. (4.20,c)) is possible. Experimentally, this is achieved by increasing the drive power. This is possible because the transition matrix elements for the one and two-photon processes scale differently with excitation amplitude (linear for single photon and quadratic for two-photon processes). At first (drive power $-20\,\mathrm{dBm}$ probe power $-47\,\mathrm{dBm}$) the one photon process for exciting the $|e\rangle$-state is clearly visible: In Fig. (4.20,a)), the $|f\rangle$ state excitation is present, but just slightly. If the drive power is increased (drive power $-15\,\mathrm{dBm}$, probe power $-53\,\mathrm{dBm}$) the $|f\rangle$-state becomes excited, see Fig. (4.20,b)). From these measurements the anharmonicity is extracted. In the data shown in Fig. (4.20) this is $E_{\mathrm{C}}/h = 290\,\mathrm{MHz}$ for measurement (**B**). In measurement (**A**) the value was $E_{\mathrm{C}}/h = 204\,\mathrm{MHz}$, in measurement (**C**) the value could not be determined due to massive instabilities in the fridge temperature (involuntary warm up). All of the measured values are in accord with the simulated value $E_{\mathrm{C}}/h = 225\,\mathrm{MHz}$ (App. (A.3)). The deviations between measured and simulated values can be accounted to simplifications in the simulation, e.g. the interleaved aluminum-oxide layer is not considered. With the maximal transition frequency of $\frac{\omega_{\mathrm{q}}}{2\pi} = 7.14\,\mathrm{GHz}$ this allows to calculate $E_{\mathrm{J0}}/h = 21.9\,\mathrm{GHz}$ and a ratio $\frac{E_{\mathrm{J0}}}{E_{\mathrm{C}}} = 75$ with the E_{C} value gained in measurement (**B**).

4.2.3 Comparison of measured transmon parameters

As mentioned before this sample was measured three times with intermediate fabrication procedures. Therefore here a compilation of the measured data for each step is given:

Property	measurement (**A**)	measurement (**B**)	measurement (**C**)
$g_{\mathrm{q}}/2\pi$	140 MHz	138 MHz	140 MHz
E_{C}/h	204 MHz	290 MHz	—
$\Gamma_{\mathrm{q}}/2\pi$	648 kHz	—	—
$\omega_{\mathrm{q}}/2\pi$	7.14 GHz	6.84 GHz	6.43 GHz

This shows clearly that the transmon qubit is still functional after performing the fabrication steps necessary for releasing the nanobeam. Measurement (**B**) shows that the transmon survives the coating process with positive resist and the bake at 170°C. Measurement (**C**) shows that the transmon qubit survives this coating process twice and the RIE process used for releasing the nanobeam does not destroy the Josephson junctions.
Due to temperature instabilities during the measurement runs for the configurations (**B**) and (**C**) some parameters could not be determined during those cooldowns. The main reason is that the eigenfrequency of the μ-wave resonator sensitively reacts on the

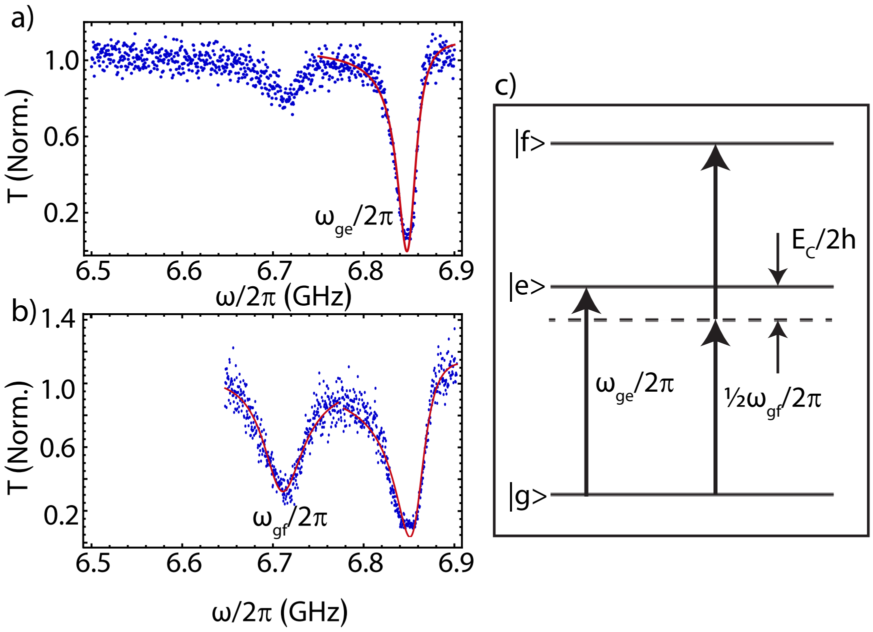

Figure 4.20: Measurement (**B**) of the qubit anharmonicity E_C via two-tone spectroscopy. a) Measurement in the dispersive regime using the AC-Stark shift, due to low drive power (-25 dBm) the $|f\rangle$-state is very weak, the $|g\rangle$-state however is clearly visible. b) By increasing the drive power (-15 dBm) also the $|f\rangle$ gets excited. c) Schematic picture of the three relevant transmon states $|g\rangle$, $|e\rangle$ and $|f\rangle$ and their respective transition frequencies. The anharmonicity in form of $\alpha = \frac{-E_\mathrm{C}}{2h}$ is also noted. The data was measured with a bandwidth of 100 Hz. Each data point consists of 10 averages.

temperature fluctuations rendering an AC-Stark shift based measurement impossible.
In the data presented a discrepancy not accountable to measurement uncertainties shows up in the E_C values. This discrepancy between the measured values of E_C for measurements (**A**) and (**B**) physically can be explained by a change in the capacitance C of the transmon qubit. Calculations show that the presence of a dielectric between the capacitor fingers during the measurement (**A**) could lead to the observed difference. More precisely a resist layer of about 25 nm would have this effect. This could be a possibility due to the small gaps between the inter-digital structures which are between $1-2\,\mu$m. Records of the fabrication process show that the lift off and cleaning process used at this stage differs from the ones used before measurements (**B**) and (**C**) where notably longer and deliberate cleansing processes were used. Apart from the charging energy $E_\mathrm{C} = \frac{e^2}{2C}$, also the qubit-resonator coupling and the maximal qubit frequency depend on C. This dependence, however is much weaker ($g_\mathrm{q} = \frac{2eV_\mathrm{rms}}{\sqrt{2}\hbar}\beta\left(\frac{E_\mathrm{J}}{8E_\mathrm{C}}\right)^{\frac{1}{4}}$, $\omega_\mathrm{q} = \frac{1}{\hbar}\sqrt{8E_\mathrm{J0}E_\mathrm{C}}$), so that no effect of the residual resist is expected in the measurements of g_q and ω_q.

4.2.4 Summary & Conclusions

In summary the goal of structuring a transmon qubit and coupling it to a μ-wave resonator was achieved. The ratio of $\frac{E_{J0}}{E_C} = 75$ confirms the qubit is well within the transmon regime. Measured parameters like coupling and anharmonicity are in good agreement with simulated values. Altogether, this enables parameter control for future samples already in the design-stage (App. (A.3)). The different measurements ((**A**),(**B**) and (**C**)) coupled with respective fabrication sequences show that the transmon qubit does not only survive these processes but also its basic parameters (E_C ,g_q and ω_q) do not change significantly. This evens the ground for hybrid samples where the transmon qubit is combined with a nanomechanical beam on one chip.

Chapter 5

Summary and Outlook

The main goal of this thesis was to check the feasibility of fabricating a hybrid three-body system consisting of a superconducting μ-wave resonator, a superconducting transmon qubit and a mechanical nanobeam resonator. To achieve this, first, the individual systems were fabricated and characterized. In a second step the fabrication procedures necessary for the individual systems were combined in a compatible way by optimizing each of them. Finally, a device with a transmon qubit and a mechanical nanobeam resonator coupled to a single μ-wave resonator on one and only one chip was fabricated and tested on its functionality.

Within this thesis the fabrication of mechanical nanobeam resonators was altered to be compatible with the one for transmon qubits. The main part here was to increase the yield of nanobeam samples and to optimize the reactive ion etching process, used to release the nanobeam from the silicon substrate. Also this goal was achieved. The optimized etching process was confirmed to be compatible with the transmon qubit by trying it on a functional transmon qubit sample and verifying the functionality afterwards.

The mechanical nanobeam resonator was first characterized at room temperatures using optical interferometry. For millikelvin measurements of the nanobeam, microwave spectroscopy was employed. This enabled extraction of important parameters like the mechanical resonance frequency, the linewidth and the electromechanical vacuum coupling. By using two-tone microwave spectroscopy, electromechanically induced transparency (EMIT) and electromechanically induced absorption (EMIA) could be observed and shown to match the theoretical predictions quantitatively. A characterization of the employed μ-wave resonator was made.

Single and two-tone spectroscopy of the transmon qubit allowed to determine the relevant parameters such as the maximal qubit frequency, the qubit linewidth and the qubit anharmonicity. The experimentally observed values are corroborated by numerical simulations, which allow to design qubits according to experimental demands in future experiments.

In conclusion, the feasibility of a hybrid three-body system consisting of a superconducting μ-wave resonator, a superconducting transmon qubit and a mechanical nanobeam resonator could be confirmed and the necessary fabrication techniques propelled to a point where success is plausible and achievable.

The next steps is to measure and understand the mechanical beam coupled to a $\lambda/2$ microwave resonator on the existing samples. When successful, the transfer of qubit excitations to the mechanical resonator using the μ-wave resonator as a microwave bus system has to follow. This however is expected to be ineffective due to the intrinsically small electromechanical vacuum coupling between mechanical and microwave resonator. For future endeavors, the main focus therefore lays on integrating the mechanical nanobeam resonator into the shunt capacitance of the transmon qubit. With this the electromechanical vacuum coupling should be enhanced and the way paved for experiments on three body interactions in the quantum regime [27]. This device layout is predicted to enable cooling of the mechanical resonator to its ground state and the exchange of excitations between all three systems on a single excitation. The interactions of a nonlinear two level system (transmon qubit) coupled to two harmonic oscillators (μ-wave and mechanical resonator) in the strong coupling regime will then be within experimentally accessible. This includes the possibility of observing a "phonon-Stark shift" where the qubit transistion frequencies depend on the number of mechanical oscillations [28]. This should be measurable by determining the e.g. $|e\rangle - |f\rangle$ transition frequency with and without sideband cooling of the mechanical resonator or even at different fridge temperatures. Similar to this also dressed electromechanical states consisting of qubit states and mechanical Fock states [31] should be present and observable in the system.

All this leads to the possibility of controlling the hybrid qubit mechanical resonator system and storing qubit information in the mechanical resonator. This enhances the coherence time of the hybrid qubit mechanical resonator system which would be a huge step towards better control in quantum information processing.

Appendix A

Fabrication sequences and Simulations

A.1 Fabrication sequences

A.1.1 Sample layout #1

1. **Cleaning the silicon chip**
   Cleaning the silicon chip with acetone(70℃) and ultrasonicate for 20 s rinse with acetone and isopropyl alcohol (IPA), dry with N_2.

2. **Coating with negative photo-resist**
   Coating the sample with ma-N 2403. Use spin-coater with program MP 2000RPM and one drop from a disposable pipette. Bake at 90℃ for 1 min .

3. **Write resonator and nanomechanical beam**
   Assemble into nB5 and run Jobfile: 01_6Beam2noBeam_layout03 with appropriate layer selection (no etching windows and frame layers). Exposure dose: $2.2\,\frac{\mathrm{C}}{\mathrm{m}^2}$.

4. **Developing the photo resist**
   Develop resist with ma-D 525 for 45 s rinse with water two times and dry with N_2.

5. **Evaporation of aluminum film**
   Assemble into „nanomechanics" sample holder and into Alu-EVAP and evaporate 100 nm aluminum perpendicular to sample surface.

6. **Lift–off process**
   Lift off the surplus aluminum by soaking the sample in acetone(70℃) for 15 min while creating liquid flow above sample surface with a pipette regularly. When the structure is visible transfer the sample from the lift–off beaker to a new acetone filled one under a continuous acetone jet. Then rinse in acetone and IPA and dry with N_2.

7. **Annealing**
   Anneal the sample in the annealing furnace at 300℃ for 30 min using the program: 28:AlAnnealPernpeinter

8. **Coating with positive photo-resist**
Coating the sample with Ar 617.08 (PMMA MA33%). Use the spin-coater with program MP 2000RPM and two drops from a disposable pipette. Bake at 170℃ for 2 min.

9. **Write etching windows**
Assemble into nB5 and run Jobfile: 01_6Beam2noBeam_layout03 with appropriate layer selection (etching windows).Exposure dose: $6\,\frac{\mathrm{C}}{\mathrm{m}^2}$

10. **Developing the photo-resist**
Develop the resist with Ar 600-56 for 2 min rinse with IPA two times and dry with N_2.

11. **RIE etching**
Assemble into *Oxford Instruments Plasmalab 80 Plus* and run the program: Beametchingdaniel :

12. **Remove the photo-resist**
Remove the resist used as etching mask by soaking the sample in acetone(70℃) for 15 min while creating liquid flow above sample surface with a pipette regularly. Then transfer the sample from the lift–off beaker to a new acetone filled one under a continuous acetone jet. Rinse with acetone and IPA. Assemble the sample into the CPD-sample holder under ethanol. Store sample in sample-holder in ethanol.

13. **CPD process**
Transfer the sample inside the sample-holder into the CPD process chamber without drying. Run the CPD process Sec. A.2.2.

A.1.2 Sample layout #2

1. **Cleaning the silicon chip**
Cleaning the silicon chip with acetone(70℃) and ultrasonicate for 20 s rinse with acetone and isopropyl alcohol (IPA), dry with N_2.

2. **Coating with negative photo-resist**
Coating the sample with ma-N 2403. Use spin-coater with program MP 2000RPM and one drop from a disposable pipette. Bake at 90℃ for 1 min .

3. **Write resonator and nanomechanical beam**
Assemble into nB5 and run Jobfile: 04_2Transmon_2Beam_6GHz with appropriate layer selection (no transmon layers). Exposure dose: $2.2\,\frac{\mathrm{C}}{\mathrm{m}^2}$.

4. **Lift–off process**
Lift off the surplus aluminum by soaking the sample in acetone(70℃) for 15 min

while creating liquid flow above sample surface with a pipette regularly. When the structure is visible transfer the sample from the lift–off beaker to a new acetone filled one under a continuous acetone jet. Then rinse in acetone and IPA and dry with N_2.

5. **Coating with double resist**
   Coating the sample with Ar 617.08(PMMA MA33%). Use the spin coater with program PMMA2000RPM and two drops from a disposable pipette. Bake at 160 ℃ for 10 min. Coating the sample with Ar 679.02(950k). Use the spin coater with program PMMA2000RPM and two drops from a disposable pipette. Bake at 160℃ for 10min.

6. **Write transmon qubit** Assemble into nB5 and run Jobfile: 04_2Transmon_2Beam_6GHz with appropriate layer selection (transmon layers). Exposure dose: $8\,\frac{\mathrm{C}}{\mathrm{m}^2}$.

7. **Developing the photo-resist**
   Develop the resist with Ar 600-56(4℃) for 3 min rinse with water and dry with N_2.

8. **Shadow-Evaporation**
   Assemble into „nanomechanics" sample holder and into Alu-EVAP. Evaporate 70 nm aluminum at an angle of $-17°$. Oxidize for 6000 s with set flow-rate of 8 and the valve at 15%. Evaporate 50 nm aluminum at an angle of $+17°$.

9. **Lift–off process**
   Lift off the surplus aluminum by soaking the sample in acetone(70℃) for 15 min while creating liquid flow above sample surface with a pipette regularly. When the structure is visible transfer the sample from the lift–off beaker to a new acetone filled one under a continuous acetone jet. Then rinse in acetone and IPA and dry with N_2.

A.1.3 Sample layout #3

1. **Cleaning the silicon chip**
   Cleaning the silicon chip with acetone(70℃) and ultrasonicate for 20 s rinse with acetone and isopropyl alcohol (IPA), dry with N_2.

2. **Coating with negative photo-resist**
   Coating the sample with ma-N 2403. Use spin-coater with program MP 2000RPM and one drop from a disposable pipette. Bake at 90℃ for 1 min .

3. **Write resonator and nanomechanical beam**
   Assemble into nB5 and run Jobfile: 01_6Beam2noBeam_layout03 with appropriate layer selection (no etching windows and frame layers). Exposure dose: $2.2\,\frac{\mathrm{C}}{\mathrm{m}^2}$.

4. **Developing the photo resist**
   Develop resist with ma-D 525 for 45 s rinse with water two times and dry with N_2.

5. **Evaporation of aluminum film**
   Assemble into „nanomechanics" sample holder and into Alu-EVAP and evaporate 100 nm aluminum perpendicular to sample surface.

6. **Lift–off process**
   Lift off the surplus aluminum by soaking the sample in acetone(70℃) for 15 min while creating liquid flow above sample surface with a pipette regularly. When the structure is visible transfer the sample from the lift–off beaker to a new acetone filled one under a continuous acetone jet. Then rinse in acetone and IPA and dry with N_2.

7. **Annealing**
   Anneal the sample in the annealing furnace at 300℃ for 30 min using the program: 28:AlAnnealPernpeinter.

8. **Coating with double resist**
   Coating the sample with Ar 617.08(PMMA MA33%). Use the spin coater with program PMMA2000RPM and two drops from a disposable pipette. Bake at 160℃ for 10 min. Coating the sample with Ar 679.02(950k). Use the spin coater with program PMMA2000RPM and two drops from a disposable pipette. Bake at 160℃ for 10min.

9. **Write transmon qubit** Assemble into nB5 and run Jobfile: 04_2Transmon_2Beam_6GHz with appropriate layer selection (transmon layers). Exposure dose: $8\,\frac{\mathrm{C}}{\mathrm{m}^2}$.

10. **Developing the photo-resist**
    Develop the resist with Ar 600-56(4℃) for 3 min rinse with water and dry with N_2.

11. **Shadow-Evaporation**
    Assemble into „nanomechanics" sample holder and into Alu-EVAP. Evaporate 70 nm aluminum at an angle of $-17°$. Oxidize for 6000 s with set flow-rate of 8 and the valve at 15%. Evaporate 50 nm aluminum at an angle of $+17°$.

12. **Lift–off process**
    Lift off the surplus aluminum by soaking the sample in acetone(70℃) for 15 min while creating liquid flow above sample surface with a pipette regularly. When the structure is visible transfer the sample from the lift–off beaker to a new acetone filled one under a continuous acetone jet. Then rinse in acetone and IPA and dry with N_2.

13. **Coating with positive photo-resist**
    Coating the sample with Ar 617.08 (PMMA MA33%). Use the spin-coater with program MP 2000RPM and two drops from a disposable pipette. Bake at 170°C for 2 min.

14. **Write etching windows**
    Assemble into nB5 and run Jobfile: 01_6Beam2noBeam_layout03 with appropriate layer selection (etching windows).Exposure dose: 6 $\frac{C}{m^2}$

15. **Developing the photo-resist**
    Develop the resist with Ar 600-56 for 2 min rinse with IPA two times and dry with N_2.

16. **RIE etching**
    Assemble into *Oxford Instruments Plasmalab 80 Plus* and run the program: beametchingdaniel:

17. **Remove the photo-resist**
    Remove the resist used as etching mask by soaking the sample in acetone(70°C) for 15 min while creating liquid flow above sample surface with a pipette regularly. Then transfer the sample from the lift–off beaker to a new acetone filled one under a continuous acetone jet. Rinse with acetone and IPA. Assemble the sample into the CPD-sample holder under ethanol. Store sample in sample-holder in ethanol.

18. **CPD process**
    Transfer the sample inside the sample-holder into the CPD process chamber without drying. Run the CPD process Sec. A.2.2.

A.2 Fabrication processes

A.2.1 Electron beam lithography (Example Jobfile)

Here an example for a jobfile used in the *NanoBeam Limited* nB5 Electron Beam Lithography System is given:

```
# run nbwrite DS/20150622_02_BeamsOnly_etching_nbAl1p6 -1=daniel:mbl -2=daniel:mbr

# .global

# marktype mp1

# registration (0,0)
```

```
# focus auto
focus 0.069
.end

.block
# marktype mp1
# registration (0,0)
focus 0.069
stepsize (0,0)
grid (1,1)
base_dose 6.0
pattern pureAlNanoelectromechanicswindows (-1 000 000, -1 000 000)
.end

.pattern
id pureAlNanoelectromechanicswindows
filename DS/2015-06-22/2015-06-22_02_BeamsOnly_etching_w.npf
dose 9 1
.end

.write
current 3.99
mf_trim (1.0005, 1.0005, 0, 0)
sf_trim (1.0005, 1.0005, 0, 0)
.end
```

A.2.2 Critical Point Drying Process

The CPD process consist of several main and several repeating steps. First the process chamber is cooled to 4°C. This is necessary for filling it with liquid CO_2 which is at room temperature. The sample is then transferred to the process chamber and the chamber filled with ethanol. Here special attention has to be paid on how to position the sample, if the sample–surface looks upward inside the process chamber a heavy contamination with metallic dust can be observed after the process. This does not occur if the sample is downward facing. After closing the process chamber the exchange process begins. Here the ethanol in the chamber is gradually replaced with liquid CO_2. To reassure the sample is never outside the liquid this is done by quick flushing interrupted by soaking phases of about 10 min. How often this process has to be repeated depends every time and is checked by examining the exhaust gas for ethanol residues. When no more ethanol is detected in the exhaust gas the CPD process can start. The chamber is sealed and the temperature increased above the critical temperature of CO_2 to ca. 40°C there it is stabilized. When all the CO_2 is in the supercritical fluid state the pressure inside the chamber is gradually lowered by venting. When the chamber pressure is equal to environment pressure the chamber can be opened and the sample extracted.

A.3 Transmon qubit simulations

In the course of fabricating transmon qubit samples. Simulations with *CST Studio Suite® 2015* were made. With the known transmon layout used in sample layout # 2 and # 3 simple electrostatic simulations of the shunt capacitance C_{S} and the gate capacitance $C_{\mathrm{g,q}}$ were made. With this the charge energy E_{C} and the coupling strength g_{q} can be estimated. For the transmon used in this thesis the simulations predicted a charge energy of $E_{\mathrm{C,simu}}/h = 225\,\mathrm{MHz}$ and a coupling of $g_{\mathrm{q}}/2\pi = 160\,\mathrm{MHz}$.
When these values were verified by measurements further simulations investigating the impact of different transmon layout measures on these parameters were made. For this a slightly changed layout shown in Fig. (A.1)was used. Here the SQUID loop was neglected and therefore is not present in the layout, this is appropriate for $C_{\mathrm{S}} \gg C_{\mathrm{JJ}}$, where C_{JJ} is the capacitance from the Josephson junctions. The results of these simulations are following:

- The shunt capacitance is mainly influenced by the overall length of the bulks ($\approx 2e + f$) and the gap i between them, but also the width of the capacitor plates d has to be considered, especially for small i.

- The gate capacitance is, as formulas suggest, mainly dependent on the shunt capacitance and the distance to the *upmu*-wave resonator (gap), however for large distances also the other gaps to the groundplane (gap2 and gap3) have to be considered. The

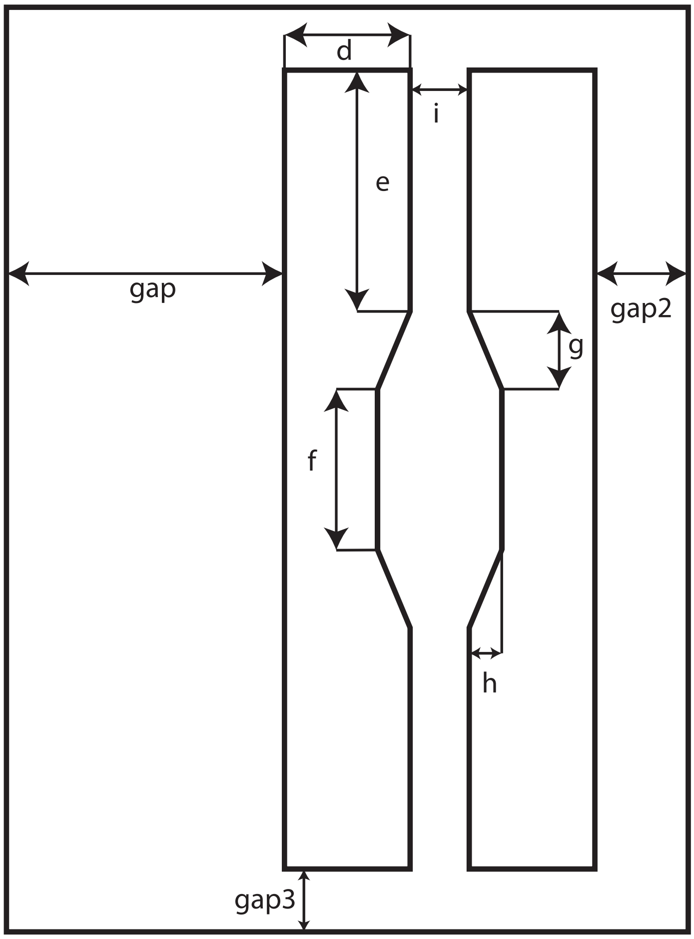

Figure A.1: Transmon qubit layout used for simulations investigating the impact of structural changes. Only the transmon inside its pocket is shown. The different distances are denoted.

gap to the groundplane opposite to the resonator (gap2) should be small to enable access with a microwave antenna at this position, this complicates the process of finding the right gap3.

- The distances e and f are interchangeable, the length of f is dictated only by the measures of the used SQUID loop, which is not considered in this simulation.

Appendix B

Measurement setups and circuitry

B.1 Detailed measurement setup for homodyne detection

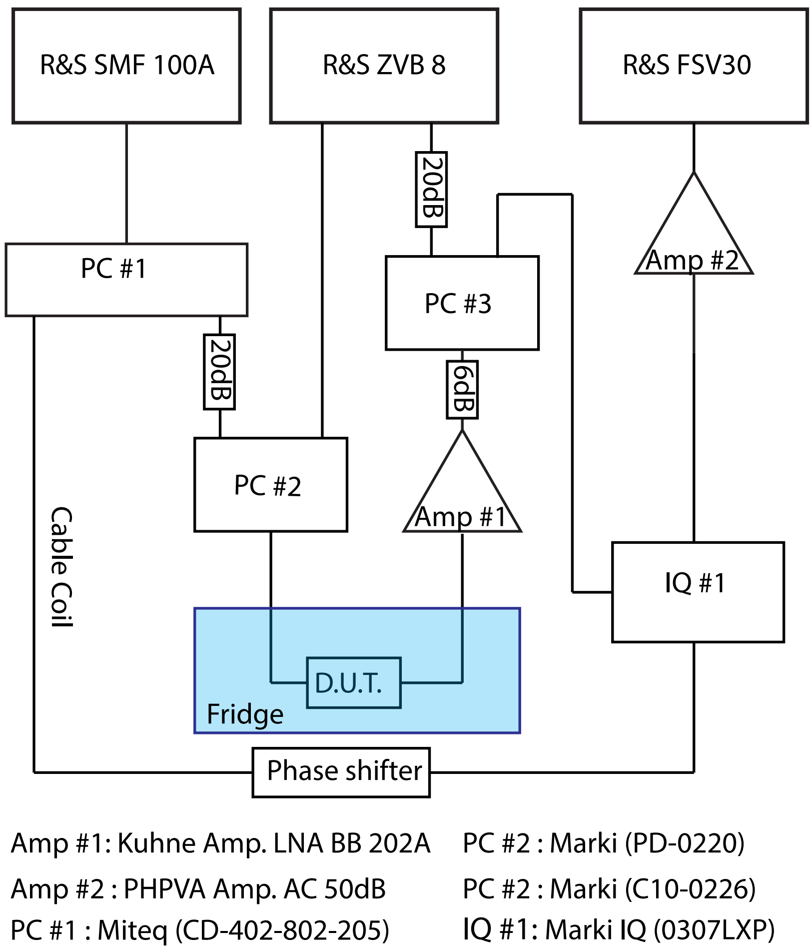

Figure B.1: Exact wiring and device layout for the homodyne measurement setup.

B.2 Additional measurement data

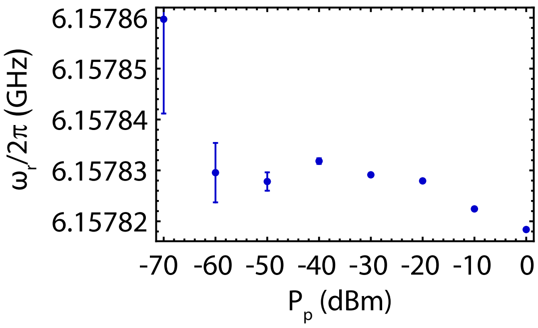

Figure B.2: Dependency of the μ-wave resonator resonance frequency on the probe power. The resonance frequency stays constant from −20 dBm to −60 dBm. The attenuation for this measurement was −78,5 dB for the whole input path.

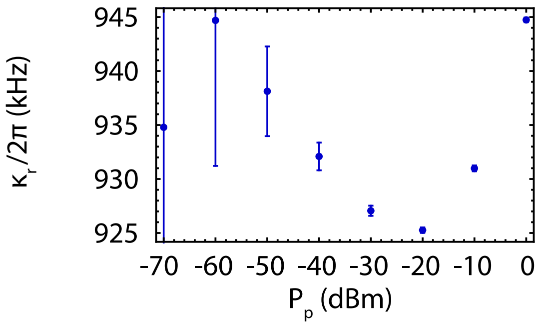

Figure B.3: Dependency of the μ-wave resonator linewidth on the probe power. The effective linewidth has a minimum at a probe power of −20 dBm (1.41×10^{-13} W at the sample). The attenuation for this measurement was −78,5 dB for the whole input path.

Bibliography

[1] LIGO Scientific Collaboration and Virgo Collaboration *et al.* Observation of Gravitational Waves from a Binary Black Hole Merger. *Physical Review Letters* **116**, 061102 (2016).

[2] E. Meyer. Atomic force microscopy. *Progress in Surface Science* **41**, 3 (1992).

[3] R. Gross & A. Marx. *Festkörperphysik* (De Gruyter Oldenbourg, 2012).

[4] M. Aspelmeyer, T. J. Kippenberg & F. Marquardt. Cavity optomechanics. *Reviews of Modern Physics* **86**, 1391–1452 (2014).

[5] C. A. Regal, J. D. Teufel & K. W. Lehnert. Measuring nanomechanical motion with a microwave cavity interferometer. *Nature Physics* **4**, 555 (2008).

[6] J. Moser, J. Güttinger, A. Eichler, M. J. Esplandiu, D. E. Liu, M. I. Dykman & A. Bachtold. Ultrasensitive force detection with a nanotube mechanical resonator. *Nature Nanotechnology* **8**, 493 (2013).

[7] J. Chaste, A. Eichler, J. Moser, G. Ceballos, R. Rurali & A. Bachtold. A nanomechanical mass sensor with yoctogram resolution. *Nature Nanotechnology* **7**, 301 (2012).

[8] Bosch-Sensortec. BMA 455 (2016).

[9] J. D. Teufel, T. Donner, D. Li, J. W. Harlow, M. S. Allman, K. Cicak, A. J. Sirois, J. D. Whittaker, K. W. Lehnert & R. W. Simmonds. Sideband cooling of micromechanical motion to the quantum ground state. *Nature* **475**, 359 (2011).

[10] F. Hocke, X. Zhou, A. Schliesser, T. J. Kippenberg, H. Huebl & R. Gross. Electromechanically induced absorption in a circuit nano-electromechanical system. *New Journal of Physics* **14**, 123037 (2012).

[11] M. Pernpeintner, T. Faust, F. Hocke, J. P. Kotthaus, E. M. Weig, H. Huebl & R. Gross. Circuit electromechanics with a non-metallized nanobeam. *Applied Physics Letters* **105**, 123106 (2014).

[12] K. C. Schwab & M. L. Roukes. Putting mechanics into Quantum mechanics. *Physics Today* **58**, 36–42 (2005).

[13] M. D. LaHaye, J. Suh, P. M. Echternach, K. C. Schwab & M. L. Roukes. Nanomechanical measurements of a superconducting qubit. *Nature* **459**, 960–964 (2009).

[14] M. H. Devoret & R. J. Schoelkopf. Superconducting Circuits for Quantum Information: An Outlook. *Science* **339**, 1169 (2013).

[15] P. W. Shor. Algorithms for quantum computation: discrete logarithms and factoring. In *, 35th Annual Symposium on Foundations of Computer Science, 1994 Proceedings* 124 (1994).

[16] D. Deutsch & R. Jozsa. Rapid Solution of Problems by Quantum Computation. *Proceedings of the Royal Society of London A: Mathematical, Physical and Engineering Sciences* **439**, 553 (1992).

[17] D. Ballester, G. Romero, J. J. GarcÃa-Ripoll, F. Deppe & E. Solano. Quantum Simulation of the Ultrastrong-Coupling Dynamics in Circuit Quantum Electrodynamics. *Physical Review X* **2**, 021007 (2012).

[18] J. Clarke & F. K. Wilhelm. Superconducting quantum bits. *Nature* **453**, 1031 (2008).

[19] J. Koch, T. M. Yu, J. Gambetta, A. A. Houck, D. I. Schuster, J. Majer, A. Blais, M. H. Devoret, S. M. Girvin & R. J. Schoelkopf. Charge-insensitive qubit design derived from the Cooper pair box. *Physical Review A* **76**, 042319 (2007).

[20] A. Wallraff, D. I. Schuster, A. Blais, L. Frunzio, R.-S. Huang, J. Majer, S. Kumar, S. M. Girvin & R. J. Schoelkopf. Strong coupling of a single photon to a superconducting qubit using circuit quantum electrodynamics. *Nature* **431**, 162 (2004).

[21] T. Niemczyk, F. Deppe, H. Huebl, E. P. Menzel, F. Hocke, M. J. Schwarz, J. J. Garcia-Ripoll, D. Zueco, T. HÃ¼mmer, E. Solano, A. Marx & R. Gross. Circuit quantum electrodynamics in the ultrastrong-coupling regime. *Nature Physics* **6**, 772 (2010).

[22] T. Niemczyk, F. Deppe, M. Mariantoni, E. P. Menzel, E. Hoffmann, G. Wild, L. Eggenstein, A. Marx & R. Gross. Fabrication technology of and symmetry breaking in superconducting quantum circuits. *Superconductor Science and Technology* **22**, 034009 (2009).

[23] L. Frunzio, A. Wallraff, D. Schuster, J. Majer & R. Schoelkopf. Fabrication and characterization of superconducting circuit QED devices for quantum computation. *IEEE Transactions on Applied Superconductivity* **15**, 860 (2005).

[24] H. Walther, B. T. H. Varcoe, B.-G. Englert & T. Becker. Cavity quantum electrodynamics. *Reports on Progress in Physics* **69**, 1325 (2006).

[25] R. J. Schoelkopf & S. M. Girvin. Wiring up quantum systems. *Nature* **451**, 664 (2008).

[26] H. Paik, D. I. Schuster, L. S. Bishop, G. Kirchmair, G. Catelani, A. P. Sears, B. R. Johnson, M. J. Reagor, L. Frunzio, L. I. Glazman, S. M. Girvin, M. H. Devoret & R. J. Schoelkopf. Observation of High Coherence in Josephson Junction Qubits Measured in a Three-Dimensional Circuit QED Architecture. *Physical Review Letters* **107**, 240501 (2011).

[27] T. Heikkilä, F. Massel, J. Tuorila, R. Khan & M. Sillanpää. Enhancing Optomechanical Coupling via the Josephson Effect. *Physical Review Letters* **112**, 203603 (2014).

[28] J.-M. Pirkkalainen, S. U. Cho, J. Li, G. S. Paraoanu, P. J. Hakonen & M. A. Sillanpää. Hybrid circuit cavity quantum electrodynamics with a micromechanical resonator. *Nature* **494**, 211 (2013).

[29] T. Ramos, V. Sudhir, K. Stannigel, P. Zoller & T. J. Kippenberg. Nonlinear Quantum Optomechanics via Individual Intrinsic Two-Level Defects. *Physical Review Letters* **110**, 193602 (2013).

[30] A. C. Pflanzer, O. Romero-Isart & J. I. Cirac. Optomechanics assisted by a qubit: From dissipative state preparation to many-partite systems. *Physical Review A* **88**, 033804 (2013).

[31] M. Abdi, M. Pernpeintner, R. Gross, H. Huebl & M. J. Hartmann. Quantum State Engineering with Circuit Electromechanical Three-Body Interactions **114**, 173602 (2015).

[32] T. A. Palomaki, J. W. Harlow, J. D. Teufel, R. W. Simmonds & K. W. Lehnert. Coherent state transfer between itinerant microwave fields and a mechanical oscillator. *Nature* **495**, 210–214 (2013).

[33] F. Hocke. *Microwave Circuit-electrodynamics in a Nanomechanical Hybrid System*. Phd thesis, Walther-Meißner-Institut, TU München (2013).

[34] P. E. Schmidt. *Inductive switchable cavity electromechanics*. Master's thesis, TU München (2015).

[35] F. Wulschner. *Controlled interactions in superconducting quantum circuits*. Phd thesis, Walther-Meißner-Institut, TU München (to be submitted 2016).

[36] W. W. Timoshenko S. & Y. D.H. *Vibration Problems in Engeneering* (John Wiley and Sons: New York, 1990 5th ed.).

[37] X. Zhou. *Superconducting Cavity Nanoelectromechanics.* Phd thesis, EPFL Lausanne (2013).

[38] Aluminium:the essentials [WebElements Periodic Table].

[39] D. M. Photiadis & J. A. Judge. Attachment losses of high Q oscillators. *Applied Physics Letters* **85**, 482 (2004).

[40] I. Wilson-Rae. Intrinsic dissipation in nanomechanical resonators due to phonon tunneling. *Physical Review B* **77**, 245418 (2008).

[41] A. A. Clerk, M. H. Devoret, S. M. Girvin, F. Marquardt & R. J. Schoelkopf. Introduction to quantum noise, measurement, and amplification. *Reviews of Modern Physics* **82**, 1155–1208 (2010).

[42] P. R. Saulson. Thermal noise in mechanical experiments. *Physical Review D* **42**, 2437–2445 (1990).

[43] M. Goeppl, A. Fragner, M. Baur, R. Bianchetti, S. Filipp, J. M. Fink, P. J. Leek, G. Puebla, L. Steffen & A. Wallraff. Coplanar waveguide resonators for circuit quantum electrodynamics. *Journal of Applied Physics* **104**, 113904 (2008).

[44] D. Pozar. *Microwave engeneering* (John Wiley and Sons: New York, 2012 4th ed).

[45] B. A. Mazin. Microwave Kinetic Inductance Detectors (2004).

[46] J. Goetz, F. Deppe, M. Haeberlein, F. Wulschner, C. W. Zollitsch, S. Meier, M. Fischer, P. Eder, E. Xie, K. G. Fedorov, E. P. Menzel, A. Marx & R. Gross. Loss mechanisms in superconducting thin film microwave resonators. *Journal of Applied Physics* **119**, 015304 (2016).

[47] H. Haus. *Waves and fields in optoelectronics* (Prentice-Hall: Englewood Cliffs, New Jersey, 1984).

[48] I. Wilson-Rae, N. Nooshi, W. Zwerger & T. J. Kippenberg. Theory of Ground State Cooling of a Mechanical Oscillator Using Dynamical Backaction. *Physical Review Letters* **99**, 093901 (2007).

[49] A. Schliesser, P. Dela'Haye, N. Nooshi, K. J. Vahala & T. J. Kippenberg. Radiation Pressure Cooling of a Micromechanical Oscillator Using Dynamical Backaction. *Physical Review Letters* **97**, 243905 (2006).

[50] C. K. Law. Interaction between a moving mirror and radiation pressure: A Hamiltonian formulation. *Physical Review A* **51**, 2537 (1995).

[51] C. Genes, D. Vitali, P. Tombesi, S. Gigan & M. Aspelmeyer. Ground-state cooling of a micromechanical oscillator: Comparing cold damping and cavity-assisted cooling schemes. *Physical Review A* **77**, 033804 (2008).

[52] P. Grangier, J. A. Levenson & J.-P. Poizat. Quantum non-demolition measurements in optics. *Nature* **396**, 537 (1998).

[53] M. L. Gorodetsky, A. Schliesser, G. Anetsberger, S. Deleglise & T. J. Kippenberg. Determination of the vacuum optomechanical coupling rate using frequency noise calibration. *Optics Express* **18**, 23236 (2010).

[54] B. D. Josephson. Possible new effects in superconductive tunnelling. *Physics Letters* **1**, 251 (1962).

[55] J. Clarke & A.I.Braginsky. *The SQUID Handbook* (Wiley-VCH Verlag GmbH & Co. KGaA).

[56] P. W. Anderson & J. M. Rowell. Probable Observation of the Josephson Superconducting Tunneling Effect **10**, 230 (1963).

[57] M. J. Schwarz, J. Goetz, Z. Jiang, T. Niemczyk, F. Deppe, A. Marx & R. Gross. Gradiometric flux qubits with a tunable gap. *New Journal of Physics* **15**, 045001 (2013).

[58] M. O. Scully & M. S. Zubairy. *Quantum optics* (Cambridge University Press, 1997).

[59] E. T. Jaynes & F. W. Cummings. Comparison of quantum and semiclassical radiation theories with application to the beam maser. *Proceedings of the IEEE* **51**, 89 (1963).

[60] A. Blais, R.-S. Huang, A. Wallraff, S. M. Girvin & R. J. Schoelkopf. Cavity quantum electrodynamics for superconducting electrical circuits: An architecture for quantum computation. *Physical Review A* **69**, 062320 (2004).

[61] N. B. Delone & V. P. Krainov. AC Stark shift of atomic energy levels. *Physics-Uspekhi* **42**, 669 (1997).

[62] F. Hocke, M. Pernpeintner, X. Zhou, A. Schliesser, T. J. Kippenberg, H. Huebl & R. Gross. Determination of effective mechanical properties of a double-layer beam by means of a nano-electromechanical transducer. *Applied Physics Letters* **105**, 133102 (2014).

[63] Q. P. Unterreithmeier, T. Faust & J. P. Kotthaus. Damping of Nanomechanical Resonators. *Physical Review Letters* **105**, 027205 (2010).

[64] C. Deng, M. Otto & A. Lupascu. An analysis method for transmission measurements of superconducting resonators with applications to quantum-regime dielectric-loss measurements. *Journal of Applied Physics* **114**, 054504 (2013).

[65] S. Gröblacher, K. Hammerer, M. R. Vanner & M. Aspelmeyer. Observation of strong coupling between a micromechanical resonator and an optical cavity field. *Nature* **460**, 724 (2009).

[66] M. Mueting. *Time domain characterization of a transmon qubit*. Master's thesis, TU München (2015).

[67] D. I. Schuster, A. A. Houck, J. A. Schreier, A. Wallraff, J. M. Gambetta, A. Blais, L. Frunzio, J. Majer, B. Johnson, M. H. Devoret, S. M. Girvin & R. J. Schoelkopf. Resolving photon number states in a superconducting circuit. *Nature* **445**, 515 (2007).

[68] A. A. Houck, D. I. Schuster, J. M. Gambetta, J. A. Schreier, B. R. Johnson, J. M. Chow, L. Frunzio, J. Majer, M. H. Devoret, S. M. Girvin & R. J. Schoelkopf. Generating single microwave photons in a circuit. *Nature* **449**, 328 (2007).

[69] F. Deppe, M. Mariantoni, E. P. Menzel, A. Marx, S. Saito, K. Kakuyanagi, H. Tanaka, T. Meno, K. Semba, H. Takayanagi, E. Solano & R. Gross. Two-photon probe of the Jaynes-Cummings model and controlled symmetry breaking in circuit QED. *Nature Physics* **4**, 686 (2008).

Acknowledgments

At the end of this thesis I would like to express my gratitude to everyone who contributed to the success of this work. In particular, I thank:

Prof. Dr. Rudolf Gross, for giving me the opportunity to perform my master's thesis at the Walther-Meißner-Institut.

Dr. Hans Hübl, for supervising this thesis with a watchful eye but nevertheless leaving me with enough latitude to pursue my own ideas.

Matthias Pernpeintner, for advising me during this thesis and introducing me to all the know-how I needed, and more. For his patience and immediate help with all problems or questions I could think of.

Philip Schmidt, for advising me during the time Matthias was in faraway lands and helping me with lots of measurement problems as well as discussing the results afterwards.

Friedrich Wulschner for introducing me to the fabrication and measurements of Josephson junctions and transmon qubits.

The staff of the WMI, for keeping everything running and making my work so much easier.

My office colleagues Stefan Pogorzalek, Ahmed Alshemi, Patrick Yard, Anh Tuan Le, Tobias Wimmer, Hiroto Sakimura and Prof. Dr. B.S. Chandrasekhar. For a good working atmosphere and a lot of fruitful discussions about physics, the universe and everything.

All the other master and PhD students and postdocs for enlightening discussions on hot topics at the WMI and elsewhere.

And last, but not least my parents, my brother and the rest of my family for the constant support during my study in whatever fashion imaginable.